Investigation Of Metal Insulator Transition In 3D Transition Metal Oxides

Thesis submitted for the degree of

Doctor of Philosophy (Science)

in

Physics (Experimental)

by

RAVINDRA SINGH BISHT

Department of Physics

University of Calcutta

2019

Dedicated To

My Brother……

ACKNOWLEDGMENTS

I would like to recognize the importance of following individuals who are the integrated part of this dissertation. I wish to express my sincere thanks to my Ph.D. supervisor, Prof. A. K. Raychaudhuri, who always supported and helped me over these years. I have learnt a lot from him and I am really thankful to his constant inputs and insights throughout this dissertation. I further thank him for giving me the freedom to carry out my research work. The discussion I had with him always motivated me to think more clearly.

I also thanks to Dr. Barnali Ghosh (Saha) for her support and help whenever it was necessary. I further thanks to her for the suggestions on synthesis of nickelates. I express my deepest gratitude and thanks to Prof. Aveek Bid and his research group at IISc Bangalore for allowing me to work in their lab without hesitation for nearly 60 days. The work carried out in his lab has an important contribution to this dissertation. I thank Prof. Tanusri Saha Dasgupta as an examiner for her inputs during my academic talks. My thanks are also due to Dr. V. Reddy, Dr. Achintya Singha, Dr. D. Kabiraj, Dr. R. J. Chaudhury, Dr. S. R. Barman, and Prof. Mandar M. Deshmukh for allowing me to work in there lab for completing some of the measurements/characterizations. I am grateful to my college teachers Prof. S. Annapoorni, Prof. Patrick Dasgupta, Late. Dr. R. Venkatraman, and Dr. Sangeeta Gadre, who motivated me to take this journey.

I thank Sudipta, Anirban, Shaili, Dr. Gopinath Daptary, Dr. Rishi Ghimire, Dr. Sudeshna Samanta, Dr. Ankita Ghatak, and Dr. Rajib Nath to have a collaboration on different projects. I appreciate the present and past members of NEW NANO LAB for their extensive support throughout this journey. I always cherish the academic as well as non-academic discussion with them.

I am thankful to my friends Poonam, Poulami, Ransell, Shaili, Dhani, Kumar Neeraj, Ankan, Ritam, Shishir da, Siddhi di, Vibhuti, Ruchi, Neha, Tukun, Avinash, Darshan, and Raghvendra for making these years memorable. Thank you guys for making “city of joy” a joyful place for me too. A special thanks goes to Dr. Ashutosh Kumar Singh, Dr. Tanmoy Ghosh, Dr. Sandeep Aggarwal, Dr. Arup Ghosh and Dr. Sagar Sarkar for their help whenever it needed.

My heartfelt thanks goes to Vaibhav, Sanjeev, Harsh, Ankur, Geetika, Monika, Sonal, Shweta, Pratibha and Randhir.

My thanks are also due to the staff of the technical cell and workshop for providing technical assistance. Their valuable support played an immense role in completing this dissertation.

I am very fortunate to have a family who supported unconditionally throughout this journey. I will always remain grateful and in debt to my parents for always being there for me. Being youngest at home, I always got advice from my brother, sister, and brother-in-law which helped me to keep myself calm while staying away from home. Finally, I would like to express my love to my niece, Samaya.

Ravindra Singh Bisht

PUBLICATIONS

1. Ravindra Singh Bisht, Gopi Nath Daptary, Aveek Bid and A. K. Raychaudhuri, "Continuous transition from weakly localized regime to strong localization regime in $Nd_{0.7}La_{0.3}NiO_3$ films" *J. Phys.: Condens. Matter*, 2019, 31, 145603
2. Ravindra Singh Bisht, S. Samanta, and A. K. Raychaudhuri, "Phase coexistence near the metal-insulator transition in a compressively strained $NdNiO_3$ film grown on LaAlO3: Scanning tunneling, noise, and impedance spectroscopy studies" *Phys. Rev. B 95, 115147 (2017)*
3. Ravindra Singh Bisht, R. R. Ghimire, and A. K. Raychaudhuri, "Control of Grain-Boundary Depletion Layer and Capacitance in ZnO Thin Film by a Gate with Electric Double Layer Dielectric*" J. Phys. Chem. C 119, 27813−27820 (2015)*
4. Shaili Sett, Ravindra Singh Bisht, Ankita Ghatak, and A. K. Raychaudhuri, "Surface oxide driven super-linear photo response in a Germanium nanowire" *Appl. Surf. Sci. 497 143754 (2019)*
5. Ravindra Singh Bisht *etal.* "Electroresistance in Nickelates" (*To be Submitted*)
6. Ravindra Singh Bisht *etal.* "Disorder driven suppression of a correlation driven Mott transition" (*To be Submitted*)
7. Ravindra Singh Bisht *etal.* "Effect of swift heavy ion induced disorder in $Nd_{0.7}La_{0.3}NiO_3$ film" (*To be Submitted*)

SCIENTIFIC EVENTS ATTENDED

1. National Conference on Quantum Condensed Matter, IISER Mohali, India (2018) (Poster Presentation).
2. APS March Meeting, Los Angeles 2018 (Oral Presentation).
3. NANOINDIA 2017, IIT Delhi, India (Poster Presentation).
4. Indo-US Bilateral Workshop on Physics and Chemistry of Oxides: Theory meets Experiments, Vedic Village, Kolkata, India (2016) (Poster and Oral Presentation).
5. International Conference on Nanoscience and Technology 2016, IISER Pune, India (Poster Presentation).
6. ATNMC workshop, S. N. Bose National Centre for Basic Sciences, Kolkata, India (2015).
7. Nanodays, S. N. Bose National Centre for Basic Sciences, Kolkata, India (2015) (Poster Presentation).
8. INUP Familiarization workshop 2014, Indian Institute of Science, 21-23 May, (2014).
9. Bringing the Nanoworld together, Saha Institute of Nuclear Physics, Kolkata, India (2014).

Table of Contents

Chapter 1 Introduction

In this chapter, we introduce the fundamentals of metal-insulator transition and oxide perovskite in the context of rare earth nickelates. A brief review of the underlying physics of structural, electronic, and magnetic phase transition has been given. We discuss certain scenarios that make nickelates system interesting for the scientific community from a basic physics point of view. This has been followed by the motivation and overview of the thesis.

1.1 Motivation

The metal-insulator transition (MIT) is one of the oldest problems in condensed matter physics but still one of the least understood, because of its multi-dimensionality and due to the absence of a coherent theory/theories that can explain most of the observations. A number of systems like oxides, chalcogenides, and doped semiconductors show MIT [1-10]. Change in externally controllable physical parameters like doping, temperature, pressure, strain and magnetic field can also lead to MIT in a given material [11-20]. In general, when we talk about MIT, it is classified into two broad classes namely correlation driven Mott transition and a disorder driven Anderson transition [7-10]. In a correlation driven MIT, the main factor that controls the transition is the density of states (DOS) at the Fermi level (E_F). In this transition, a correlation gap in DOS at E_F opens up and such transitions are driven by temperature/pressure. These temperature driven transitions are often first order in nature. Another distinct class of MIT occurs in a disorder solid, which is known as Anderson transition. In Anderson transition disorder leads to localized states although the DOS at the E_F remains finite. The mobility edge separates the extended and localized states in an Anderson transition. Anderson transition is often tuned by varying disorder or adjusting the E_F by carrier doping through substitutional doping of one or more constituents. These types of MIT are continuous (also called second order phase transition) in nature [9, 12, 21].

Transition metal oxides (TMO) form a broad class of solids where MIT has been studied extensively because of the strong correlations amongst the crystal structure, charge and spin degrees of freedom [2-12]. TMO compounds in that context present a rich physics and even the ideas like "strong correlations" were developed for the first time from such class of materials. The diverse and fascinating properties of the TMO like MIT, ferroelectricity, colossal magnetoresistance, spin-orbit coupling, and high-temperature superconductivity makes it a versatile system to study basic physics from decades and the interest is still alive [7,8,10]. Most of the physical properties in TMO's can be understood by an itinerant or a localized picture of the electrons. This dual behavior of electrons (localized or delocalized) in TMO's can even lead to a jump in conductivity by many orders [3].

A plethora of TMO compounds which show MIT, ferroelectricity, colossal magnetoresistance, and high temperature superconductivity belong to a class known as oxide perovskite (ABO_3),

where “A” site cations represent rare-earth ion, “B” site cations represent transition metal ion and “O” anions represent oxygen. Most of the underlying physics in such compounds is driven by the transition metal ion and by changing the transition metal ion, one can tune the interplay between lattice, charge and spin degrees of freedom. Distinct classes of compounds like vanadates, titanates, manganites, cobaltates, nickelates, and cuparates show such interplay between lattice, charge and spin degrees of freedom [7, 10]. The oxide perovskites thus cover a spectrum of physical properties and have been investigated for a long time. The highly susceptible nature of perovskite oxides to undergo a structural distortion from the ideal cubic structure makes it an important candidate to understand its exotic physical phenomenon [22]. Another important parameter is the valence state of the transition metal ions as they are known to exhibit multiple valences which essentially change the nature of bonding from being ionic to covalent [10, 23].

As it is emerging in last decade or so that the MIT in these materials has aspects of both Mott transition and Anderson transition, so that one has mixed first-order and second-order transitions with co-existence of different electronic phases [24-28]. In this thesis, we have chosen the rare earth nickelates ($RNiO_3$) which belongs to 3d TMO, to understand MIT in such class of materials. We have studied some of the emerging aspects of these phase co-existence which are probed using different physical techniques. We have shown that such phase co-existence indeed occurs and may lead to electroresistance effect. We have also investigated the nature of the temperature driven transition that has been tuned with isovalent substitutional doping and disorder induced by swift heavy ions of inert gases. We have further investigated whether co-existence leads to the development of correlated fluctuations. A description of these results has been given in the later section of this chapter.

1.2 Introduction to perovskites

The first perovskite structure, calcium titanate ($CaTiO_3$) was discovered in 1839, in the Ural Mountains. The structural analysis shows the titanium ions are surrounded by six oxygen anions and forms octahedra [29, 30]. The calcium ion occupies the space between the octahedra and forms a crystal structure. In general, there are many compounds which follow a similar structure and are termed as perovskite with general formula ABX_3. When A-site cations are replaced by rare earth

ion, B site cations are replaced by transition metal ion and X anions are replaced by oxygen, the structure is known as TMO perovskite and also known as oxide perovskite [4, 31, 32]. In most of the oxide perovskite (hereafter we will use the word oxides for "oxide perovskites"), the structural distortion is primarily decided by A cations while the valence state of B cations play an important role in deciding the underlying physics i.e. electronic, magnetic and structural properties.

In the crystal structure of ABO_3 compounds, the rare earth cations A sits at the body center and B sits at the corner of the unit cell and is surrounded by six oxygen anion which forms octahedra. Together this arrangement in a periodic manner leads to a crystal structure. The schematic of an ideal cubic structure is shown in Figure 1(a). The A-site cations are twelve fold coordinated with oxygen anions and B site cations are six fold coordinated with oxygen anions. The BO_6 octahedra are a functional and fundamental unit for the ABO_3 structure. Looking into the crystal structure of an ideal cubic structure like strontium titanate ($SrTiO_3$), the Ti-O-Ti bond angle is almost 180^0. However, in most of the cases, this doesn't hold good and the structure suffers from distortion due to a large mismatch in the ionic radius of A and B site cations which leads to a change in the B-O-B (also called superexchange angle) bond angle. In total there exist six B-O-B bond angles in an octahedron, the weighted average of two B-O_{apical}-B and four B-O_{basal}-B bond angles are often used to quantify the distortion of the crystal structure from the ideal cubic structure [5]. Figure 1(b) shows a distorted cubic structure (orthorhombic) and the deviation in superexchange angle from 180^0 is shown in Figure 1(f).

Ideally, the lattice constant (a) and ionic radii of A-site cations (r_a), B site cations (r_b) and oxygen anions (r_o) for a cubic structure should satisfy the criteria: $a = 2(r_o + r_b) = \sqrt{2}\,(r_o + r_a)$. Any deviation from this equality can be estimated by Goldschmidt tolerance factor defined as $t = \frac{(r_o + r_a)}{\sqrt{2}\,(r_o + r_B)}$. Most of the compounds are cubic in the range $0.9 < t < 1$ and may relax to a rhombohedral symmetry. For, $0.9 \leq t$, the structure, in general, adopts an orthorhombic or rhombohedral symmetry. Figure 1.1 (b) represents the lattice parameters and corresponding angles for cubic, rhombohedral, orthorhombic and monoclinic unit cells. (Note: The calculation of tolerance factor assumes the ionic nature of the chemical bond, in actual practice, this may not be always true. As a result of different nature of bonding this can only give a rough estimation (especially $RNiO_3$ is interpreted as a mixed bonding character)) of the distortion. In Figure 1.1 (a)

and (b) we show a cubic structure and the lattice parameters of its distorted counterpart respectively.

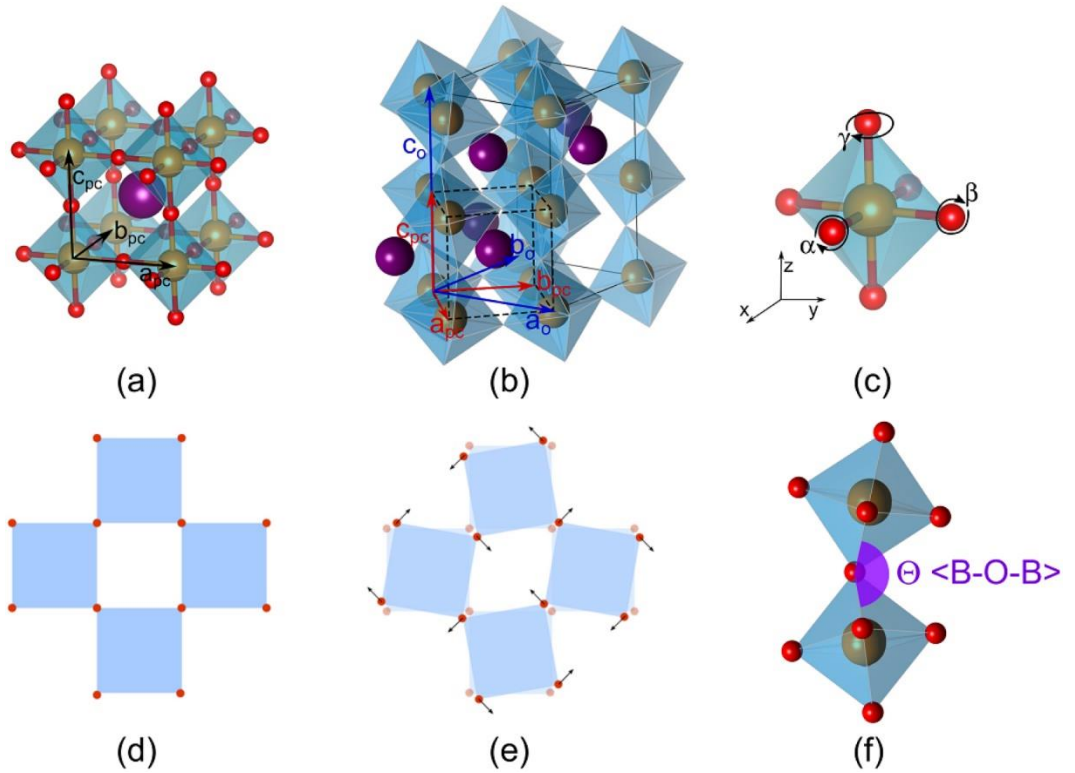

Figure 1 (a) and (b) Ideal cubic structure and distorted orthorhombic structure of ABO_3 compound respectively, (c) Representation of BO_6 octahedra with crystallographic axes according to Glazer notation, (d) top view of BO_6 octahedra of an ideal cubic structure and (e) top view of BO_6 octahedra in distorted orthorhombic structure in Glazer notation. (f) Deviation of B-O-B bond angle (superexchange angle) from 180^0 [Image is taken from reference 5 with author permission].

In crystallographic notation, all the structural distortions are accompanied by either rotation of octahedra or tilting of octahedra. In Figure 1 (a) and (b) we show the structure of an ideal cubic structure and distorted orthorhombic structure of ABO_3 compound. The first notation to represent such rotation or tilt of octahedra was given by Glazer and known as Glazer notation [33, 34]. In Glazer notation, a, b, and c represent the crystallographic direction while the superscript represents the direction of the rotation for octahedra. The Glazer notation $a^0a^0a^0$ for an ideal cubic structure represents that there is no rotation of octahedra in all the directions. Further, an orthorhombic structure (Pbnm space group) has a Glazer notation $a^-a^-c^+$ which represents an out of phase rotation of equal magnitude along the x and y-axis while an in-phase rotation of the octahedra along the z-

axis [29, 33]. Figure 1(d) and (e) show the top view of BO_6 octahedra in Glazer notation for an ideal cubic structure and distorted orthorhombic structure respectively.

For $t \geq 1$, the structure undergoes a polar distortion and may lead to a ferroelectric structural distortion; further increasing the t leads to a hexagonal polymorph. In actual cases, the structure can be distorted due to several factors like strain, pressure, temperature, ionic radii mismatch of A and B site cations, ionic radii mismatch of A-site cations for two or more cations (cationic disorder) and Jahn-Teller (JT) distortion [38-50].

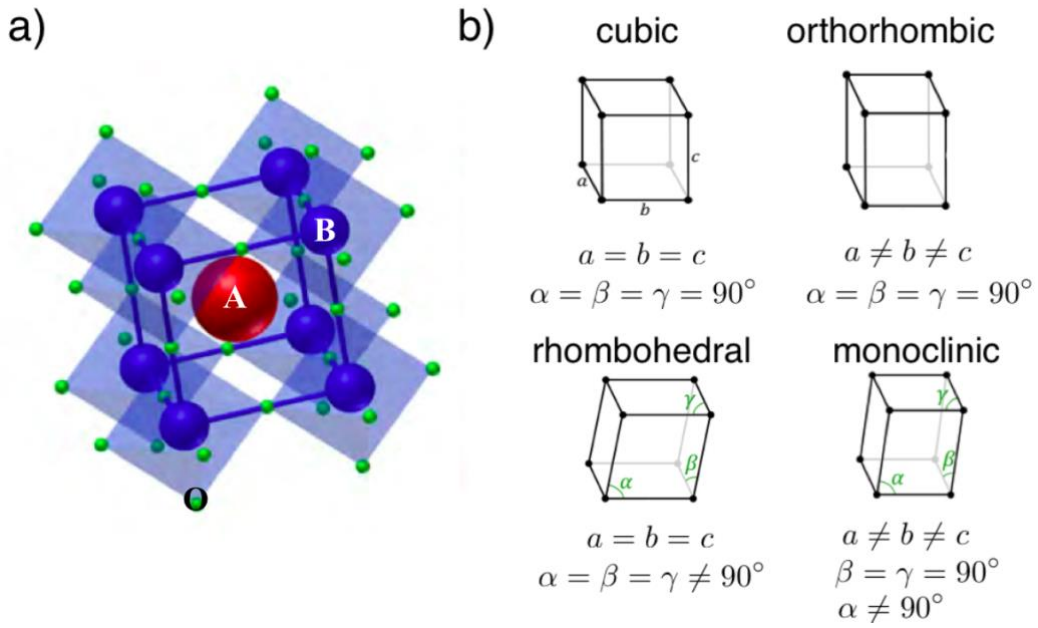

Figure 1.1 (a) Ideal cubic structure of ABO_3 compounds and (b) Representation of cubic, orthorhombic, rhombohedral, and monoclinic unit cells along with the lattice parameters [Image is taken from reference [13]].

As discussed above the cationic radius $< r_a >$ plays an important role in the physical properties of the oxides. When two or more cations sit at the same site, due to a mismatch in the ionic radius of this random substitution a disorder is induced in the crystal and is known as a cationic disorder. If two cations sit at the A site, the cationic disorder, in this case, can be quantified by the radius distribution of A-site cations variance (σ^2). The relation is given below as:

$$\sigma^2 = \sum_i (x_i r_{ai}^2) - < r_a >^2 \qquad (1)$$

where $< r_a >= \sum_i (x_i r_{ai})$ is the average radii of the i^{th} ion with a fractional doping x_i and r_{ai} represent the ionic radii of random ion sits at the A site. For $Nd_{1-x}La_xNiO_3$ the average radii can be expressed as:

$$< r_a >= (1 - x) r_{Nd}^{3+} + x r_{La}^{3+} \qquad (1.1)$$

The term "chemical pressure" has been widely used in the literature when 'A' site cations have the same valence but different ionic radii. In that case, by isovalent substitution one can really change the chemical pressure in the crystal structure. In the later section, we will discuss how these properties affect the electronic structure of a material.

1.3 Metal Insulator Transition

The ideal definition of metal and insulator is $\sigma \neq 0$ and $\sigma = 0$ respectively as T→ 0 K, where σ represents electrical conductivity. If we look into the Einstein relation ($\sigma = e^2 N(E_F) D$, where e is an electronic charge, $N(E_F)$ is DOS at E_F and D is the diffusion coefficient) for diffusive transport. We can get an insulator in two ways either with having D = 0 or $N(E_F)$ = 0 [7, 10]. In the subsections below, we will discuss how one can get a transition from metal to insulator and vice-versa. In particular, we will discuss Mott and Anderson transition in this context as other MIT's are out of the scope of this thesis.

1.3.1 Mott Transition

The band theory was considered to be the most successful quantum theory for solids that explained most of the electronic transport in the metals, semiconductors, and insulators. However, it failed for compounds like nickel oxide (NiO). According to the band theory due to the presence of a half-filled band, cubic NiO should exhibit a metallic character. However, cubic NiO has been reported as an insulator along with other TMO like cobalt oxide (CoO) (in 1937) by Verwey. The first insight to explain the insulating nature in such compounds was given by Peierls. Later, Mott explained how electron-electron interaction in some compounds can lead to an insulating state [7-10, 51].

In the model, Mott suggested that when a single electron is sitting at a lattice site, in the absence of electron-electron interaction they will form a half-filled band and when two electrons with

opposite spins sit at the same site the band will be full. However in presence of electron-electron interaction (U), for a filled band where two electrons with opposite spins are sitting at the same site, the energy cost (U) to keep two electrons at the same site can split the band into a lower band of single occupied sites and an upper band with double occupied sites. The system would be a "Mott insulator" when a lower band with the single occupied site is filled while the upper band with double occupancy is empty. In Figure 1.2 (I) and (II) we show the schematic of Mott idea to understand the splitting of bands. As shown for a non-interacting picture, (Figure 1.2 (I)) all the lattice sites carry one electron each and electrons hopping can take place from one site to another with a transition probability t. In the presence of interaction, the energy gained by hopping can be compensated by U which leads to splitting of the band (Figure 1.2 (III)). The system would be insulating if there is a gap associated with it. The first theoretical model was introduced by Hubbard in this context after implementing Mott's idea to explain the insulating state. According to the Hubbard model, the Hamiltonian for such systems can be written as:

$$H = -t \sum_{<i,j>\sigma} c_{i,\sigma}^{\dagger} c_{j,\sigma} + U \sum_i n_{i\uparrow} n_{i\downarrow} \qquad (1.2)$$

where t is hopping integral and represents kinetic energy term, U is the onsite Coulomb potential due to electron-electron interaction and n is number operator. The split energy bands were represented as Lower Hubbard Band (LHB) and Upper Hubbard Band (UHB).

The competition between U, B (bandwidth of d band before splitting), and t decides the nature of the electronic state of the specimens. For one dimension, the hopping integral t will result in a single band of bandwidth, B = 2zt, where z is coordination number and t is hopping probability. For U/B << 1 the kinetic energy term dominates and the system is metallic, for U/B >> 1 the onsite coulomb energy dominates and drives the system to an insulating state. Thus tuning the U/B ratio can drive a system from metallic to insulating regime, such transitions are referred as "Mott-Hubbard" transition and the tuning of U/B can be done in a number of ways like strain, isovalent substitution, pressure, and carrier doping, etc. Further, it has been observed that the bandgap also depends on the type of ligand attached to the transition metal ion like Ni, Co, and Cu [23].

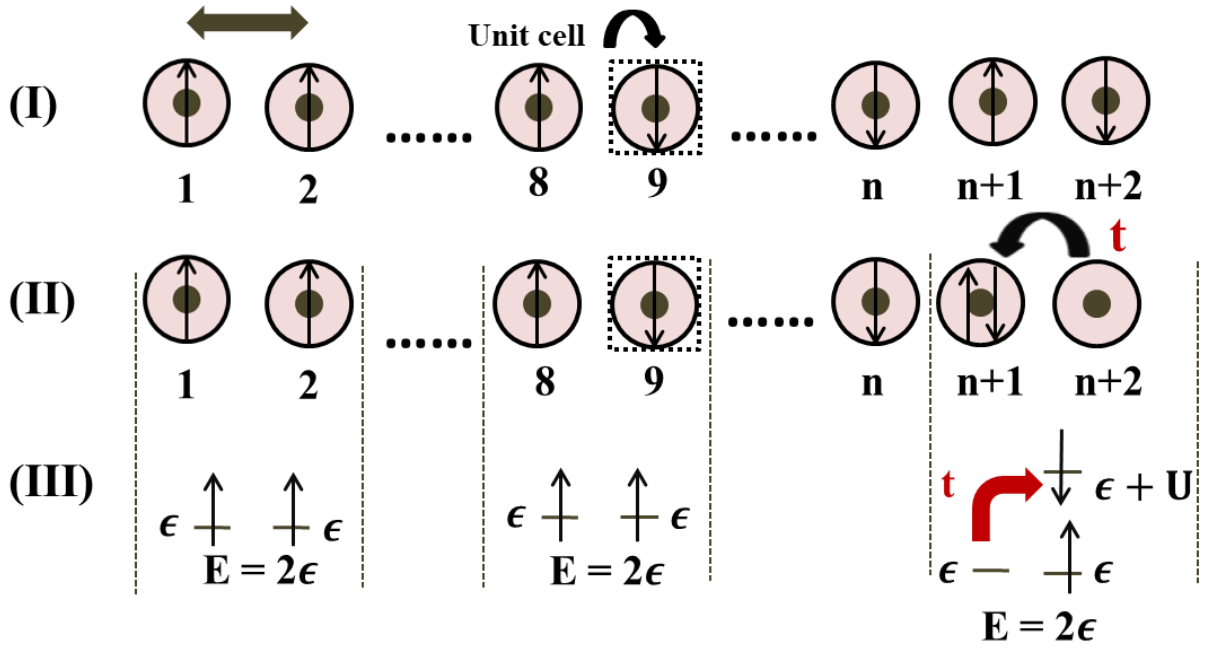

Figure 1.2 The model for non-interacting and interacting picture of electrons per lattice site (I) The arrangement of electrons per lattice site; no spin ordering has considered here (II) Electron hopping from one lattice site to another with transition probability t and (III) Splitting of bands due to onsite coulomb repulsion U leads to a splitting of band [Image adapted from reference 23 and modified].

In such cases, along with the onsite coulomb repulsion, the hybridization between transition metal ion and ligand plays an important role to understand the electronic properties. This idea was adopted by Zaanen, Sawatzky, and Allen (ZSA), they suggested for a strong hybridization between a transition metal ion d orbital and ligand p orbital, the hopping term $t_{pd,}$ and charge transfer energy Δ decide the bandwidth of transition metal ion [53]. In Figure 1.3 (a) we show that when $\Delta > U$ it follows the Mott Hubbard picture and in that case p-band lies below the LHB while in the limit $\Delta < U$ the gap opens up between UHB and ligand p-band since the LHB lies below ligand p-band; such insulators are named as charge transfer insulator as shown in Figure 1.3 (b). The cuprates and nickelates belong to such class of materials under this scheme [53].

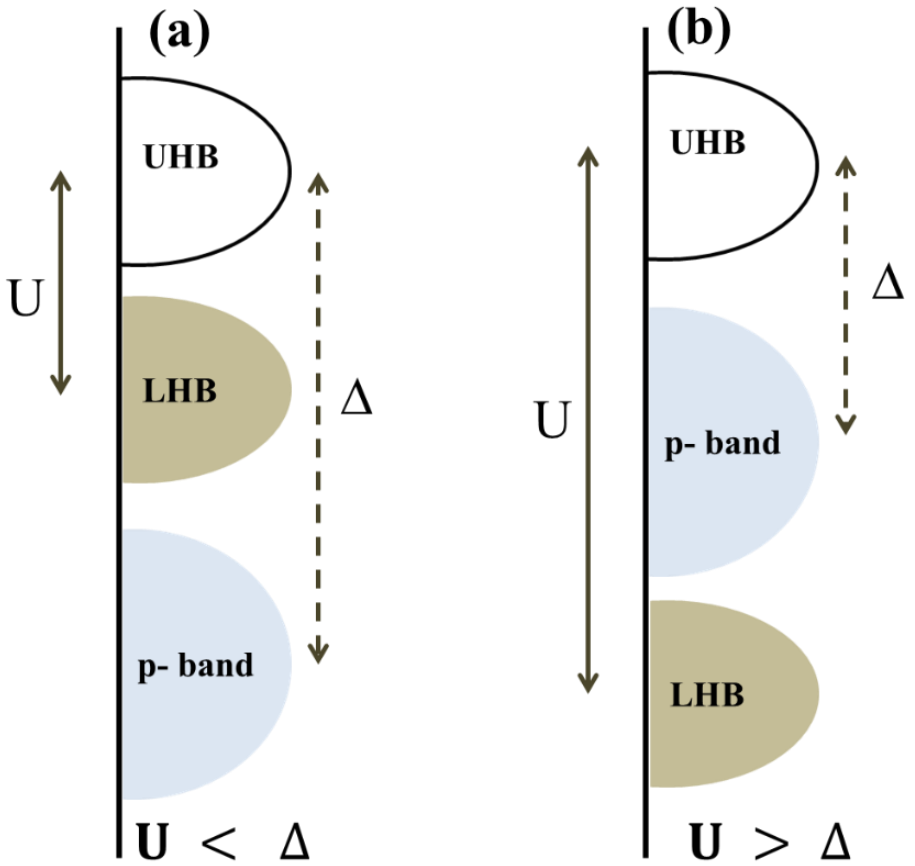

Figure 1.3 (a) Band diagram for Mott-Hubbard insulator and (b) Charge transfer insulator. U and Δ represent onsite coulomb repulsion and charge transfer energy ($\epsilon_d - \epsilon_p$) respectively.

Apart from the insulating state, such transition also leads to the emergence of highly correlated metallic phases which leads to a huge enhancement in the effective mass [13]. The description of such metallic phases has been given under Fermi liquid theory and a T^2 dependence of the resistivity occurs [47]. In Fermi liquid description the excitations of such interacting systems are known as quasiparticles and their lifetime is given as:

$$\frac{1}{\tau_{ee}} \approx \frac{\pi}{h} V^2 N_f^2 E^2 \qquad (1.3)$$

, where h is Planck's constant, V is interaction potential, N_f is DOS at Fermi surface and E is quasiparticles energy. Thus the T^2 dependence of resistivity is always considered as a signature for Fermi liquids, however, this may not be always correct [47].

1.3.2 Anderson Transition

There exist another class of insulators where the disorder can disrupt the local periodicity of the crystal. Such disorder/imperfection in the crystal may come from vacancies, defects, and impurities, etc. which can lead to strong scattering of electrons and hence give rise to an insulating state. One should always remember that the idea of Mott and band insulator assumes a perfect crystal and a long-range periodicity of the crystal. It was pointed out by P. W. Anderson in 1958 that in presence of strong disorder (random potential (V_0)) the diffusion can vanish for a wave propagating in a random potential, the wave function changes dramatically and becomes localized. On the other hand for a weak disorder even if there is a scattering of Bloch waves from the disorder solid, the wave function remains extended even after losing phase coherence [12, 13].

In Figure 1.4 (a) and (b), we show that for a weak disorder the wavefunction remains extended while the wave function decays exponentially for the strong disorder. The decay of the envelope of the wavefunction at r_0 in space can be written as $(\Psi(x_0)) \sim \exp|r - r_0|/\xi$, where ξ is localization length. The electrons in such localized states can't move and are bound to the vicinity of their positions. It is important to note that the Anderson transition has the only scale of conductivity, there is no band gap present in an Anderson insulator. However, in the presence of electron-electron correlation, one can have a correlation gap as seen in many oxides [53].

As shown in Figure 1.4 (c), DOS itself shows no gap and the energy spectrum is continuous. If the E_F lies in the white region the system is metallic but there are the shaded region where the mobility is zero, if E_F lies in such regions the system would show insulating behavior. The boundary of the white and shaded region is called mobility edge and system can undergo an MIT if E_F crosses the mobility edge from either side [10], such transitions are called "Mott-Anderson" transition.

Nevertheless, real materials exhibit much more complex behavior, in that context, it is difficult to explain the nature of the insulating state when both correlation and disorder are present. In table 1, we show the key difference between Mott and Anderson transition.

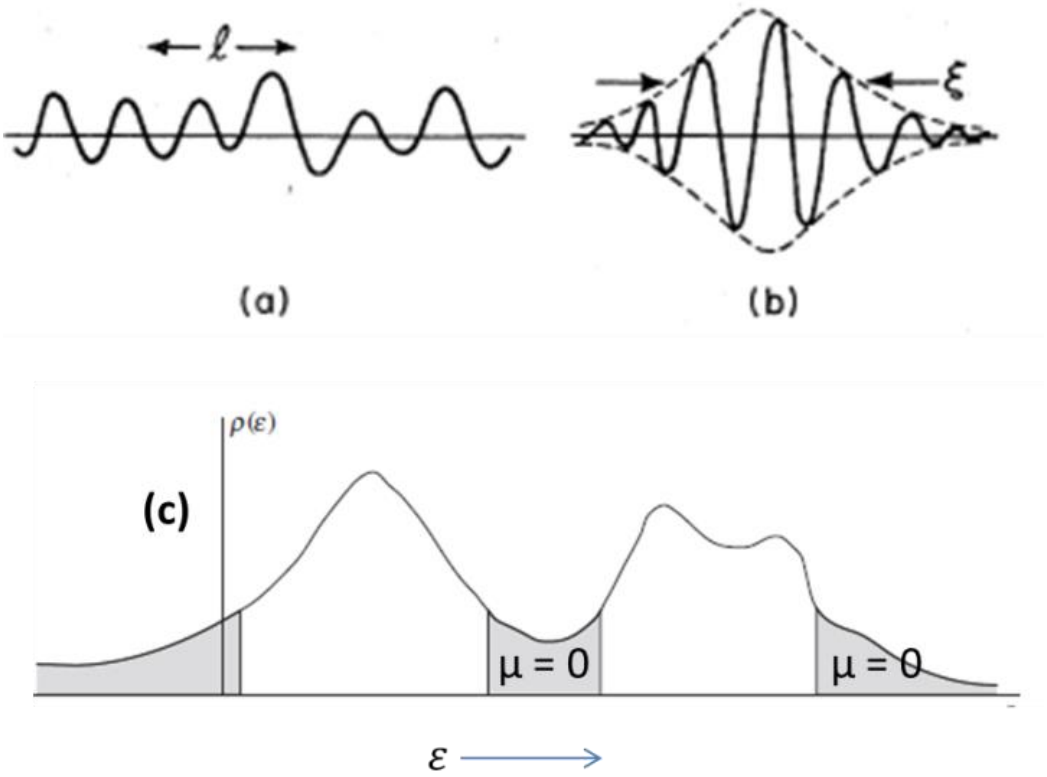

Figure 1.4 (a) The extended state wave function with mean free path length l, (b) The localized state wavefunction decays exponentially over a length scale ξ known as localization length and (c) DOS in a continuous energy spectrum where white region shows the delocalized state and shaded region shows a localized state with zero mobility (μ). The boundary between them is known as the mobility edge [Images (a) and (b) are taken from reference [12] with journal permission and (c) taken from reference [10]].

For the strongly localized regime where the thermal activation is absent, the transport at low temperature is governed by the hopping of electrons from one localized state to other localized states and is known as variable range hopping (VRH). The conductivity then follows a power-law behavior:

$$\sigma = \sigma_0 \exp\left(-\left(\frac{T_0}{T}\right)^n\right) \qquad (1.4)$$

where n depends on the dimension of the system and T_0 is characteristic temperature [54]. In presence of disorder as well as correlation, n is ½.

Table 1 Key difference between a Mott and Anderson transition

Mott Transition	Anderson Transition
✓ Correlation (U) plays an important role. ✓ Many-electron problem. ✓ First-order phase transition when tuned by parameters like pressure or temperature. ✓ May lead to a change in symmetry.	✓ Disorder (V_0) plays an important role. ✓ Single-electron problem. ✓ Continuous transition (Second-order). ✓ No change in the symmetry occurs truly at T= 0 K and cannot be tuned by changing T. The only scale is the scale of conductivity.

After a brief overview and some basic knowledge about crystal structure, and electronic properties in the context of MIT, the following section is devoted to the discussion of experimental observations and theoretical predictions in the context of $RNiO_3$; which is the key material that has been investigated in the thesis.

1.4 Rare Earth Nickelates ($RNiO_3$)

The material was first synthesized in 1971 and was almost forgotten for 20 years [35]. Later, the discovery of high-temperature superconductivity motivated the scientific community to revisit the electronic, structural, and magnetic properties of $RNiO_3$. Earlier results on the bulk $RNiO_3$ by Torrance and co-workers showed an absence of superconductivity, however, some fascinating properties like temperature dependent MIT were observed. Further, the observed MIT can be tuned by the size of rare-earth ion and pressure [35-40]. It has been shown that all the nickelates except $LaNiO_3$ show a temperature-dependent MIT. It was also found that MIT in $RNiO_3$ has a structural basis with a magnetic transition.

1.4.1 Structural, Electronic and Magnetic Properties of Bulk $RNiO_3$

Most of the work in the late 90's was carried out in the bulk samples. As the idea of thin films was not developed that much in the context of complex oxide, which requires high oxygen pressure to

stabilize the valence state of transition metal ion in $RNiO_3$. The difficulty in the synthesis of $RNiO_3$ single crystals arises due to poor stability of Ni^{3+} at ambient pressure and high temperature [55-57]. Later on, some chemical routes have been adopted to synthesize polycrystalline $RNiO_3$ bulk samples at ambient oxygen pressure and low temperature. The electronic properties and transport measurements show that the metal-insulator transition temperature (T_{MI}) can be tuned by changing rare earth size as well as pressure. Further, it was observed that along with MIT, $RNiO_3$ undergo a structural transition also.

The observed structural properties of the $RNiO_3$ with smaller rare-earth ions like Ho, Y, and Er shows a transition from high temperature orthorhombic to low-temperature monoclinic phase while the structural transition was absent in the earlier X-ray diffraction (XRD) and neutron diffraction study for rare earth ions of large sizes like $NdNiO_3$, $PrNiO_3$, and other compounds. The observation of low temperature monoclinic phase from Raman study leads to the argument that the monoclinic phase is too small to be picked up by XRD for large size rare earth ions [58]. Using synchrotron XRD, Garcia and co-workers later showed a transition from high temperature orthorhombic phase to low temperature monoclinic phase for $NdNiO_3$ also [59].

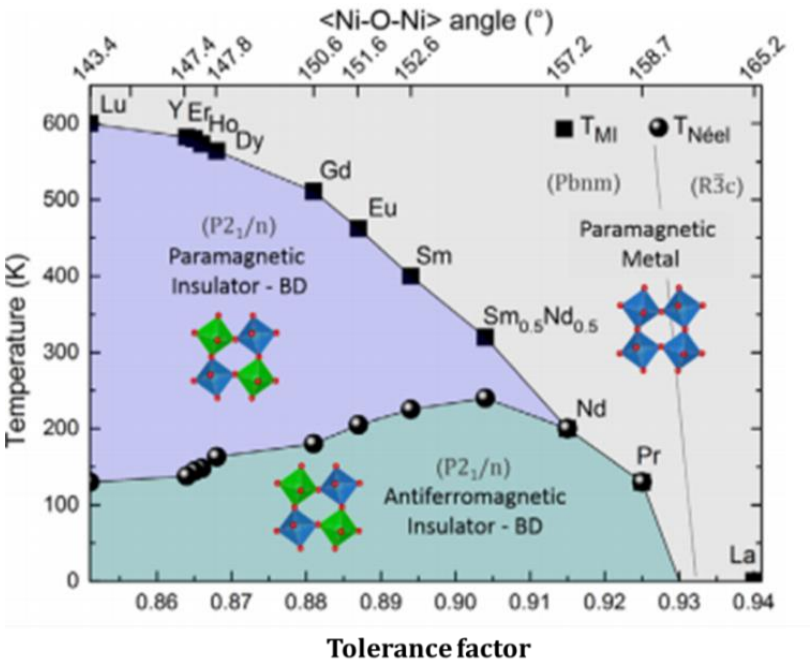

Figure 1.5 The phase diagram of the rare earth nickelates ($RNiO_3$) [Image is taken from reference 5 with author's permission].

All the $RNiO_3$ members except $LaNiO_3$ exhibit a transition from high temperature orthorhombic (Pbnm) structure to a low temperature monoclinic ($P_{21/n}$) structure. The metallic $LaNiO_3$ is rhombohedral (R3C) throughout the entire temperature range as shown in the phase diagram of $RNiO_3$. The phase diagram also suggests that T_{MI} can be tuned continuously from 600 K ($LuNiO_3$) to 120 K ($PrNiO_3$) by mixing two rare earth ions according to Vegard's rule [60]. In Figure 1.5 we show the phase diagram of $RNiO_3$.

As mentioned in the previous paragraph along with the structural change, the $RNiO_3$ undergo a magnetic phase transition from high temperature paramagnetic (PM) phase to low temperature antiferromagnetic (AFM) phase as shown in Figure 1.5. The phase diagram of the material with ions of different ionic radii at the R site also has an impact on the spin order. For instance, when the ionic radius is relatively larger like ionic radii of Pr and Nd, it shows AFM ordering (↑↑↓↓) of nickel moments along with the MIT. For R ions with lower ionic radii, the AFM transition gets de-coupled from the MIT and the Neel Temperature $T_N < T_{MI}$ (Figure 1.5 and 1.6). This suggested that the insulating state in $RNiO_3$ can't arise because of the AFM ordering of nickel moments [61-63]. The transition for smaller rare-earth ions goes from PM metallic phase to PM insulating phase and finally AFM insulating phase with E' AFM ordering of spins defined by wave vector $(\frac{1}{2}, 0, \frac{1}{2})$ in orthorhombic notation. This type of transition for smaller rare earth sizes is continuous in nature (Figure 1.6).

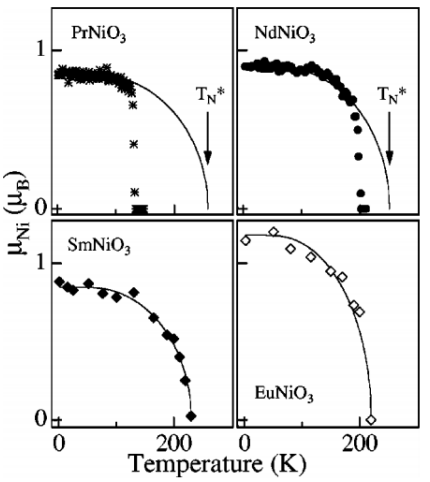

Figure 1.6 First-order nature of the magnetic transition for R = Pr and Nd and, a continuous transition for R = Sm and Eu [Image is taken from reference 62 and used with journals permission].

1.4.2 Thin films of $RNiO_3$

Due to the difficulty in the synthesis of $RNiO_3$ single crystals as well as bulk samples for smaller size rare-earth ions, which demands high pressure and temperature, in absence of such high-pressure annealing (200 bar) the closest system to study the physical properties are thin films. The availability of growth techniques like Off-axis sputtering, Molecular beam epitaxy (MBE), Laser MBE/Pulsed laser deposition (PLD) leads to high-quality films, which allows one to control the sensitive parameters like strain, thickness and heterostructure also [5]. The epitaxial stabilization in the thin films due to the lattice mismatch between film and substrate leads to an additional energy scale in the free energy and hence breaks the threshold for annealing in high oxygen pressure [15]. Transport measurements on $RNiO_3$ film show that the T_{MI} can be strongly tuned by a number of physical parameters like substrate-induced strain (by growing it on different substrates as shown in Figure 1.7), lattice symmetry, carrier doping, thickness, and oxygen vacancies, etc. [64-69]. Due to the degree of epitaxial strain, even the Neel temperature (T_N) can be modified strongly.

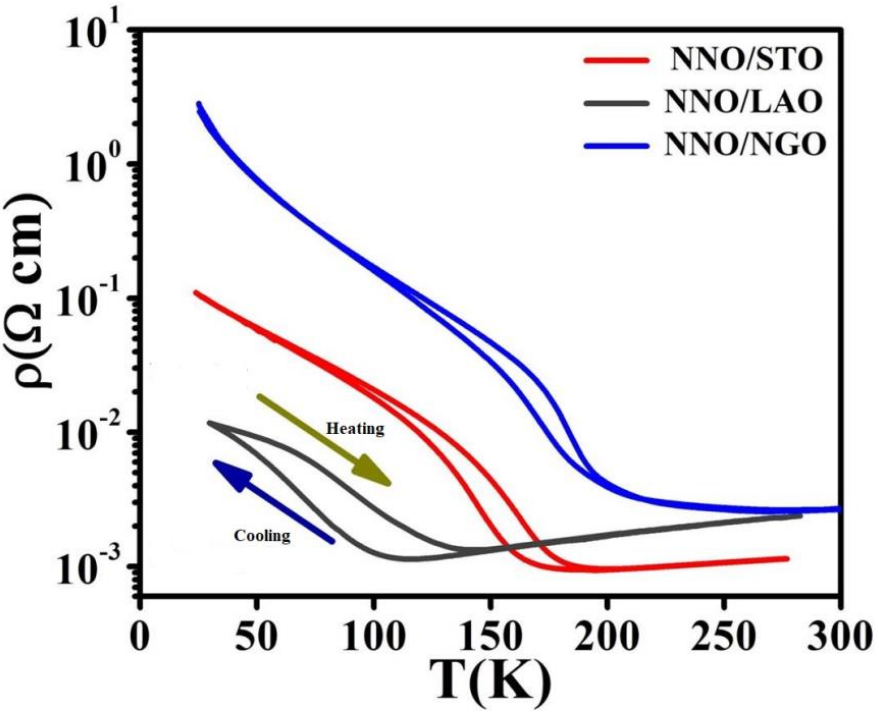

Figure 1.7 Resistivity (ρ) as a function of temperature T for $NdNiO_3$ films grown on $LaAlO_3$ (LAO), $SrTiO_3$ (STO), and $NdGaO_3$ (NGO) single crystal substrates of (100) orientation.

Table 1.1 Factors affecting the T_{MI} in $NdNiO_3$ films: A survey of past studies

Controlling Parameters	Conclusion	Reference
Strain and Thickness	Compressive strain stabilizes metallic state while tensile strain stabilizes the insulating state. Reducing thickness lowers the $T_{MI.}$	Phys. Rev. B 62, 15 (2000)
Field Controlled Strain	Lowering of T_{MI} by 3.3 K due to field-effect compressive strain of 0.25 % produced by PMN-PT substrate.	Sci. Rep. 6, 22228; (2016)
Growth Pressure	Lower growth pressure results in a large compressive strain and hence suppress the T_{MI}	Appl. Phys. Lett. 106, 092104 (2015)
Disorder creates by swift heavy ions	Irradiation by 200 MeV Ag^+ ions induce the stress in $NdNiO_3$ films and suppress the T_{MI}.	J. Appl. Phys. 112, 073718 (2012)
Strain due to $NdNiO_3$ film and substrate lattice mismatch	Compressive strain suppresses the T_{MI} and tensile strain incite the T_{MI}.	J. Appl. Phys. 114, 243713 (2013)
Anisotropic strain	The different orientation of NGO viz. (100), (001) and (110) used for the film growth changes the T_{MI} by nearly 120 K.	Appl. Phys. Lett. 103, 172110 (2013)
Strain and thickness	Cross over from non-fermi liquid to Fermi liquid phase. Predictive criteria for Anderson localization.	Sci. Adv. 2015; 1:e1500797
Lattice symmetry	In the tensile strained film, along with MIT, symmetry lowering structural change occurs, while this change is absent in the compressively strained film.	Sci. Rep. 6, 23652 (2016)
Substrate orientation	The T_{MI} occurs at 335 K by using NGO $(111)_{pc}$ substrate for the growth due to modification of octahedral tilt at the interface.	APL Mat. 3, 062506 (2015)

To summarize, the change in the size of the rare-earth ions, strain, pressure, and doping essentially change the superexchange angle (Ni-O-Ni bond angle) which controls the following physical properties:

- The electronic bandwidth of the bands.
- Magnetic ground state.
- Madelung Potential (The most dominating energy scale exists in a bandgap) [15].

1.4.3 Understanding of MIT in $RNiO_3$

In a completely ionic picture, the ground state electronic configuration of Ni^{3+} in $RNiO_3$ is d^7. Considering the effect of crystal field the Ni^{3+} is considered to be in a low spin state with six electrons in the t_{2g} manifold and one electron in the e_g manifold. According to such electron distribution of Ni^{3+} in t_{2g} and e_g manifold, the Ni^{3+} is a Jahn-Teller (JT) active ion [23]. The half-filled e_g manifold at room temperature gives rise to a metallic state and $RNiO_3$ is expected to undergo a Jahn-Teller distortion to lift the degeneracy. Such uplifting of degeneracy is seen for $RNiO_3$, with smaller rare-earth ions. Surprisingly JT distortion has not been observed for $NdNiO_3$ and $PrNiO_3$ due to their large bandwidth [70-75]. However, it has been observed that the insulating state and symmetry lowering is accompanied by the breathing mode distortion of NiO_6 octahedra which gives rise to the two inequivalent bond length of NiO in the system and hence two different NiO_6 octahedra with a small difference in volume.

To understand these observations, there are various experimental and theoretical reports which exist in the literature are quite debatable. We will highlight a few of them in this section. As mentioned earlier, the d^7 configuration of Ni^{3+} makes it a JT active ion. Further, no more signature of orbital ordering was present. The famous ZSA diagram puts $RNiO_3$ at the boundary between low Δ metals and charge transfer insulator, thus suggesting bad metallic nature of $RNiO_3$ [52]. The isotope experiments done by Medarde and co-workers on $RNiO_3$ suggested that electrons and lattice interactions play an important role (other than bandwidth) and should be taken into account in understanding MIT in Nickelates [40]. Later Ramanathan and co-workers confirm this hypothesis by infrared spectroscopy experiments that show the shifting of spectral weight over an energy scale due to the interaction between electron and lattice [75].

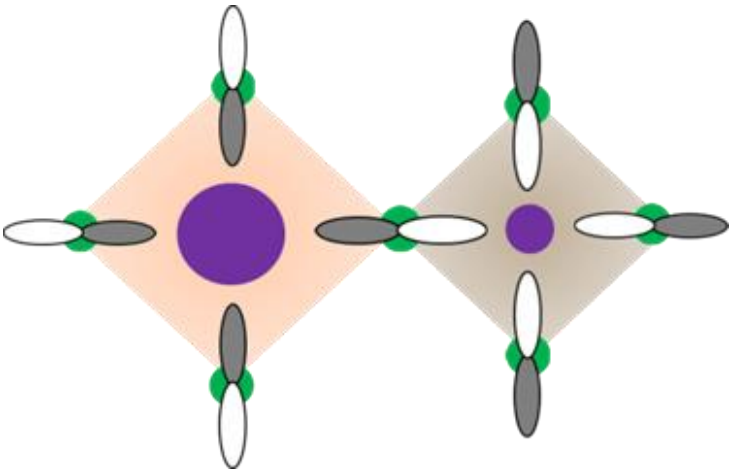

Figure 1.8 Breathing mode distortion of NiO_6 octahedra, the circle represents Ni atom and lobes represent oxygen p orbital. The white portion of lobes show hole in the p orbital.

Theoretical prediction by Khomski and Mazine suggested charge disproportion 2 Ni^{3+} $\rightarrow$

$Ni^{3+\delta}$ + $Ni^{3-\delta}$ at Ni site are responsible for the charge ordering in nickelates [73]. The picture given by Khomski and co-workers ($2d^7 \rightarrow d^8 + d^6$) suggest a transfer of an electron from one Ni site to other Ni site leads to a charge disproportion that gives rise to an insulating state [73]. Experimentally observed value for δ was found to be ~ 0.2e, where e is electronic charge [74]. Further claims by Millis et. al shows there is no charge ordering in $RNiO_3$, the presence of holes in the oxygen leads to an asymmetrical coupling of oxygen (shown in Figure 1.8) and results in a bond disproportion given as [74]

$$(d^{n+1}L)_i + (d^{n+1}L)_j \rightarrow (d^{n+1}L^2)_i + (d^{n+1})_j \qquad (1.5)$$

where i and j represent two different Ni sites and L represents a hole in oxygen. Similar predictions were made by Green and co-workers (as shown in Figure 1.9). The $d^{n+1}L^2$ represent smaller octahedra and d^{n+1} represents bigger octahedra [76]. Further, new theories and new observations are always evolving to understand MIT in $RNiO_3$ [77, 78]. So far the work carried by Millis and Green is considered to be the most successful phenomenon to understand the insulating state of $RNiO_3$. Nevertheless, the exact interpretation of the insulating state is still debatable.

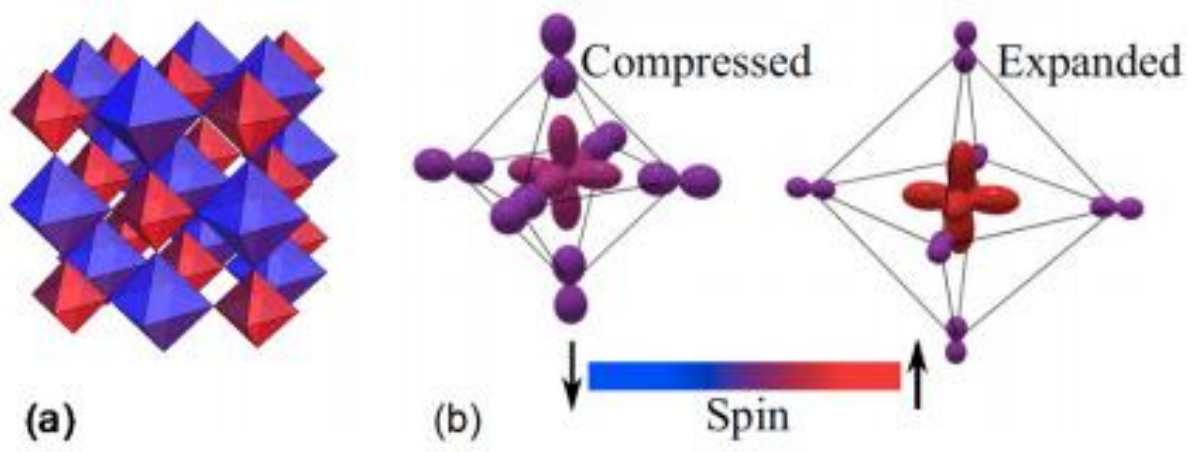

Figure 1.9 (a) Checkerboard arrangement of NiO_6 octahedra, (b) and (c) representation of two inequivalent nickel sites in NiO_6 octahedra representation [Image is taken from reference 76 and used with journals permission].

Interestingly the metallic state of the $RNiO_3$ shows a departure from the classical Boltzmann law and the resistivity power-law follows a T^2 or $T^{5/3}$ behavior. Mikheev et.al shows that depending on the nature of epitaxial strain the temperature exponent can be changed from 5/3 to 2 [67]. Unlike conventional metals where the T^2 term is suppressed due to electron-phonon scattering at high temperature, the T^2 or $T^{5/3}$ term in resistivity along with, saturation resistance fairly explains the metallic behavior in nickelates till high temperature. The $RNiO_3$ thus follows a two channel resistivity model:

$$\frac{1}{\rho} = \frac{1}{\rho_{ideal}} + \frac{1}{\rho_{sat}} \qquad (1.6)$$

Where $\rho_{ideal} = \rho_0 + BT^m$. ρ_{sat} is a parallel high resistance when resistivity approaches the Mott-Ioffe-Regel (MIR) limit and involves a cutoff time for the electrons scattering. The exponent $m = 2$ and 5/3 shows a Fermi Liquid (FL) and a Non-Fermi Liquid (NFL) behavior respectively. The saturation resistivity further depends on the epitaxial strain and is insensitive to disorder [47, 67]. However, the exact origin of such fractional exponent is still not well understood.

1.5 Overview of the thesis

In this thesis, we have looked into some of the basic physics issues that are related to phase co-existence and also the presence of disorder in a correlation driven the transition. We have investigated the nature of MIT in $NdNiO_3$ and $Nd_{0.7}La_{0.3}NiO_3$ thin films. In the case of $Nd_{0.7}La_{0.3}NiO_3$, the substitution of Nd at La site leads to a situation where the MIT as seen in $NdNiO_3$ is gradually suppressed. We have studied that how the nature of transition can be tuned by external stimuli like substrate-induced strain, lattice symmetry, electric field and disorder that have been produced by swift heavy ion irradiation that does not change the stoichiometry of the sample. Further, we show how the correlated fluctuations are observed near MIT. This dissertation used a combination of experimental techniques like temperature dependent electrical resistance (conductance) measurement in the range 300 mK to 300 K (wherever needed), magnetoconductance measurements, temperature dependent Scanning tunneling microscopy and spectroscopy (STM/STS), 1/f noise spectroscopy as well as impedance spectroscopy. The experiments were carried out in the thin films grown by Pulsed laser deposition (PLD) on single crystalline substrates of $LaAlO_3$, $SrTiO_3$, and $NdGaO_3$.

Specifically, we have addressed the following issues:

(I) We have observed the phase co-existence near MIT for a compressively strained $NdNiO_3$ film. We have shown that the observed phase co-existence is dynamic in nature. The STS results reveal that the DOS changes dramatically near the transition. The two co-existing phases have different types of DOS at the E_F. One phase showed a depleted DOS close to E_F with a small yet finite correlation gap (~ 18 meV) while the other co-existing phase showed a metal like DOS that has no depletion. The co-existence of the two phases leads to a jump in the resistance fluctuation (as seen through 1/f noise spectroscopy) at the transition. This has also been corroborated by the Impedance spectroscopy (IS) that shows a broad hump in the capacitance at the transition region. This investigation adds a new dimension to the field of strongly correlated systems and shows that the opening up of depletion in DOS at E_F has a spatial dependence that can co-exist with a normal conducting phase that shows a parabolic dependence of dI/dV.

(II) We also show how factors like biaxial strain, substrate symmetry, and substitutional disorder (induced by isovalent substitution of larger La ions in place of smaller Nd ions) plays important role in the transport properties and can change the nature of MIT. The combination of these factors makes substituted nickelates ($Nd_{0.7}La_{0.3}NiO_3$) undergo a continuous transition as seen in systems undergoing disorder/composition driven Anderson transition. We establish a cross-over from a Positive Temperature Coefficient (PTC) resistance regime to Negative Temperature Coefficient (NTC) resistance regime does not necessarily constitute an MIT since the extrapolated conductivity at zero temperature ($\lim_{T\to 0} \sigma = \sigma_0$) though small is finite, which shows a signature of the bad metallic state as well as an absence of an activated transport.

(III) Application of a bias current (and hence field) leads to suppression of the electrical resistance of the insulating state in $NdNiO_3$ films thus leading to large electroresistance. The resistivity measurement at different currents shows suppression of resistivity by nearly an order without affecting the metal-insulator transition temperature. To rule out the possibility of Joule heating as a cause of electroresistance, we have performed current-induced resistivity switching measurement with low duty cycle. The continuous I-V and pulsed I-V measurement show absence of Joule heating contribution below a critical current/power dissipation. Thermal modelling shows that even at highest current bias, the maximum temperature rise is nearly 12 K, which is insufficient for such a change in resistivity by nearly an order. The results thus suggested that the observed effects are due to the intrinsic electroresistance effect in the $NdNiO_3$ film. We discuss a certain scenario like the phase co-existence of the high temperature metallic and low temperature insulating filaments that may lead to this observation.

(IV) Presence of disorder in a system undergoing a correlation driven transition is a topic of considerable current interest. We showed that the introduction of disorder in a controlled way using swift heavy ion interaction suppresses the correlation driven MIT and makes the system looks like a heavily disordered metal governed by weak localization. The disorder (atomic displacement up to 2% of the total atoms) in the $NdNiO_3$ films was created using 1 MeV Ar^{4+} ion irradiation. The extent of disorder was varied by different

irradiation time. We show, that the pristine film shows an MIT at 180 K and consistent with the Mott type behavior of the MIT. At low temperature, such a film shows Variable Range Hopping (VRH) with conductivity $\sigma \rightarrow 0$ at T=0. For disorder, up to 1% of displaced atoms or lower the insulating state is suppressed and the system shows a weak localization behavior with $\sigma \neq 0$ at T=0. Supporting evidence from Raman spectroscopy as well as X-Ray studies show that these effects of Anderson transition and proximity to a disordered metallic state persist till the basic integrity of the NiO_6 octahedra is preserved.

We have arranged the thesis in the following chapters:

Chapter 1: Introduction

Chapter 2: Sample preparation, characterization, and measurement techniques

Chapter 3: Phase co-existence near the metal insulator transition

Chapter 4: Continuous transition from weak localized regime to a strongly localized regime in $Nd_{0.7}La_{0.3}NiO_3$ films

Chapter 5: Electroresistance in $NdNiO_3$ films

Chapter 6: Disorder induced signature of Anderson transition in a Mott system

Chapter 7: Conclusion and Future directions

Appendix A: Low-temperature structural studies of $Nd_{0.7}La_{0.3}NiO_3$ nanoparticles

Appendix B: Reciprocal space mapping data for different nickelates films

Appendix C: Resistance as a function of current for $NdNiO_3$ film grown on $SrTiO_3$ (100) substrate

Bibliography for Chapter 1

1. J. B. Torrance, P. Lacorre, A. I. Nazzal, E. J. Ansaldo, and Ch. Niedermayer, Phys. Rev. B 45, 8209 (1992).
2. Arnulf Möbius, Critical Reviews in Solid State and Materials Sciences 0,1-55 (2017).
3. A. K. Raychaudhuri, Adv. Phys. 44, 21 (2006).
4. G. Catalan, Phase Trans. 81, 729, (2008).
5. S. Catalano, M. Gibert, J. Fowlie, J. Íñiguez, J. M. Triscone, and J. Kreise, Rep. Prog. Phys. 81, 046501, (2018).
6. W. Yamaguchi, O. Shiino, T. Endo, K. Kitazawa, and T. Hasegawa, Appl. Phys. Lett. 76, 517 (2000).
7. N. F. Mott, Metal-Insulator Transition. Taylor & Francis, London (1990).
8. M. Imada, A. Fujimori, and Y. Tokura, Metal-insulator transitions, Rev. Mod. Phys. 70, 1039 (1998).
9. V.F. Gantmakher, Electrons and Disorder in Solids Clarendon Press Oxford (2005).
10. Daniel I. Khomskii, Transition Metal Compounds, Cambridge university press
11. G. Catalan, Progress in perovskite nickelate research, Phase Trans. **81,** 729-749, (2008).
12. P. A. Lee and T. V. Ramakrishnan, Rev. Mod. Phys.57 287 (1985).
13. R Scherwitzl, Metal-insulator transitions in nickelate heterostructures, Ph.D. thesis, University of Geneva (2012).
14. M. L. Medarde, J. Phys.: Condens. Matter 9 1679 (1997).
15. S. Middey, J. Chakhalian, P. Mahadevan, J. W. Freeland, A. J. Millis and D. D. Sarma, Annual Review of Materials Research vol 46, ed D R Clarke (2016)
16. N. Gayathri, A. K. Raychaudhuri, X. Q. Xu, J. L. Peng, and R. L. Greene, J. Phys. Condens. Matter **10,** 1323 (1998).
17. G. Catalan, R. M. Bowman, and J. M. Gregg, Metal-insulator transitions in $NdNiO_3$ thin films, Phys. Rev. B **62**, 7892 (2000).
18. E. Mikheev, A. J. Hauser, B. Himmetoglu, N. E. Moreno, A. Janotti, C. G. Van de Walle and S. Stemmer, Sci. Adv. **10,** 1500797 (2015).
19. S. Heo, C. Oh, M. J. Eom, J. S. Kim, J. Ryu, J. Son, and H. M. Jang, Sci. Rep. **6**, 22228 (2016).

20. Y. Kumar, R. J. Choudhary, and R. Kumar, J. Appl. Phys. **112**, 073718 (2012).
21. A. K. Raychaudhuri, K. F. Rajeev, H. Srikanth, and N. Gayathri, Phys. Rev. B **51**, 12 (1995).
22. Jian Liu Mott Transition and Electronic Structure in Complex Oxide Heterostructures Ph.D. thesis, University of Arkansas, Fayetteville (2012).
23. Sagar Sarkar, Role of structure in determining the properties of transition metal/post-transition metal compounds, Ph.D. thesis, University of Calcutta, India (2018).
24. E. J. Moon, B. A. Gray, M. Kareev, J. Liu, S. G. Altendorf, F. Strigari, L. H. Tjeng, J. W. Freeland, and J. Chakhalian, New J Phys 13 073037 (2011).
25. R. S. Bisht, S. Samanta, and A. K. Raychaudhuri, Phys. Rev. B 95 115147 (2017).
26. Ali M. Alsaqqa, Sujay Singh, S. Middey, M. Kareev, J. Chakhalian, and G. Sambandamurthy, Phys. Rev. B 95, 125132 (2017).
27. G. Mattoni, P. Zubko, F. Maccherozzi, A. J. H. van der Torren, D.B. Boltje, M. Hadjimichael, N. Manca1, S. Catalano, M. Gibert, Y. Liu, J. Aarts, J. M. Triscone, S. S. Dhesi, and A. D. Caviglia, Nat. Commun. **7**, 13141 (2016).
28. K. W. Post, A. S. McLeod, M. Hepting, M. Bluschke, Yifan Wang, G. Cristiani, G. Logvenov, A. Charnukha, G. X. Ni, Padma Radhakrishnan, M. Minola, A. Pasupathy, A. V. Boris, E. Benckiser, K. A. Dahmen, E. W. Carlson, B. Keimer and D. N. Basov, Nature Physics 14, 1056–1061 (2018).
29. Jennifer Fowlie, https://doi.org/10.1007/978-3-030-15238-3
30. https://en.wikipedia.org/wiki/Calcium_titanate
31. David B. Mitzi, Introduction: Perovskites, Chem. Rev. 119, 5, 3033 (2019).
32. Asish K. Kundu and B. Raveau, Structural, Magnetic and Electron Transport Properties of Ordered-Disordered Perovskite Cobaltites, Perovskites: Structure, Properties, and Uses.
33. A Glazer, Acta Crystallogr. A, 31 756 (1975).
34. A Glazer, Acta Crystallogr. B, 28 3384 (1972).
35. J.B. Torrance, P. Lacorre, A.I. Nazzal, E.J. Ansaldo, and C. Niedermayer, Phy. Rev. B 45, 8209 (1992).
36. J. Garcia-Munoz, J. Rodriguez-Carvajal, P. Lacorre, and J.B. Torrance, Phys. Rev. B 46, 4414–4425 (1992).

37. J.A. Alonso, M.J. Martı´nez-Lope, M.T. Casais, J.L. Garcia-Munoz, and M.T. Fernandez-Diaz, Phys. Rev. B 61, 1756–1763 (2000).
38. R. D. Shannon, Acta Cryst. A 32(5) 751 (1976).
39. F. Capon, P. Ruello, J.-F. Bardeau, P. Simon, P. Laffez, B. Dkhil, L. Reversat, K. Galicka, and A. Ratuszna, J. Phys. Condens. Matter 17, 1137–1150 (2005).
40. M. Medarde, P. Lacorre, K. Conder, F. Fauth, and A. Furrer, Phys. Rev. Lett. 80, 2397, (1998).
41. P.C. Canfield, J.D. Thompson, S.W. Cheong and L.W. Rupp, Phys. Rev. B 47, 12357, (1993).
42. X. Obradors, L.M. Paulius, M.B. Maple, J.B. Torrance, A.I. Nazzal, J. Fontcuberta, and X. Granados, , Phys. Rev. B 47, 12353–12356 (1993).
43. J.-S. Zhou, J.B. Goodenough, and B. Dabrowski, Phys. Rev. Lett. 94, 226602, (2005).
44. M. Medarde, J. Mesot, P. Lacorre, S. Rosenkranz, P. Fischer, and K. Gobrecht, Phys. Rev. B 52, 9248–9258, (1995),
45. S. Ishiwata, M. Azuma, M. Hanawa, Y. Moritomo, Y. Ohishi, K. Kato, M. Takata, E. Nishibori, M. Sakata, and I. Terasaki, Phys. Rev. B 72, 045104 (2005).
46. M. Amboage, M. Hanfland, J.A. Alonso, and M.J. Martinez-Lope, J. Phys. Condens. Matter 17, S783–S788 (2005).
47. S. Stemmer and S. J. Allen, Rep. Prog. Phys. 81, 062502 (2018).
48. M.A. Novojilov, O.Yu. Gorbenko, I.E. Graboy, A.R. Kaul, H.W. Zandbergen, N.A. Babushkina, and L.M. Belova, Appl. Phys. Lett. 76, 2041 (2000).
49. A. Tiwari, C. Jin, and J. Narayan, Appl. Phys. Lett. 80 4039 (2002).
50. P. Goudeau, P. Laffez, A. Zaghrioui, E. Elkaim, and P. Ruello, Crys. Eng. 5, 317–325, (2002).
51. Patrik Fazekas, Lecture Notes on Electron Correlation and Magnetism
52. J. Zaanen, G. A. Sawatzky and J. W. Allen, Phys. Rev. Lett. 55, 418, (1985).
53. A K Raychaudhuri, Adv. Phys. 44, 21 (2006).
54. A. L. Efros and M. Pollak, Electron-Electron interaction in disordered systems (1985).
55. P. Lacorre, J.B. Torrance, J. Pannetier, A.I. Nazzal, P.W. Wang, and T.C. Huang, J. Solid State Chem. 91, 225, (1991).
56. S. J. Kim, G. Demazeau, J.A. Alonso, and J.-H. Choy, J. Mater. Chem. 11, 487 (2001).

57. S. Ishiwata, M. Azuma, M. Takano, E. Nishibori, M. Takata, M. Sakata, and K. Kato, J. Mater. Chem. 12, 3733, (2002).
58. M. Zaghrioui, A. Bulou, P. Lacorre, and P. Laffez, Phys. Rev. B 64, 081102 (R) (2001).
59. J. L. García-Muñoz, M. A. G. Aranda, J. A. Alonso, and M. J. Martínez-Lope, Phys. Rev. B 79 134432 (2009).
60. https://en.wikipedia.org/wiki/Vegard%27s_law
61. J.L. Garcia Munoz, J. Rodriguez-Carvajal, and P. Lacorre, Europhys. Lett. 20, 241–247 (1992).
62. I. Vobornik, L. Perfetti, M. Zacchigna, M. Grioni, G. Margaritondo,J. Mesot, M. Medarde and P. Lacorre, Phys. Rev. B 60, R8426 (1999).
63. M.A. Mogrinski, N.E. Massa Horacio Salva, J.A. Alonso, and M.J. Martinez-Lope, Phys. Rev. B 60, 5304 (1999).
64. S. Heo, C. Oh, M. J. Eom, J. S. Kim, J. Ryu, J. Son, and H. M. Jang, Sci. Rep. 6 22228, (2016)
65. Y. Kumar, R. J. Choudhary, and R. Kumar, J. Appl. Phys.112 073718 (2012).
66. G. Catalan, R. M. Bowman, and J. M. Gregg, Phys. Rev. B 62 7892 (2000).
67. E. Mikheev, A. J. Hauser, B. Himmetoglu, N. E. Moreno, A. Janotti, C. G. Van de Walle, and S. Stemmer, Sci. Adv. 1 e1500797 (2015).
68. J. Y. Zhang, H. Kim, E. Mikheev, A. J. Hauser and S. Stemmer, Sci. Rep. 6 23652 (2016).
69. S. Das S, V. E. Phanindra, S. S. Philip, and D. S. Rana, Phys. Rev. B 96 144411 (2017).
70. J. S. Zhou and J.B. Goodenough, Phys. Rev. B 69, 153105 (2004).
71. M. Zaghrioui, A. Bulou, P. Lacorre, and P. Laffez, Phys. Rev. B 64, 081102 (2001).
72. U. Staub, G.I. Meijer, F. Fauth, R. Allenspach, J.G. Bednorz, J. Karpinski, S.M. Kazakov, L. Paolasini, and F. dacapito, Phys. Rev. Lett. 88, 126402 (2002).
73. I. I. Mazin, D. I. Khomskii, R. Lengsdorf, J. A. Alonso, W. G. Marshall, R. M. Ibberson, A. Podlesnyak, M. J. Martinez-Lope, and M. M. Abd-Elmeguid, Phys. Rev. Lett. 98, 176406 (2007).
74. H. Park, A. J. Millis, and C. A. Marianetti, Phys. Rev. Lett. 109, 156402 (2012).
75. R. Jaramillo, S.D. Ha, D. M. Silevitch, and S. Ramanathan, Origins of bad metal conductivity and the insulator-metal transition in the rare-earth nickelates, Nat. Phys. **10**, 304 (2014).

76. R. J. Green, M. W. Haverkort, and G.A. Sawatzky, Phys. Rev. B 94 195127 (2016)
77. Alain Mercy, Jordan Bieder, Jorge Íñiguez, and Philippe Ghosez, Nature Communications | 8: 1677 (2017)
78. Oleg E. Peil, Alexander Hampel, Claude Ederer, and Antoine Georges, Phys. Rev. B 99, 245127 (2019).

Chapter 2 Sample preparation, characterization and measurement techniques

In this chapter, we discuss the growth and characterization of different samples prepared along with the measurement techniques used for different work. The powder samples/pellets were prepared by the sol-gel method and the thin films were prepared by Pulsed laser deposition.

2.1 Introduction

This thesis discusses the investigation of metal-insulator transition (MIT) in rare-earth nickelates ($RNiO_3$). To answer some of the basic physics issues in the context of rare earth nickelates, we have grown the thin films (different thickness) and nanopowder of the different nickelates, in particular, Lanthanum (La) and Neodymium (Nd) based. Most of the observations in this thesis has been made on the thin films of the $NdNiO_3$ and $Nd_{0.7}La_{0.3}NiO_3$. Further to prepare a good film, a good target material is necessary as all the films used in the thesis has been made by the laser ablation method. Thus an extensive characterization is much needed to confirm the formation of a right phase.

In this thesis, we have adopted the sol-gel method for preparing the nanoparticles followed by high temperature sintering to make a target material for the pulsed laser deposition (PLD). The phase formation was checked by X-ray diffraction (XRD), Rietveld analysis, Raman spectroscopy and Transmission electron microscopy (TEM). The composition was checked by the Energy-dispersive x-ray spectroscopy (EDX). The thickness of the films was measured by cross-sectional Scanning electron microscope (SEM) and in situ by reflection high energy electron diffraction. The surface topography was checked using an atomic force microscope (AFM).

The films used in the thesis were grown on a single crystal substrate of $SrTiO_3$, $LaAlO_3$, and $NdGaO_3$. The choice of substrates was made to modify the built-in strain and as well as the interfacial change in symmetry due to the different symmetry of the substrates and films. To induce the disorder in films, the ion irradiation was performed at low energy ion beam facility, IUAC Delhi.

The electrical and magnetic transport data were taken in a He-3, He-4, and liquid nitrogen (LN_2) based cryostats with a magnetic field of 10 Tesla. The Scanning tunneling spectroscopy (STS) was performed in a commercial Scanning probe microscopy (SPM) unit from RHK. The impedance and 1/f noise spectroscopy were done in a homemade LN_2 cryostat. All the instruments and setups were calibrated with standard samples before the measurements. All the required data acquisition and analysis programs were written in either C/C++, Labview or Matlab. In upcoming sections, we will briefly discuss these techniques.

2.2 Synthesis of $NdNiO_3$ and $Nd_{1-x}La_xNiO_3$ ($x \geq 0.1$) Nanopowder and Pellet

The growth of nickelates is challenging, as the Ni (Nickel) valence requires high oxygen pressure to stabilize the +3 oxidation states. Further, the solid-state reaction method requires a much higher temperature and pressure for the phase formation of the nickelates. Due to the unavailability of the high pressure (200 bar) oxygen [1, 2], the $Nd_{1-x}La_xNiO_3$ nanoparticles used in this thesis were made by polymeric precursor synthesis route. We will now discuss the synthesis process in details.

The stoichiometric amount of high purity (> 99.9 %) precursors of Lanthanum nitrate hexahydrate, Neodymium nitrate hexahydrate, and Nickel acetate tetra-hydrate were dissolved in 1:1 acetic and deionized (DI) water solution in a beaker. The appropriate amount of ethylene glycol was added to the solution. The water and ethylene glycol ratio play an important role in determining the particle size of the specimen [3]. In the present work, we have used 1.5 times of ethylene glycol with respect to the DI water. The molarity of the precursor solution was 0.2 M to 0.4 M. The solution was stirred at 70^0 C for 2 hours and 6 hours at room temperature, respectively, in a hot plate equipped with a magnetic stirrer. After 6 hours, the solution was heated until the formation of sol. The sol was allowed to dry and kept at 150^0 C for 12 hours followed by pyrolysis at 350^0 C and 450^0 C for 1.5 and 1 hour, respectively. The final heating for the phase formation was done at 650^0 C for 8 hours in a flow of ultra-high purity oxygen gas. The advantage of this method is to get a uniform and homogeneous dispersion of the nanoparticles.

To make the target material for the Pulsed laser deposition (PLD), the as-prepared nanopowder was pressed into a pellet with 80 MPa pressure and sintered at 800^0 C in a tubular furnace with a high oxygen flow for 24 hours. The pellet was ground and again sintered at 800^0 C in high oxygen flow for 24 hours. This step was followed 7 times and finally, the sintered pellet was kept in a high flow of oxygen at 650 ^{0}C for 24 hours to maintain oxygen stoichiometry. The as-obtained nanopowder and pellets were characterized extensively before using it for the experiments. The detailed characterization of the powder and pellets are given in the later section. In Figure 2 (a) and (b) we show the actual synthesis process followed by the flow chart for the synthesis of nickelates nanoparticles and pellet.

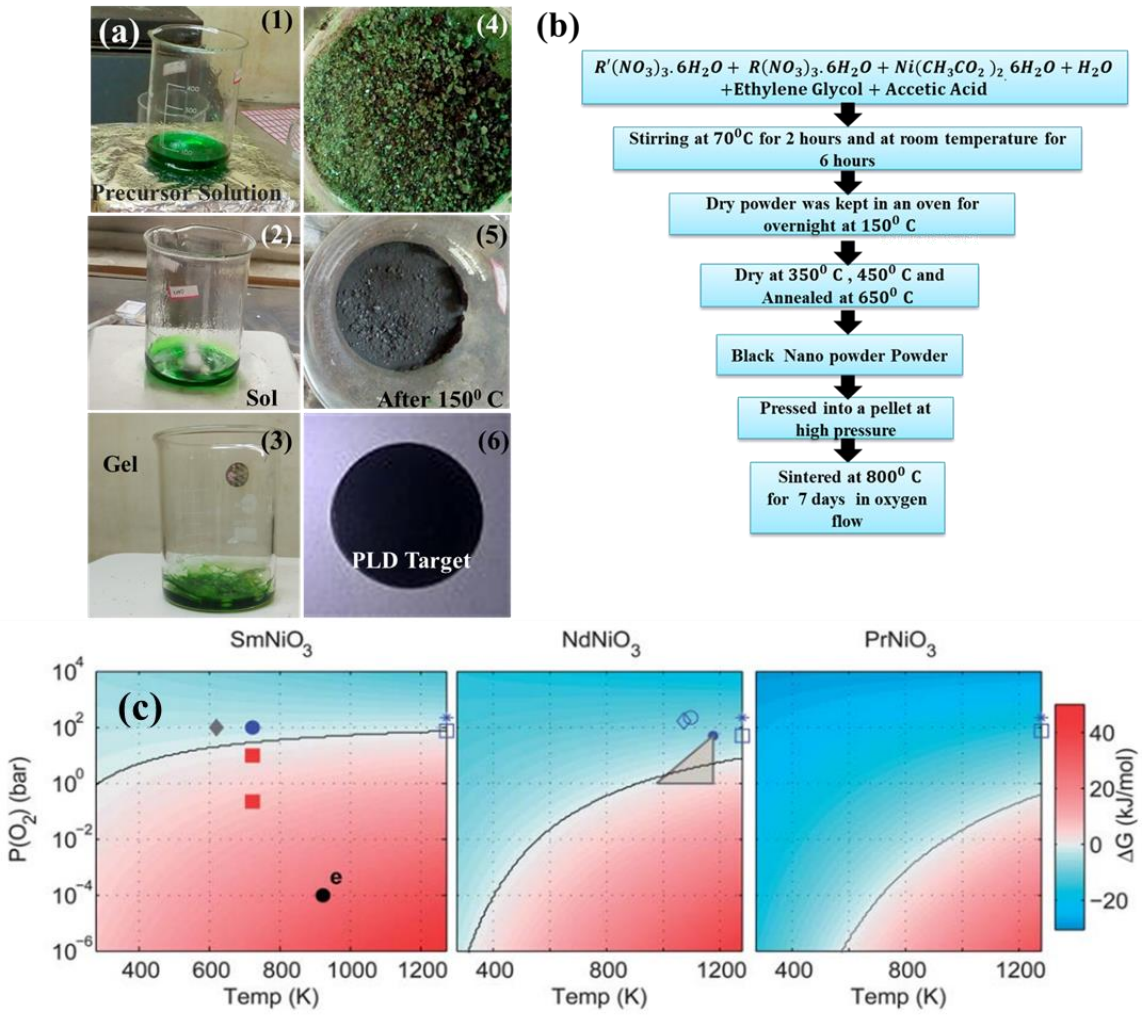

Figure 2 (a) The experimental process for making the $Nd_{1-x}La_xNiO_3$ nanopowder and Pellet, (b) The flow chart for the synthesis and (c) Proposed thermodynamic stability phase diagram for different nickelates. Our synthesis method agrees with the proposed phase diagram for $NdNiO_3$ (Image used from reference 2 with permission of the author).

2.3 Growth of $Nd_{1-x}La_xNiO_3$ thin films

To grow the thin films of nickelates, we have adopted the method of physical vapor deposition (PVD). In particular, we have chosen Pulsed laser deposition (PLD). Venkatesan and co-workers first used the laser ablation technique to deposit the thin film of a high-temperature superconductor [4]. Since this technique is being used widely for the film growth of complex oxides. In PLD a pulse excimer laser is focused on the target material/pellet. The high-energy laser pulse ablates the target material, which in the presence of oxygen/vacuum leads to the formation of a plasma plume

containing ions, molecules, electrons, etc. The plasma plume formed due to the ablation flows in a perpendicular direction to the substrate and the accumulation of materials ablated from the laser pulse results in the growth of films on the substrates. Unlike the evaporation technique, this technique plays an important role in the deposition of thin films of complex oxides, which is not possible in thermal/evaporation where the stoichiometry is often limited due to different vapor pressure of different specimen. Another advantage of this technique is that one can really grow a thin film layer by layer.

The full process of thin films growth by PLD process can be described as follows:

1. Laser pulse and target material interaction.
2. Formation of plasma plume due to the ablated material during laser irradiation.
3. Slowing down of the plasma plume in a background oxygen gas.
4. Collection of the ablated material on the substrate.
5. Nucleation at the substrate, which results in the thin film growth.

In this thesis, we have used coherent COMPex pro 201F KrF excimer laser of wavelength 248 nm for the film growth [6]. Depending on the laser energy and the spot size of the laser, an associated value of energy per unit area called fluence was optimized for the film growth. In Figure 2.1 (a) and (b), we show the formation of dark spots due to the laser on a laser sensitive paper. Figure 2.1 (a) and (b) shows the formation of dense dark and uniform spots on the encircled regions with respect to the whole area. In order to achieve uniformity in the films, these dark and uniform spots positions were used as a marker to mount the substrates before the deposition. To perform layer-by-layer growth we have used Reflection high-energy electron diffraction (RHEED) gun, which is equipped with our PLD chamber. In RHEED, a beam of electrons (energy 35 kV) generated by the electron gun hits the sample surface at a grazing angle, where the electrons diffract from the sample surface (As shown in Figure 2.2(a)). A small fraction of electrons interfere constructively and leads to the diffraction pattern, which can be captured at the detector [7].

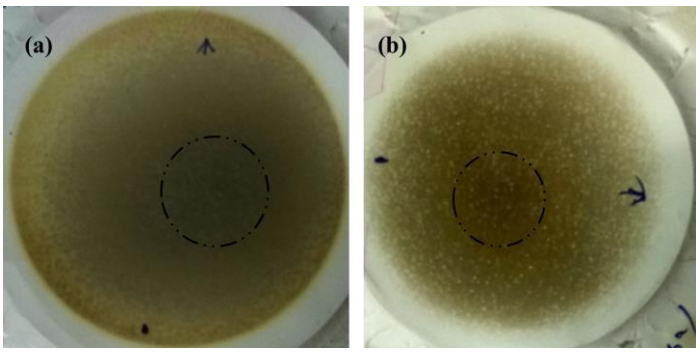

Figure 2.1 (a) The dark and uniform spots on a laser sensitive paper from the ablation of (a) $NdNiO_3$ and (b) $Nd_{0.7}La_{0.3}NiO_3$ target.

For thin films prepared in this thesis, we have used nearly 4000 laser shots with a repetition rate of 5 Hz and 1500/1200 laser shots with a repetition rate of 5/3 Hz to grow films of thickness nearly 80 nm and 15 nm respectively. The target pellets were ablated before all the deposition in order to remove surface contamination due to other depositions in the PLD chamber and a pre annealing was performed for 15 minutes to achieve a thermal equilibrium between substrates and the heater. To maintain the oxygen stoichiometry, after the deposition, the as-grown films were cooled in situ in the presence of 1 bar ultra-high purity oxygen gas. Figure 2.2 (b) shows the growth of 25 Unit Cell (UC) (nearly 10 nm) thickness $NdNiO_3$ film on $SrTiO_3$ (100) single crystal substrate.

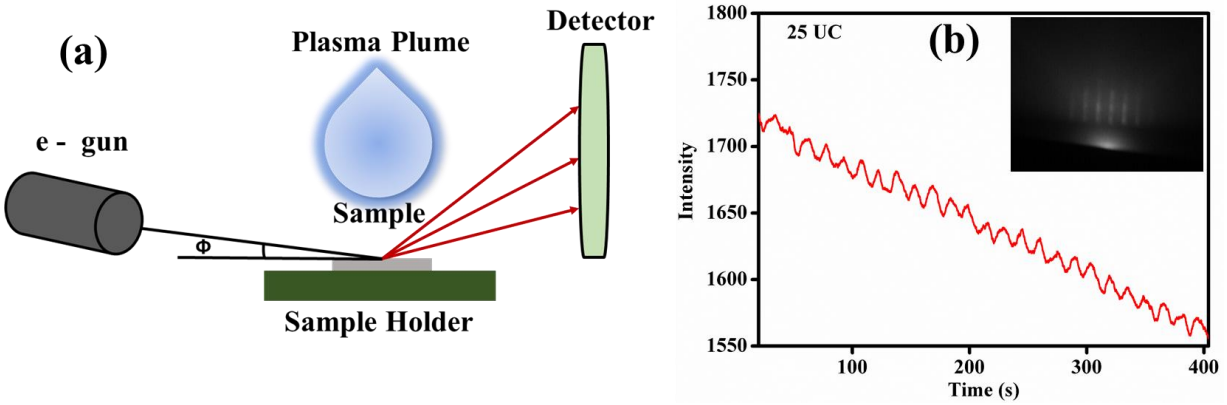

Figure 2.2. (a) The Schematic of RHEED set up and (b) The RHEED oscillations of 25 UC $NdNiO_3$ film deposited on $SrTiO_3$ single crystal substrate on the application of 1000 laser shots. Inset shows the electron diffraction pattern.

2.4 Characterization of $Nd_{0.7}La_{0.3}NiO_3$ and $NdNiO_3$ nanopowder/films

2.4.1 X-Ray Diffraction

For any material, the primary characterization is X-ray Diffraction (XRD) to understand the crystal structure, crystallinity, and phase identification. X-ray diffraction is a non-destructive tool widely used in material characterization. From diffraction theory, we know that electromagnetic radiation will diffract only if the wavelength (λ) of the electromagnetic radiation will be of the order of spacing of the grating. When a monochromatic beam of X-rays falls on a crystal, due to the interaction of oscillating electric field and an electronic cloud of periodic atoms, the X-rays will scatter. However due to the regular/periodic arrangement of atoms, in some direction, the interference will be constructive while in other direction the interference will be destructive [8, 9]. The constructive interference leads to a situation when the outgoing X-rays are in phase and the path difference varies by an integer number of the wavelengths. The equation is given as

$$n\lambda = 2d\sin\theta \qquad (2.1)$$

, known as Braggs law. Here n represents the order of reflection, θ is the angle between Bragg planes and incoming X-rays, λ is the wavelength of X-ray used, and d represents inter-planar spacing. In this thesis, we have used PANalytical X-PERT Pro and Rikagu diffractometer for the XRD of films and powder samples, respectively (As shown in Figure 2.3 (c) and (d)). We have also used synchrotron-based XRD for the characterization of powder samples. In Figure 2.3, we present the XRD data for the different samples. To check the orientation of the films we have performed the high-resolution XRD rocking analysis. In the rocking curve, we have fixed the detector at the center of films Bragg reflection and followed the diffraction intensity of the sample while it is rocked [9, 10].

In lab XRD, we have used an X-ray of wavelength 1.54 angstrom while for the synchrotron XRD we have used a wavelength of 0.98 angstrom. The synchrotron data was taken at the KEK photon factory Japan. In Figure 2.3 (a) and (b), the Rietveld refinement for $NdNiO_3$ and $Nd_{0.7}La_{0.3}NiO_3$ shows that the structure follows a Pbnm symmetry at room temperature. In Table 2, we summarize

the lattice parameters of the $NdNiO_3$ and $Nd_{0.7}La_{0.3}NiO_3$ nanopowder after Rietveld refinement. The obtained lattice parameters match fairly with the numbers reported in the literature [1].

Table 2 Obtained lattice parameters from Rietveld refinement

Lattice Parameter (angstrom)	$NdNiO_3$	$Nd_{0.7}La_{0.3}NiO_3$
a	5.415	5.455
b	5.363	5.378
c	7.619	7.610

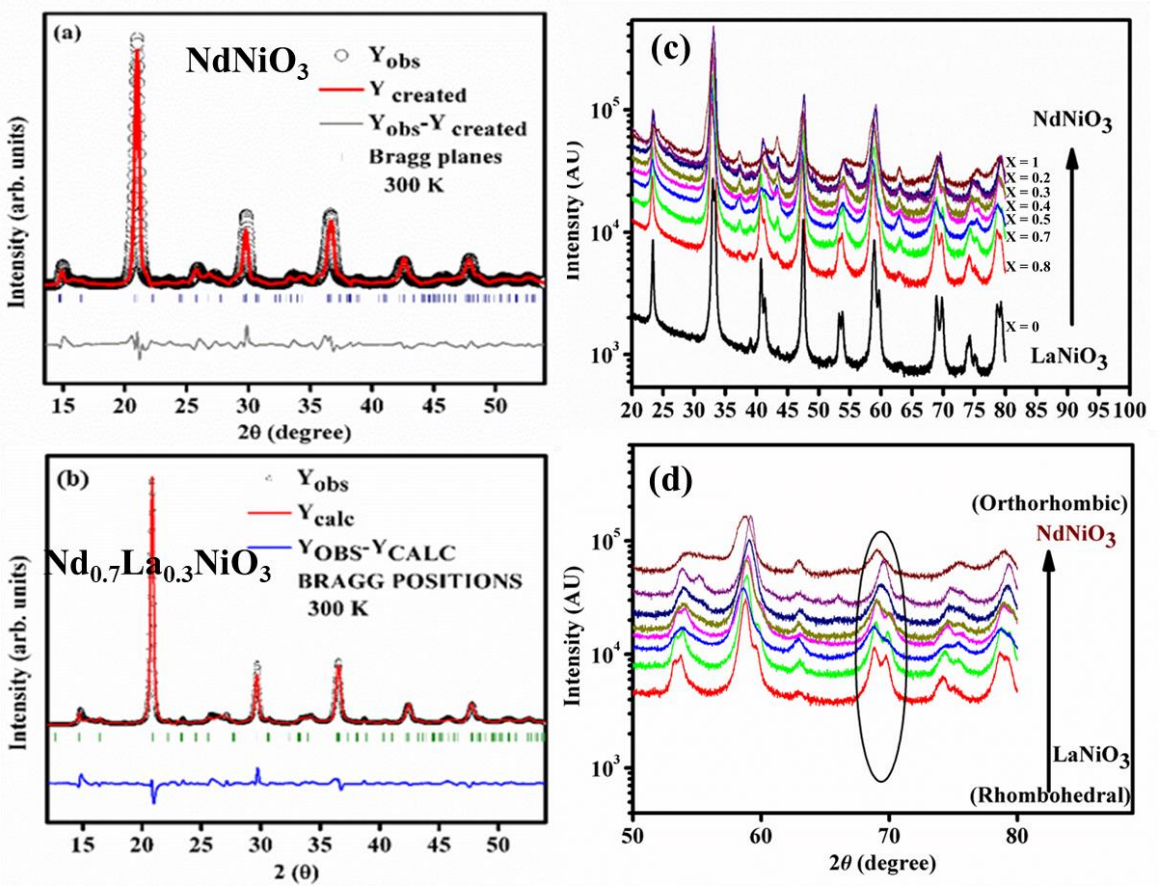

Figure 2.3 (a) Synchrotron XRD of the (a) $NdNiO_3$ and (b) $Nd_{0.7}La_{0.3}NiO_3$ nanoparticles. The Rietveld refinement shows that both the nanoparticles have an orthorhombic (Pbnm) symmetry. (c) The XRD pattern of $Nd_xLa_{1-x}NiO_3$ (x= 0 to 1) taken in lab X-ray, the merging of 2 peaks to a single peak near 69^0 shows a transition from rhombohedral to orthorhombic phase, and (d) Zoomed image of (c) near 69^0.

2.4.2 Scanning Electron Microscope and Energy Dispersive X-ray Spectroscopy

In the Scanning electron microscope (SEM), unlike an optical microscope, an electron beam is used to achieve the images, topography, and morphology of the specimen under test. In our SEM (Quantum FEG 250), a field emission gun was used to generate an electron beam. The electron beam travels through a vacuum and after passing through a set of the condenser lens, it is focussed on the sample. These electrons undergo inelastic and elastic interactions, which result in the spreading out of electrons into the materials [11]. In this process, some electrons fly back to the vacuum, which is backscattered electrons while some lose their energy and results in the emission of secondary electrons and X-ray, etc. The secondary electrons are detected by the detectors and used for information about specimen surface topography. Along with the topography, we have also used the cross-sectional SEM to determine the thickness of our films as shown in Figure 2.4.

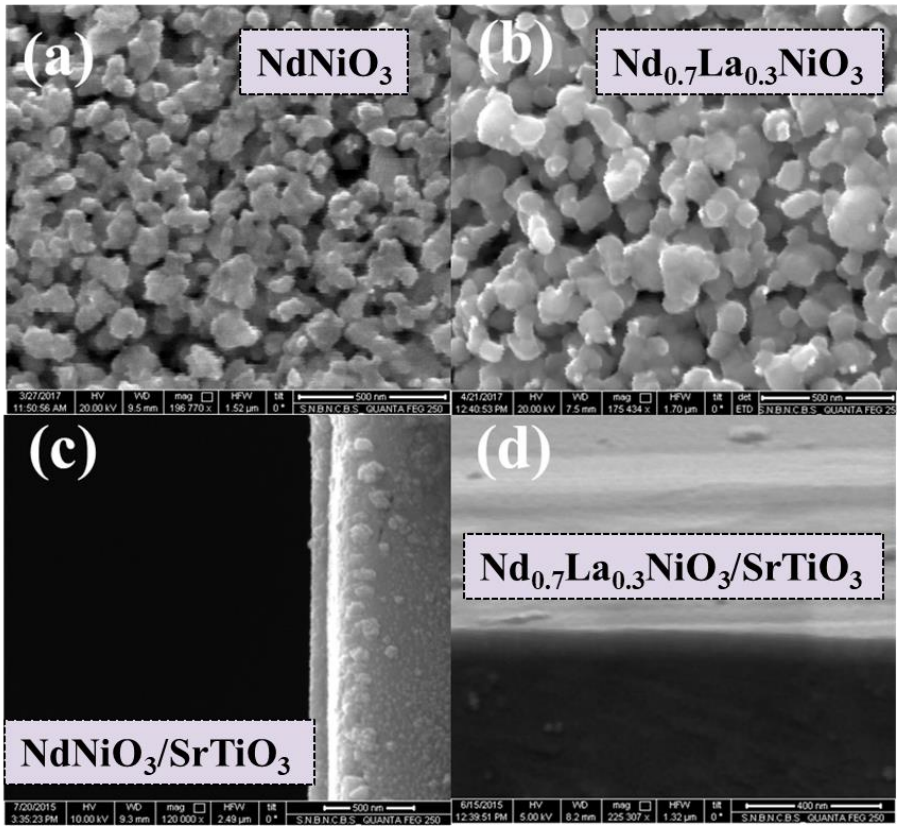

Figure 2.4 (a) The as-prepared nanoparticles of (a) $NdNiO_3$, (b) $Nd_{0.7}La_{0.3}NiO_3$, (c) and (d) Cross-sectional SEM image of nearly 80 nm thick film of $NdNiO_3$ and $Nd_{0.7}La_{0.3}NiO_3$ on $SrTiO_3$ (100) single crystal substrate.

Further, when an electron beam interacts with the samples it can eject an electron from the inner shell and creates a hole. The hole can be filled by higher-energy electrons from another shell, which results in the emission of X-ray. The energy released in the form of X-ray in this process can be measured by the energy dispersive spectrometer [12]. This is known as energy dispersive X-ray spectroscopy and used in determining the elemental composition of the specimen. In Figure 2.5 (a) and (b) we show the EDS spectra for the as-prepared nanoparticles. The atomic percentage shows that the samples are highly stoichiometric and there is no oxygen deficiency. The stoichiometry was checked for the films also.

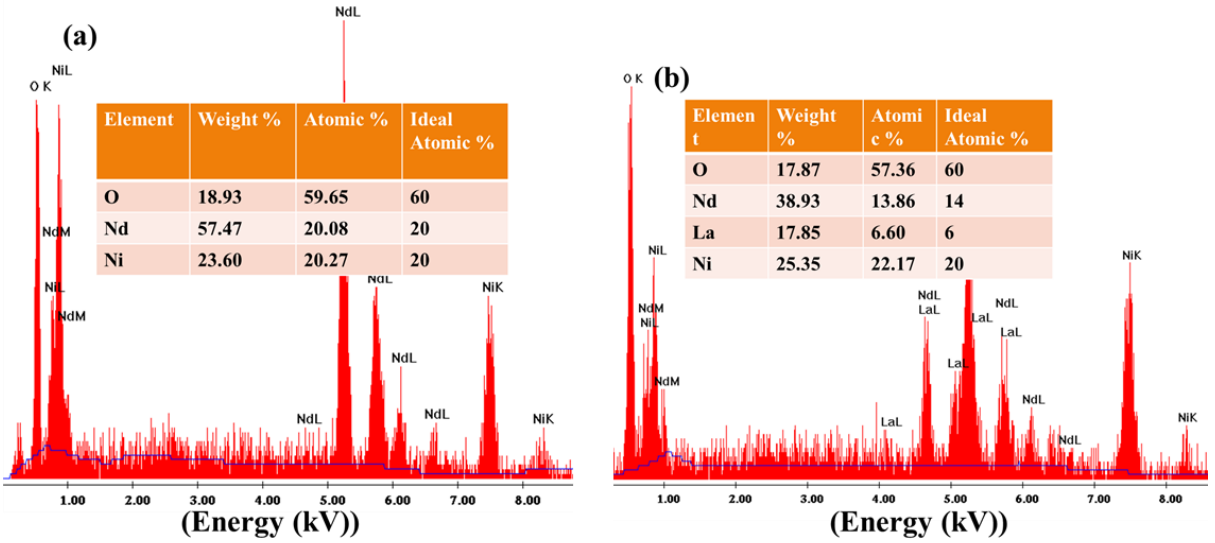

Figure 2.5 EDS spectra and elemental composition of as-prepared nanoparticles of (a) $NdNiO_3$ and (b) $Nd_{0.7}La_{0.3}NiO_3$

2.4.3 Transmission Electron Microscope

The transmission electron microscopy is an imaging technique which is used to collect information like imaging, diffraction pattern, and elemental composition a thin specimen. Unlike conventional light microscopy where one uses the photons to capture the image, in transmission electron microscope (TEM) one uses the highly energetic electron beam (energy 200 kV) which penetrates the samples (thickness less than 200 nm) and after passing through a set of condenser lenses and aperture, the intensity of the transmitted beam is recorded via CCD camera [13]. Due to the thickness variation of the sample at different regime, as the thicker regime of the sample is more occlude as compared to the thinner regime, the difference in the intensity of transmitted beam leads

to a difference in contrast which helps in generating the micrographs. In general, the electrons that are scattered elastically and in elastically on interaction with the samples result in TEM imaging. The TEM can be used for both imaging and diffraction technique, unlike SEM where one can use it for only imaging technique [14].

We have used TEM to get the selected area diffraction pattern (SAED) to check the elemental homogeneity of the samples and to check the lattice spacing of the as-grown nanoparticles of nickelates. To check the elemental homogeneity of the specimen we have used the energy-filtered transmission electron microscopy (EFTEM). In Figure 2.6, we show the mapped elemental composition and SAED pattern for $Nd_{0.7}La_{0.3}NiO_3$ and $NdNiO_3$ nanoparticles.

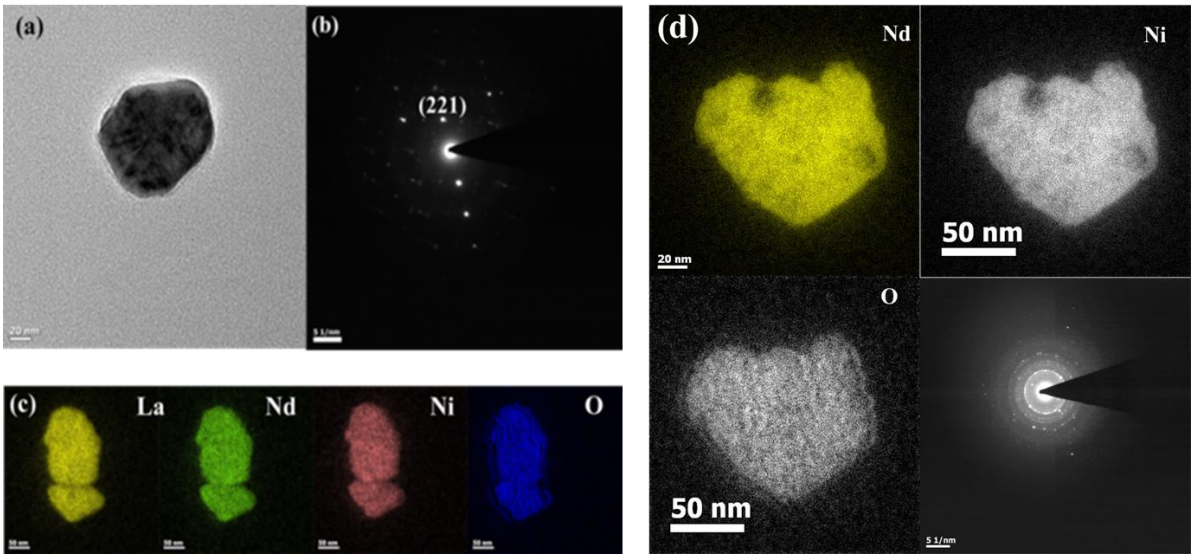

Figure 2.6 (a) The TEM image and (b) SAED pattern of $Nd_{0.7}La_{0.3}NiO_3$ nanoparticles, (c) and (d) represent the EFTEM mapping of $Nd_{0.7}La_{0.3}NiO_3$ and $NdNiO_3$ nanoparticles. The EFTEM images show that samples are elemental homogeneous.

2.4.4 Atomic Force Microscope

The Atomic force microscope (AFM) is a type of scanning probe microscopy (SPM) in which information related to the topographical image and the surface characteristics (like grain size and roughness) can be explored down to the nanoscale range. The main component of an AFM consists of a cantilever, scanner, laser and a four-quadrant photodiode [15]. The tip attached to cantilever is generally made of silicon nitride and used for the surface imaging. When a tip comes close to the surface of the sample, both attractive and repulsive forces come into the picture due to the

interaction between the tip and the sample surface which results in a positive or negative bending of the cantilever, which is detected by the laser beam. The laser beam reflects back from the cantilever onto the four-quadrant photodiode detector. Using the position-sensitive photodiode, one can measure the bending of the cantilever very accurately. Hence during the XY scan, the bending of cantilever and samples height can be monitored which is eventually used for generating the AFM image. The advantage of AFM is to get the surface morphology of highly insulating samples along with the metallic ones, where the former is not possible in a Scanning-tunneling microscope.

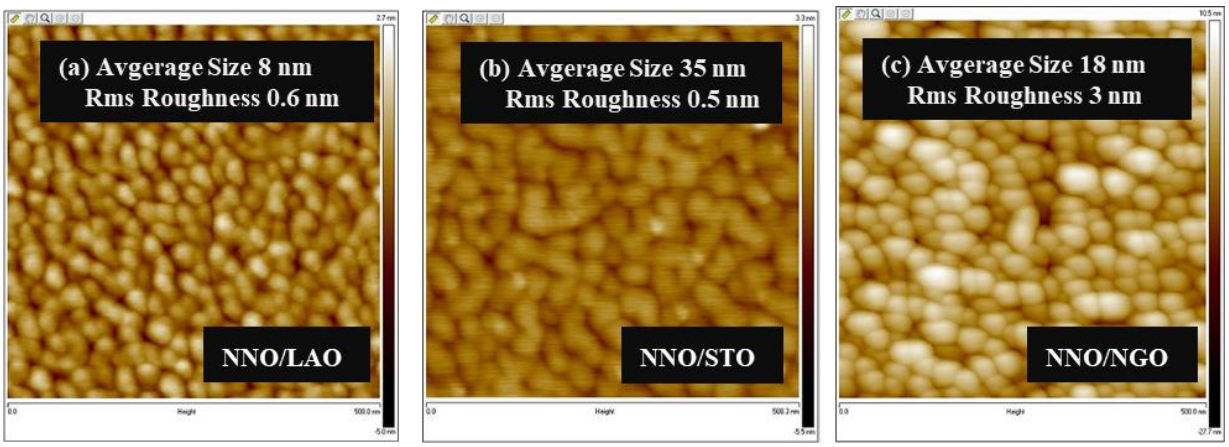

Figure 2.7 (a) The nearly 1µm × 1 µm AFM topographic image of $NdNiO_3$ film of 60 nm grown on LAO, STO and NGO single crystal substrates.

2.5 Measurement Techniques

2.5.1 Scanning Tunneling Microscope

The first Scanning tunneling microscope (STM) was developed by the Binning and Rohrer in 1981 at IBM laboratory. They incorporated the theoretical prediction of Fowler and Northeim into the real design [16]. The basic principle of an STM is tunneling of electrons through a potential barrier in an ultra-high vacuum. Classically this tunneling is forbidden but quantum-mechanically the dual nature of electrons allows them to penetrate a potential barrier (V) even if the energy of electrons (E) is less than the potential barrier (E < V) and thus there is always a finite probability of electrons tunneling even if E < V, which is forbidden according to classical mechanics.

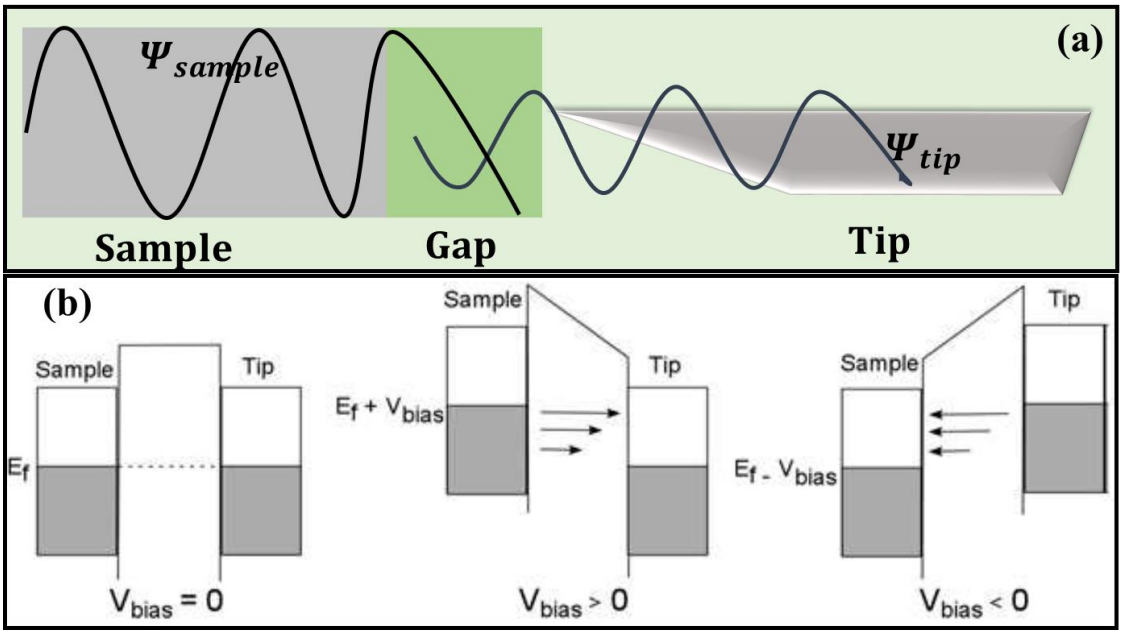

Figure 2.8 (a) The schematic of overlapping of samples and tip wavefunction through a potential barrier and (b) change in Fermi level; of the sample on application of different bias [Image b is taken from reference 17].

In a laboratory STM, for such tunneling to occur a sharp tip of Pt-Ir / W is brought in the close vicinity (sub-nanometre) of the samples. This configuration makes a metal-insulator-metal/semiconductor/insulator junction [18]. In the absence of applied bias, the probability of electrons to tunnel from the sample to tip or tip to sample is the same (As shown in Figure 2.8 (a)). As a result, the net tunneling current is zero. In the presence of applied voltage bias, the Fermi level (E_F) can be raised [17]. When V is applied on the sample with respect to the tip, the E_F of the sample can be raised to E_F + V. Thus, the electrons from the occupied state of the samples can tunnel into the unoccupied states of the tip [9, 16-18]. This results in a net tunneling current flow from the tip to sample. On applying a bias to the tip with respect to the sample, this results in a tunneling current flow from the sample to tip. The rise in E_F on the application of bias has been shown in Figure 2.8 (b). The tunneling current is directly related to the density of state of the sample and is given by:

$$I\,(z,V,W,T) = c\int_{-\infty}^{\infty} N_S\left(E+\frac{eV}{2}\right) N_t\left(E+\frac{eV}{2}\right)\tau(z,E,W)\left[f\left(E-\frac{eV}{2}\right)-f\left(E+\frac{ev}{2}\right)\right]dE \qquad (2.2)$$

Where *c* is a constant which depends on the tip-sample effective junction area, *z* represents the distance between tip and sample, W defines the mean work function of the sample and tip surface, *T* represents temperature, tunneling barrier penetration factor is defined by t, *Nt* (E), *Ns* (E) is the DOS of tip and sample respectively, and *f* (*E*) defines the Fermi function.

The STM/STS results presented in the thesis has been collected using a commercial STM UHV SPM 350 by RHK technology [19]. The system consists of the two chambers namely load lock and main chamber. The load lock chamber was attached to a turbopump with a base pressure of 10^{-8} mbar and the main chamber was attached to an ion pump with a base pressure of 10^{-10} mbar. Thus, a condition for ultra-high vacuum (UHV) is always maintained.

The measuring unit of our system consists of the following units:

1. R9 Controller: The backbone of the UHV STM. A fully integrated circuit, which provides control for the SPM. All feedback loops, lock-in amplifier, filters, signal generators are part of this unit.
2. Scan Head and Sample Holder: A unit for the tip to approach the samples on a beetle type sample holder. The three piezoelectric legs of the scan head with Z piezo sensitivity 1.5 nm/V and range ± 225 nm allows the tip to approach sample in a beetle motion.
3. Thermocouple: The Ni-Al K type thermocouple allows us to measure the sample temperature correctly.
4. W-Filament: It has been used as a heater while performing temperature-dependent STS.
5. Lock-in amplifier: To detect the dI_t and I_t as a function of bias (V).
6. IVP Preamplifier: A preamplifier with 10^8 Gain (10nA/V) was used to provide a differential signal from tip and sample to R9 controller.
7. Vibration Isolation: Most important part for any vibration-sensitive measurement. This has been taken care by a bench floating on three nitrogen gas legs.

Depending on the requirements, the STS was performed by measuring the local tunneling conductance $g(=\frac{dI}{dV})$. The STS provides the information on spatial dependence of the DOS at the Fermi level (E_F). During STS, the temperature was kept stable during data scan and no drift in the temperature was observed. The $\frac{dI}{dV}$ was measured in a modulation mode with a small ac bias. The

data was taken with a constant direct current (dc) bias (for keeping a fixed height of the tip above the film), and a small a.c modulation voltage (much less than the dc bias) that has been used to measure the differential tunneling conductance $\frac{dI}{dV}$. Taking a raster scan in the presence of an ac modulation allows one to record the topography as well as spectroscopy data together. The noise floor of the measuring system was less than 10 pA/$\sqrt{Hz}$ and the tunneling resistance was few Gigaohms. The local tunneling conductance map is a contour plot of $g = \frac{dI}{dV}$ taken at a fixed dc bias V. In Figure 2.9 we show the schematic of the STM unit to detect the tunneling current and the electronics associated with it.

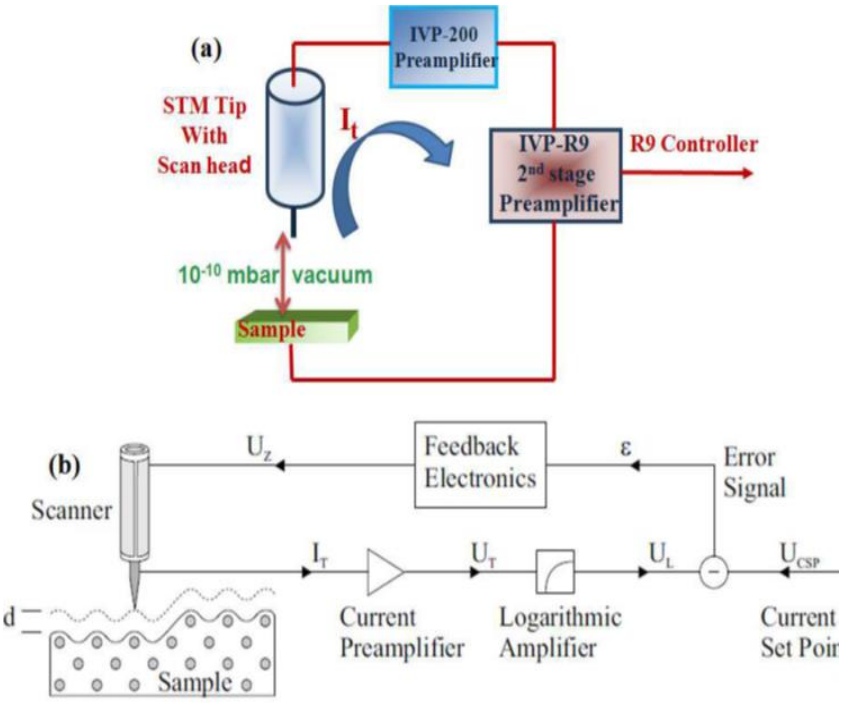

Figure 2.9 (a) The Schematic of detecting tunneling current through the IVP 200 preamplifier and (b) The schematic of the electronic circuit in STM [Image is taken from reference 9 and 20].

It is a good practice to incorporate these parameters/facts for good spectroscopy data according to their technical specifications:

i. Optimization of bias modulation: If the output signal is very small, depending on the number of bits the digitally showed output may not be a correct value given by the hardware.

ii. Lock-in cut off frequency: While choosing the lock-in bias frequency (f) one has to be sure that it falls under the bandwidth of the preamplifier. For a given bias frequency (f) the filter cutoff frequency (F) can be set according to $F < \frac{f}{10\pi}$ and a $pre-$ sampling delay of $\frac{5}{2\pi F}$.

iii. Adjustment of the lock-in amplifier phase to remove the capacitive coupling between the sample and tip.

In Figure 2.10 (a) and (b), we show the schematic of experimental set up used for I-V measurement using 100 Mohm tunneling simulator and an STS data used as a calibration to make sure that there is no offset present due to the electronics and broadband noise. We have chosen a narrow range ($\pm$ 50 mV) of bias to check whether any offset is present across a test sample or not. To rectify the offset we have adjusted the gain of preamp and took an I-V measurement across a standard tunneling simulator of resistance 100 Mohm. This was used as a calibration before all STS data taken on the samples.

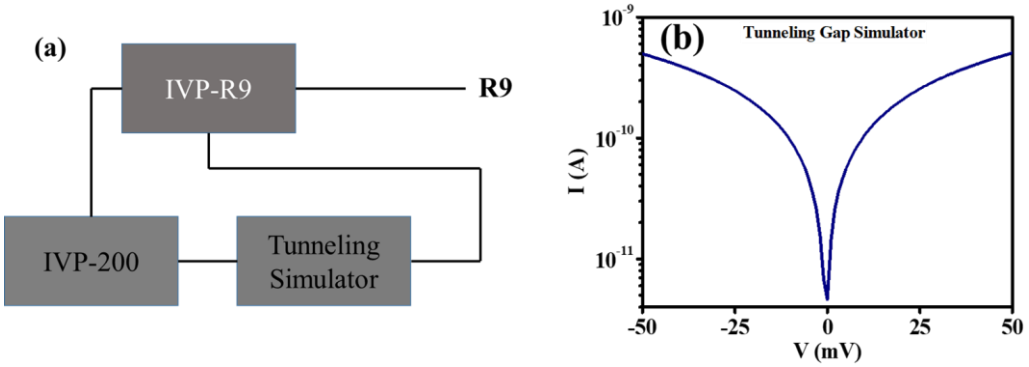

Figure 2.10 (a) The experimental set up for I-V measurement and (b) The I-V data for 100 Mohm tunneling simulator which shows the absence of offset in the data.

2.5.2 Impedance Spectroscopy

An LCR meter is generally used for the measurement of complex impedance in a frequency range from 10 Hz to 100 MHz. The LCR meter generally uses different methods namely Bridge method, Network analysis method, etc. to measure the impedance, phase angle, resistance, capacitor, etc. Depending on applications, a different type of bridge circuit elements which may be a combination of an inductor, capacitor, resistor, etc. are used in different instruments. Amongst all the methods, the most familiar bridge method is auto-balancing bridge method which works in a wide frequency

range from 20 Hz to 100 MHz. A typical LCR meter measures the current across the source under test, voltage and the phase angle between current and voltage. All other parameters can then be calculated. An LCR meter generally has four terminals low current, high current, low potential, and high potential. Low current /High current is for current measurement and low potential/high potential for voltage measurement [21]. In our experiments, we have used commercial Hioki 3532-50 LCR meter, which works from 42 Hz to 5 MHz.

2.5.3 Low temperature electrical and magnetic transport

For the electrical measurements up to liquid nitrogen (LN_2) temperature, we have used a homemade cryostat which had four wires connected (high-quality coaxial cables) to the base where the Pt-100 was fixed with a GE varnish and used as a sensor. A manganin wire was used as a heater. The jacket of cryostat was pumped down to 10^{-3} mbar pressure before inserting it to the LN_2 bath. The electrical and magnetotransport measurements below LN_2 temperature were performed in a cryogen-free and cryogen based cryocooler. For the cryogen-free cryocooler, we have used the Gifford McMahon cycle based cryostat from cryogenics and Pulsed tube cycle based cryocooler. For the cryogen-based cryostat, we have used He-3 insert from the oxford instruments. Further, the set up was equipped with a superconducting magnet that can produce a magnetic field of 16 Tesla. The method of producing a cold from these cryocooler has given in the standard books. However, the main parts of a cryocooler are the compressor, regenerator, and displacer [22-25]. The basic difference between a pulsed tube cryocooler (PTC) and a GM cryocooler (GMC) is summarized below:

- The displacer in a PTC is replaced by a pulse tube.
- The PTC is more expensive than GMC.
- The performance of a PTC is orientation dependence while it is not orientation dependence on GMC.

We have used the following systems for the low-temperature measurements.

Temperature Range	**System Used**
20 mK [25]	Dilution Refrigerator (Oxford Triton 400 XL)
300 mK [24]	Helium-3 Refrigerator (Oxford Heliox VT)
3 K [23]	PTC 405 (Cryomech)
10 K [22,26]	GMC (Coldedge, and Cryogenics)
80 K	Homemade LN_2 cryostat

Before the electrical measurements, we have calibrated the cryostats with a standard Pt-100 sensor. The measurement was done in a pseudo-four-probe configuration. In Figure 2.11 (b) we show the RT data for Pt-100 RTD sensor and which is known to follow a Bloch-Gruneisen relation. The obtained Debye temperature of 240.004 K matches fairly with the Debye temperature reported for the platinum. The RT measurements of the samples presented in this thesis were done in a four-probe configuration with the use of a Keithley source meter 2400/2410. In some of the cases where the sample resistance was quite low, we have used the lock-in amplifier (LIA) based ac technique. In Figure 2.11 (a) we show the schematic of the measurement setup in a four-probe configuration.

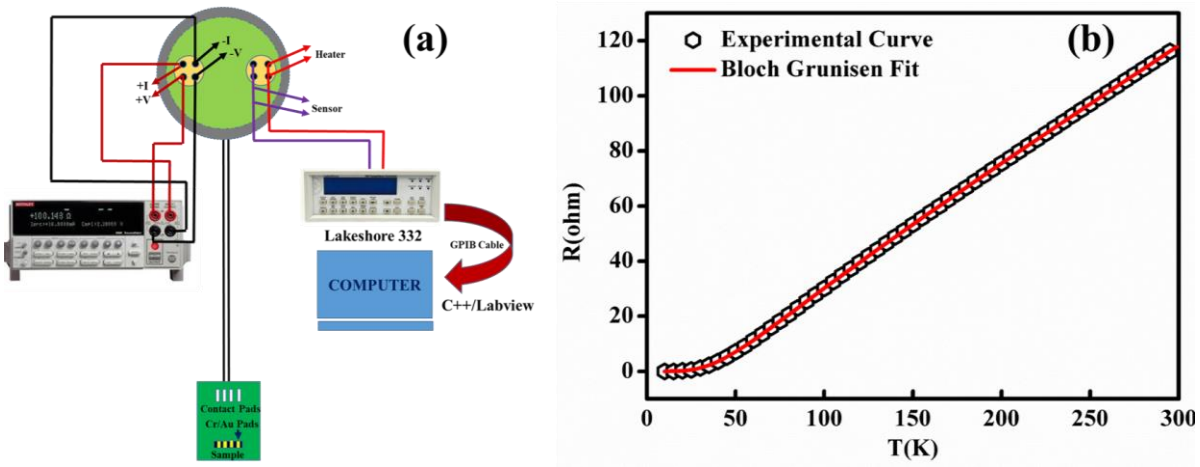

Figure 2.11 (a) The experimental schematic of four-probe measurement and the low-temperature cryostat and (b) The experimental RT data of standard Pt 100 sensor. The data were fitted with Bloch Gruneisen relation for resistivity and the Debye temperature extracted from the fit was 240.004 K. The Debye temperature matches excellently with reported value for Pt in literature.

2.5.4 Low-temperature 1/f noise spectroscopy

In this thesis, we have used 1/f noise spectroscopy in a four-probe configuration to probe the dynamic nature of phase co-existence and to probe the disorder induced by the ion irradiation. In Figure 2.12 we show the schematic of the noise measurement setup. In the noise measurement one bias the sample with a constant current $I_0 sin 2\pi f_0$ where f_0 is the frequency of LIA [27-30]. The value of series resistance (R_s) is chosen in such a way that $R_s >> r_s$, where r_s is the sample resistance. In this way, the samples voltage is amplified through a preamplifier and fed into the lock-in inputs and demodulated by the lock-in amplifier. After the demodulation, the signal is fed into the analog

to digital converter (ADC) card where the signal is processed via anti-aliasing, decimation, and digital signal processing [30].

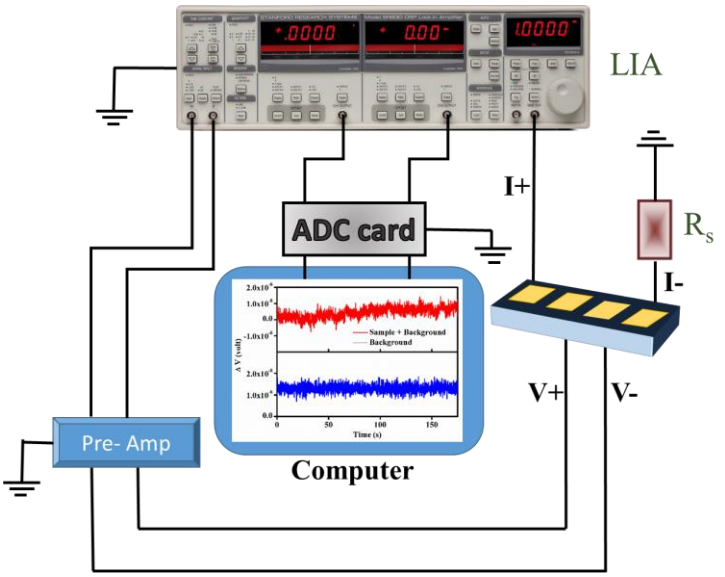

Figure 2.12 (a) The schematic of experimental four-probe 1/f noise measurement. Inset of the computer shows the time series of sample and background.

In the noise experiment, we record voltage fluctuations $\Delta V(t)$ as a function of the time. From the $\Delta V(t)$ one can get a power spectral density (PSD) using Fourier transformation, which is given as follows:

$$S_v(f) = \lim_{T\to\infty} \frac{1}{2T}\left[\int_{-T}^{T} \Delta V(t)\exp(-2\pi i f t)dt\right]^2 \quad (2.3)$$

In actual practice, the PSD was calculated from the method of average periodogram developed by the Welch [31]. As the PSD at the lock-in output is given as:

$$S_v(f,\delta) = G_0^2[S_v^0(f-f_0) + I_0^2(f-f_0)S_R(f)\cos^2\delta] \quad (2.4)$$

where $S_v^0(f)$ is the PSD due to background fluctuations, $S_R(f)$, δ , G_0 is the resistance fluctuation of the samples, phase of the LIA reference with respect to the measured voltage and the product of gain of LIA and Preamplifier [30]. Thus for δ = 0, we measure both the samples as well as background noise. While for δ = 90, we measure only background noise and the samples noise can be extracted after subtracting the background noise from the sum of the total noise (sample plus

background noise). This is one of the major advantages for the LIA based ac technique to measure the noise as one can measure the sample as well as background noise together.

In Figure 2.13 (a), we show the PSD of a low noise carbon resistance of 90 ohms at room temperature. As can be seen the PSD for sample goes as $\frac{1}{f^{\alpha}}$. When $\alpha = 0.8 - 1.2$ it is called 1/f noise. The background matches the Nyquist noise $4K_BTR$, where K_B, T, and R represent Boltzmann constant, temperature and resistance of the sample. Figure 2.13 (b) shows that the PSD is proportional to the V^2.

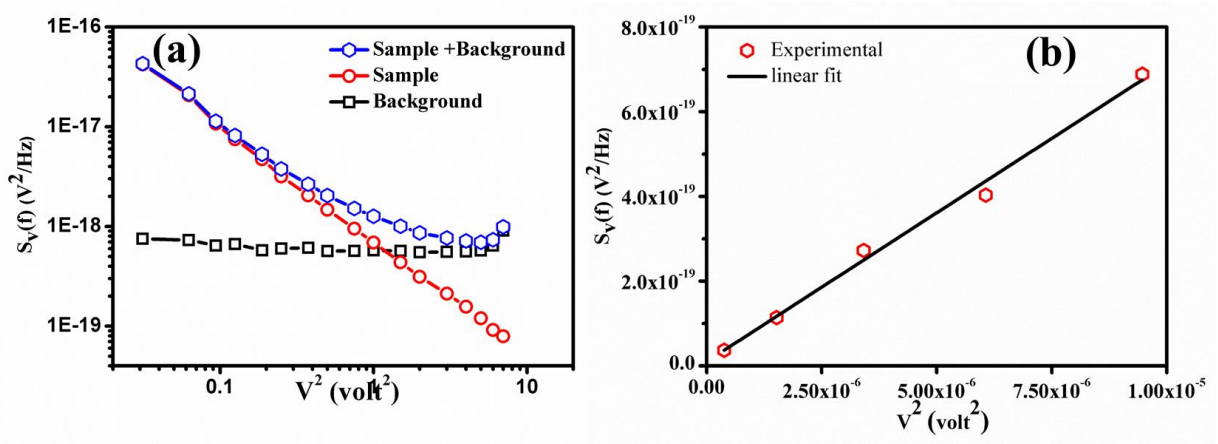

Figure 2.13 (a) The PSD of sample plus background, sample, and background noise for a low noise carbon resistance of 90 ohms at room temperature and (b) The PSD shows a V^2 dependence.

According to the central limit theorem, if the fluctuations are independent in any system, their statistics will be Gaussian. However, if there is a correlation in the fluctuation due to the physical reasons the statistics will be non-Gaussian. Often the correlation between the fluctuations can be established through higher-order statistics. To establish that we have chosen the second spectra method. The second spectra define as the Fourier transform of four-point correlation in a frequency band. Our method follows the one proposed by Seidler and coworkers [32]. The Gaussian/non-Gaussian behavior was established using the normalized second spectrum which is given as:

$$S^2(f_2) = \frac{\int_0^{\infty} <\Delta V^{(2)}(t)\Delta V^{(2)}(t+\tau)>\cos(2\pi f_2 \tau)d\tau}{[\int_{f_L}^{f_H} S_V(f_1)df_1]^2} \qquad (2.5)$$

where f_1 and f_2 represent frequencies associated with the first and second spectrum respectively. The numerator represents the second spectra and the denominator represents the first spectra.

Another way to establish the Gaussian and non-Gaussian behavior is through the probability distribution function [33]. The probability distribution function (PDF) for a Gaussian distribution of fluctuations ΔV which is centered at zero means follows the relation:

$$P(|\Delta V|) = \frac{1}{\sqrt{2\pi\sigma}} \exp\left(\frac{-(|V|)^2}{\sigma}\right) \tag{2.6}$$

For a Gaussian distribution, plotting $\ln P(|\Delta V|)$ as a function of $(|V|)^2$ should give a linear plot and any deviation from the linearity would signify the non-Gaussianity.

The second spectra and PDF becomes an important tool to probe any transition where the correlated fluctuations play a significant part in the system. For a system which shows MIT, the phase coexisting region can be easily identified from the magnitude of second spectra. The large change in the second spectrum close to T_{MI} can be better appreciated as a result of phase co-existence. Similarly, near the MIT the correlated fluctuations end up with a non-Gaussianity tail in the plot of probability distribution function as a function of mean square fluctuations. In Figure 2.14 (a) and (b), we have shown how second spectra and PDF develops a change near MIT.

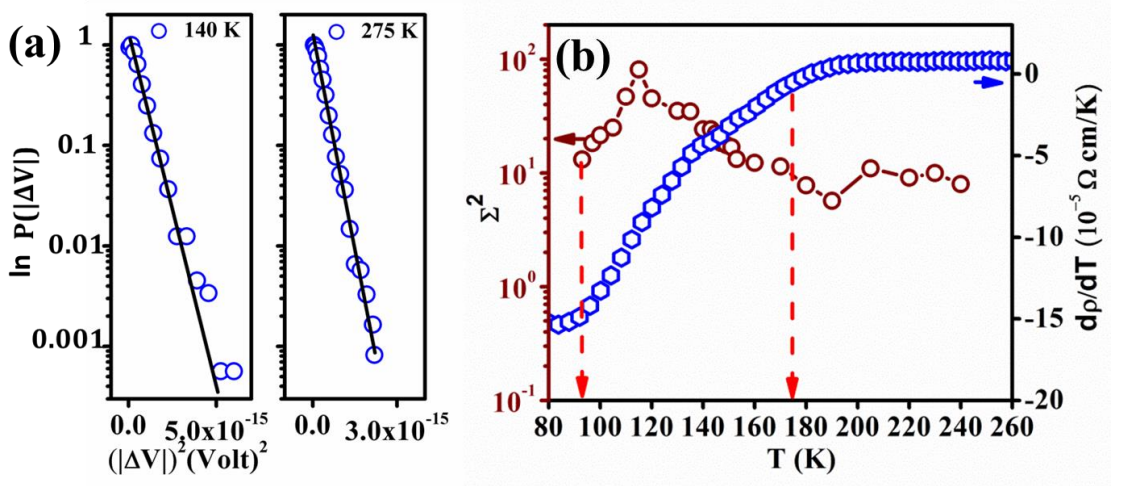

Figure 2.14 (a) The PDF and (b) integrated second spectra of $NdNiO_3$ film grown on $LaAlO_3$ single crystal substrate.

Bibliography for Chapter 2

1. G. Catalan, Phase Trans. 81, 729, (2008).
2. R. Jaramillo, F. Schoofs, S. D. Ha, and S. Ramanathan, J. Mater. Chem. C**,** 1, 2455-2462 (2013).
3. Tapati Sarkar, Tuning of ground state and phase transition in complex oxide nanomaterials, Ph.D. thesis, University of Calcutta, India (2018).
4. T. Venkatesan, X. D. Wu, A. Inam, and J. B. Wachtman, Appl. Phys. Lett. 52, 1193 (l988).
5. https://en.wikipedia.org/wiki/Pulsed_laser_deposition
6. https://www.coherent.com/lasers/laser/compex
7. https://en.wikipedia.org/wiki/Reflection_high-energy_electron_diffraction
8. http://pruffle.mit.edu/atomiccontrol/education/xray/xray_diff.php
9. Rajib Nath, Investigation of novel electrical and magnetic properties of perovskite oxides, Ph.D. thesis, University of Calcutta, India (2018).
10. https://www.malvernpanalytical.com/en/products/product-range/xpert3-range
11. C. Brechignac, P. Houdy, and M. Lahmani, A textbook of Nanomaterials and Nanochemistry
12. Joseph Goldstein, Scanning Electron Microscopy and X-Ray Microanalysis
13. Electron Microscopy: The Basics written by Bettina Voutou, Aristotle University of Thessaloniki, Greece and Eleni-Chrysanthi Stefanski
14. Electron Microscopy Fundamentals by Teri W. Odom.
15. https://www.nanosurf.com/en/
16. G. Binning and H. Rohrer, Surface Science 126, 236 (1983).
17. Scanning Tunnelling Microscopy, laboratory program, Nue Unique (2009).
18. E. L. Wolf, Principles of Electron Tunnelling Spectroscopy, Oxford University Press, Oxford, 1989.
19. www.rhktech.com.
20. Sohini Kar, Ph.D. thesis submitted to IISc Bangalore.
21. https://www.hioki.com/login.jsp?url=%2Fen%2Fmypage%2F%3F
22. Cryogenic 1.5K VTI system manual.
23. https://www.cryomech.com/cryocoolers/
24. https://nanoscience.oxinst.com/products/helium3-refrigerators/helioxvl

25. https://nanoscience.oxinst.com/products/cryofree-dilution-refrigerators/tritonxl
26. https://coldedgetech.com/custom-cryostats/
27. A. Ghosh, Ph.D. Thesis, Indian Institute of Science, Bangalore, India (2000).
28. Sh. Kogan, "Electronic noise and fluctuations in solids"
29. J. H. Scoffield, Rev. Sci. Instr. 63, 4327 (1992)
30. A. Ghosh, S. Kar, Aveek Bid, and A. K. Raychaudhuri, arXiv: Cond-Mat./0402130 v1, 4th Feb (2004).
31. P. D. Welch Modern Spectral Analysis, Edited by D.G.Childers (IEEE press, John Wiley and Sons, New York, 1978) page 17.G. T. Seidler and S. A. Solin, Phys. Rev. B 53, 9753 (1996).
32. G. T. Seidler and S. A. Solin, Phys. Rev. B 53, 9753 (1996).
33. A. Bid, "Resistance Fluctuation and Instability in Metal Nanowire", Ph.D. Thesis (2006), Indian Institute of Science, Bangalore.

Chapter 3 Phase co-existence near the metal insulator transition

In this chapter, we discuss the observation of phase co-existence near the metal-insulator transition (MIT) in a film of $NdNiO_3$ grown on single crystalline substrate $LaAlO_3$. The three techniques namely scanning tunneling spectroscopy (STS), 1/f noise spectroscopy, and impedance spectroscopy (IS) were used to probe the observation. The spatially resolved STS show the two co-existing phases have different types of density of states (DOS) at the Fermi level (E_F). One phase showed a depleted DOS close to E_F with a small yet finite correlation gap while the other co-existing phase showed a metal like DOS that has no depletion. The existence of the phase separation leads to a jump in the resistance fluctuation (as seen through 1/f noise spectroscopy) at the transition and importantly the fluctuation becomes non-Gaussian for a weak phase separation even in the metallic phase. We discuss a certain scenario that leads to such a phase separation in the general context of strongly correlated oxides. This observation of the phase separation may be generic in nature and may be present in different correlated electron system which undergoes MIT.

3.1 Introduction

The phase co-existence and the depletion of the density of states (DOS) at the Fermi level (E_F) in a correlated material have been observed experimentally for many correlated oxides [1-2]. There is clear evidence of depleted DOS probed by barrier type tunneling spectroscopy in materials like manganites and $NdNiO_3$ [3-4]. Theoretical predictions also suggest that in correlated metals the DOS at E_F may show depletion [5]. In $NdNiO_3$ a relatively recent experiment reported depletion of DOS even in the metallic state ($T > T_{MI}$ (metal-insulator transition temperature)) before the insulating state sets in with a small but clear hard gap [4]. Even in metallic $LaNiO_3$, there is evidence for depletion in DOS when the film is disordered primarily arising from electron-electron interactions [6]. In the context of $LaNiO_3$, with Mn substitution at Ni site, it has been shown that a hard gap although small (~10 meV) can open up at the metal-insulator transition (MIT) [7]. Thus there is ample evidence that there can be depletion of DOS in such correlated oxides even in the metallic state and as the transition to the insulating state is approached a hard gap may open up in the DOS.

The formation of nanoscopic insulating domains in $NdNiO_3$ film grown on $NdGaO_3$ has been observed using photoemission electron microscopy very recently. However, the insulating domain starts growing just below T_{MI} [8]. Catalan et. al described the transport properties of $NdNiO_3$ film using a percolation approach [9]. While writing this thesis, we came across two publications by Daniele Preziosi et. al and K. W. Post et. al. [10-11]. Daniele and coworkers have mapped the phase co-existence using a conducting Atomic force microscope (AFM) and the asymmetric nature of the I-V curve was related to the presence of the Schottky barrier between tip and sample. Their observation shows that some of the high conductance phases survive even above the transition temperature [10]. K. W. Post and coworkers show that the MIT has aspects of both Mott transition and Anderson transition so that one has mixed first-order and second-order transitions with co-existence of different electronic phases [11]. In general, no comments have been made on the depletion of DOS in the system. However, one can not really compare the results obtained from optical conductivity experiments and scanning tunneling spectroscopy experiments. [7, 11-15].

In this chapter, we show an observation, that in films of $NdNiO_3$ (NNO) grown on $LaAlO_3$ (LAO) substrate (hereafter NNO/LAO), there is co-existence of two phases and it was mapped using

spatially resolved Scanning tunneling spectroscopy (STS) and supported by probes like 1/f noise spectroscopy and Impedance spectroscopy (IS). We find the phase co-existence even in the metallic phase of NNO ($T > T_{MI}$), as the insulating state is approached on cooling ($T \rightarrow T_{MI}$), the DOS at the E_F is not spatially homogeneous and shows depletion in pockets. Broadly there are two phases that co-exist in the film: a normal metallic phase, which has no depletion in DOS, which co-exists with another phase which has depletion in DOS. This is seen in the metallic phase with $T > T_{MI}$. This observation is enabled by the spatial resolution of STS which is not possible to obtain in barrier type tunneling experiments as done in the past. The co-existing phases, in essence, make the material 'inhomogeneous' on a nanoscopic scale (few tens of nm) where the two co-existing phases evolve as the temperature is lowered and the MIT is approached.

We also show that this inhomogeneous behavior observed through co-existence of two phases in STS is also observed in 1/f noise spectroscopy. The 1/f noise data shows that at the transition region the noise magnitude is severely enhanced with a shift of spectral weight to lower frequency and there is also an appearance of a strong non-Gaussian component. We further strengthen this claim by observation of a peak in the dielectric constant of the film at T_{MI} that establishes the existence of internal boundaries between phases with different conductivities. The three observations together present a new view of MIT in the nickelates that have not been observed before.

In this work, the films used are thick enough to be strain relaxed. However, they have a residual compressive strain that lowers the T_{MI} and stabilizes the metallic phase with a positive temperature coefficient of resistance. We choose NNO/LAO for our experiment, because, the metallic state in NNO/LAO is stabilized strongly by the compressive strain and recent optical conductivity experiments on such films have shown that the Drude peak actually gets strengthened on cooling [13]. It is thus fascinating that even in such a system we observe the appearance of a phase with a depleted DOS. The present investigation adds a new dimension to this and shows that the opening up of depletion in DOS at E_F has a spatial dependence that can co-exist with a normal conducting phase which follows parabolic dI/dV as expected for a metal-insulator-metal junction.
To summarize this, In this chapter our results and discussion address to the following points:

- ✓ Observation of phase co-existence of high-temperature metallic phase and low-temperature insulating phase near the MIT.
- ✓ The two phases have a spatially dependent DOS. One phase shows a normal DOS at E_F while other phase shows a depletion in DOS at E_F.
- ✓ The observed phase co-existence is dynamic in nature.
- ✓ We discuss certain scenarios which may be responsible for this phase co-existence.

3.2 Strain state of the $NdNiO_3$ film grown on $LaAlO_3$ single crystal

In this section, we will discuss the strain state of the NNO film grown on LAO single crystal. The XRD was used to calculate the substrate-induced strain (as discussed in chapter 2). The XRD pattern was recorded by varying the angle between the detector and incoming x-ray. Figure 3 (a) shows the $\omega - \theta$ XRD scan which reveals that the film is strongly textured in the $(100)_{pc}$ or $(110)_o$ direction and the calculated substrate-induced strain ($\varepsilon = \frac{d_{bulk} - d_{film}}{d_{bulk}}$) was near -0.5 %. (The strain calculated as a shift of the lattice constant from the bulk value).

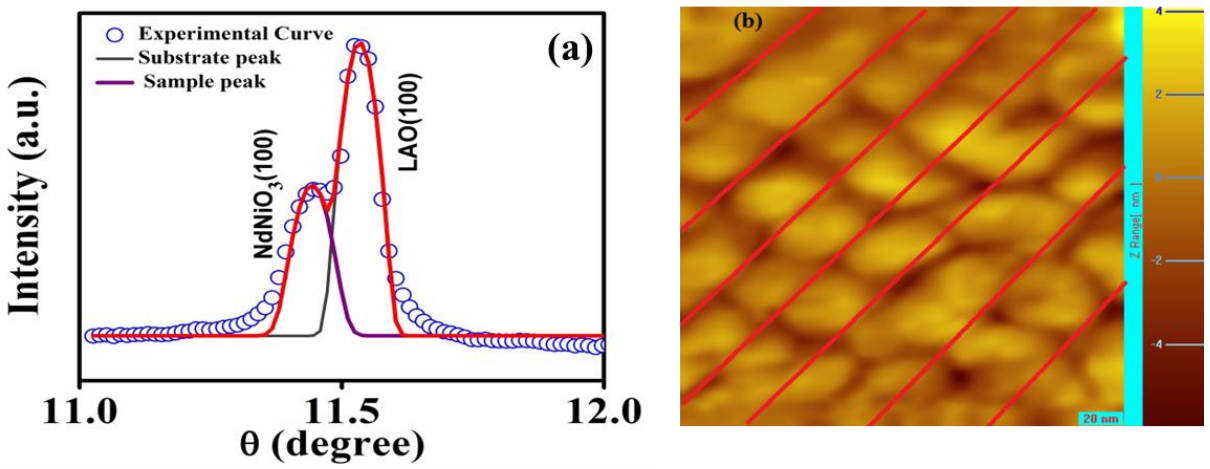

Figure 3 (a) XRD pattern shows the film and substrates reflection and (b) STM topography image of the film, the red lines are guided to the eye which shows the underlying terrace pattern in which the film was grown.

The negative sign shows that in-plane strain is compressive in nature and subscript pc and o represents the pseudocubic and orthorhombic notation respectively. From the STM topography image in Figure 3(b), one can see that the film is strain relaxed and broken into coherent regions

(grains) ~ 40 nm in size. The grains are oblate with the long axis aligned to the underlying substrate terrace axis. The grown film has a thickness of nearly 60 nm.

3.3 Resistivity as a function of temperature

In this section, we discuss the resistivity measurement of the NNO film grown LAO substrate. In order to perform the electrical measurement, Cr/Au contact pads were made on the films by thermal evaporation. The resistivity measurement was done in a collinear four-probe geometry down to 30 K in a cryogen-free closed-cycle refrigerator. Other experimental details and schematic of resistivity measurements are given in chapter 2 of the thesis. The distance between the voltage pads was 200 µm. Resistivity (ρ) data (Figure 3.1(a)) show the transition from the metallic state to an insulating state. The compressive strain in the film stabilizes the metallic state, and the T_{MI} is shifted to a lower temperature (Figure 3.1(b) shows the derivative $\frac{d\rho}{dT}$ vs T). The changeover of the sign of the derivative curve where $\frac{d\rho}{dT} = 0$ is taken as the T_{MI}. For the cooling curve, the T_{MI} is ~110 K, and for the heating curve, it is around ~148 K. The ramp rate for the temperature sweep was adjusted to 1 K/minute.

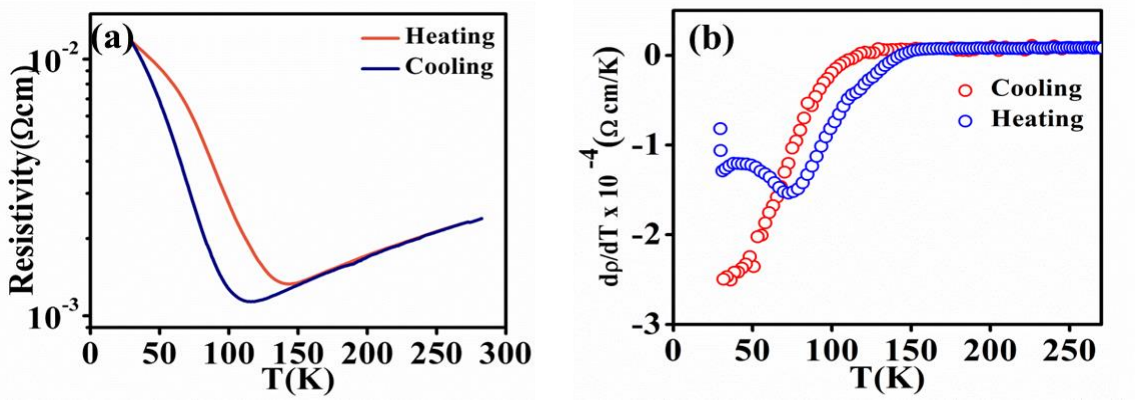

Figure 3.1 (a) Resistivity of $NdNiO_3$ film as a function of temperature during heating and cooling cycle and (b) The derivative of resistivity as a function of temperature for both heating and cooling cycle.

In the metallic state, $\rho \approx$ 2.5 mΩ-cm at room temperature (RT), and the temperature coefficient of resistivity (TCR) $\equiv \frac{d\rho}{\rho dT}$ ~ 5x10^{-3}/K. In metallic $LaNiO_3$ film typically the ρ at RT is somewhat

lower (0.5-0.6 mΩ-cm) with somewhat higher TCR of ~ 8-10x10^{-3}/K. The value of ρ, however, does depend on the substrate, thickness, and the oxygen pressure at growth. The crucial point here is to note that for $T > T_{MI}$, the TCR is strongly positive and the resistivity is in the range of maximum metallic resistivity as proposed by Mott [1, 16, 18]. The hysteresis in the resistivity graph can be attributed due to the first-order nature of the phase transition. If this is the scenario we can expect co-existence of high-temperature metallic phase and low-temperature insulating phase in the transition region. In the next section, we show the observation of spatial phase separation near MIT.

3.4 Spatial phase separation and observation of co-existing phases

To probe the spatial phase separation near the MIT we have used a UHV Scanning Tunneling Microscope (STM). The STS provides the information on spatial dependence of the DOS at the Fermi level (E_F) as discussed in chapter 2. The data were taken at 256 points (16 × 16) over a scan area of 200 × 200 nm. At each point, the data were taken 10 times and then averaged. The tunneling conductance was measured in a modulation mode with a small ac bias. The data were taken with a constant direct current (dc) bias (for keeping a fixed height of the tip above the film), and a small a.c modulation voltage (<< the dc bias) that has been used to measure the differential tunneling conductance($= \frac{dI}{dV}$). The local tunneling conductance map is a contour plot of $g = \frac{dI}{dV}$ taken at a fixed dc bias V. The dc bias thus defines the electron energy (E = eV).

Figure 3.2 (a) and (b) shows the local conductance map of NNO film grown on LAO substrate observed for a bias voltage of 0.1 V. The data are shown at two temperatures. One data is close to room temperature (290 K) where $T >> T_{MI}$ (Figure 3.2 (a)). The map is shown as a normalized tunneling conductance ($\frac{g}{g_{rms}}$) , where g_{rms} is defined as the root mean square (rms) value of g taken by a spatial average of the tunneling conductance's for a given bias V over the 256 points. This method allows us to quantify the extent of spatial inhomogeneity that arises due to the spatial dependence of DOS. At 290 K for V= 0.1 V, g_{rms} = 1.36x10^{-10} A/V. As shown in Figure 3.2 (a), at 290 K the tunneling conductance is more or less uniform where the local value of g is within 0.8 to 1.2 of g_{rms}, although there are small local patches (dark blue) where the value of g is noticeably lower ($< 0.5 g_{rms}$) and even as small as $0.3 g_{rms}$. The isolated pockets of such low g

have a length scale of a few tens of nanometers. The length scale over which conductance g is uniform are relatively large and they extend over a few tens of nanometer length scales. This inhomogeneity can be called as weak phase separation.

The inhomogeneity as measured by the spatial variation of $\frac{g}{g_{rms}}$ grows as the temperature is lowered, and closer to the transition region (T=130 K; Figure. 3.2 (b)), the sample is completely inhomogeneous and mostly consists of regions of rather low g (i.e. regions with depleted DOS) i.e. lower than $0.3g_{rms}$. At this temperature g_{rms} itself is low (~ 3.95×10^{-11} A/V). Due to the positive TCR, the ρ at 130 K is nearly 2 times lower than that at RT. However, the average tunneling conductance is lower than a factor of more than 3. Interestingly, at this temperature there are small pockets where the local tunneling conductance is relatively high, and $\frac{g}{g_{rms}}$ is >> 1. These pockets are tens of nanometer in size and are separated by regions of rather low tunneling conductance. These regions of high tunneling conductance are responsible for carrying the bulk of the conduction current, and we will see below that they are the reason for large resistance fluctuations that are non-Gaussian in nature. This co-existence of isolated metallic (high-conductance) regions separated by regions of much less conductivity also leads to the peaking of the capacitance at T_{MI}, as we will see in the impedance spectroscopy section.

The co-existence of two phases with widely different tunneling conductances (g) that have been seen in the conductance map as shown in Figure 3.2 (a) and (b), can be seen very clearly in the tunneling conductance $(g - V)$ curves taken at different locations. This allows us to quantify and clearly identify the regions with depleted g. We also studied the evolution of $g - V$ as a function of temperature with spatial resolution. This is shown in Figure 3.3 (a), where we show the temperature evolution of the $g - V$ curves at some of the marked locations (These regions are marked by respective symbols in Figure 3.2 (a) and 3.2 (b)). The red arrow marks the high tunneling conductance region and black arrow marks the low conducting region.

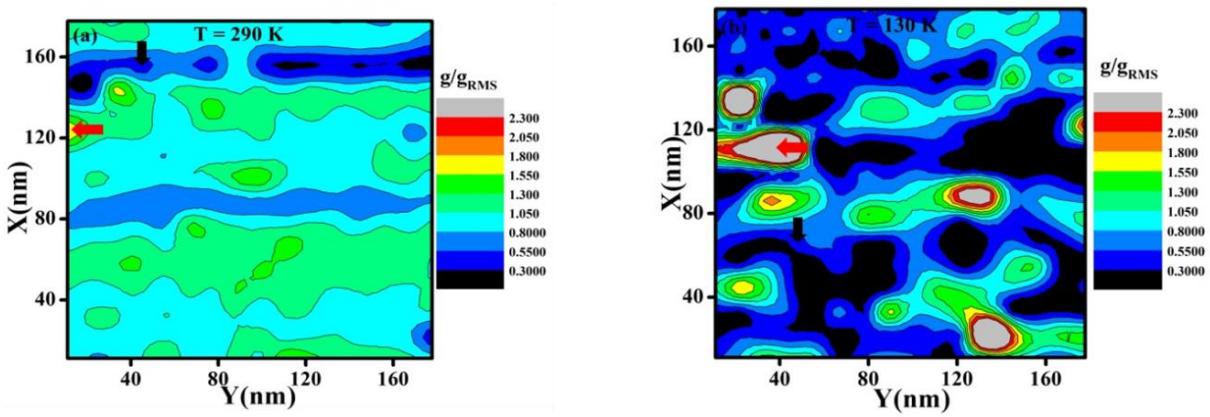

Figure 3.2 Local tunneling conductance map at (a) 290 K (Weak phase separation) and (b) 130 K (Strong phase separation). The data are plotted as normalized conductance $\frac{g}{g_{rms}}$.

The regions that show very high tunneling conductance show parabolic $g - V$ curves i.e., $g = \alpha + \beta V^2$ where α and β are related to DOS and mean tunneling barrier height. A parabolic $g - V$ curve is expected for a tunneling junction (with trapezoidal barrier formed by the vacuum barrier) with metallic electrodes and a nearly flat DOS, as in metal around E_F [19]. As shown in Figure 3.3 (a), $g - V$ curves in the region of high tunnel conductance remain nearly parabolic, even on cooling, although their volume fraction decrease on cooling as shown in Figure 3.2. In regions, where the tunneling conductance is low, the $g - V$ curve is nearly parabolic at high temperatures, but on cooling, there occurs a clear deviation from the parabolic behavior, as the DOS near the Fermi level gets depleted. This shows up as a depression in the $g - V$ curve near zero bias. To accentuate as well as quantify the deviation from the normal parabolic behavior, we plotted the normalized tunneling conductance g_n , defined as $g_n(V) = \frac{g(V)}{g_{fit}(V)}$, where $g_{fit}(V)$ is the fit to the tunnel conductance data for $|V| \leq 0.4$ to the parabolic relation. This is shown in Figure 3.3 (b). For the data in the bias region $|V| < 0.2$V where the depletion opens up, the normalized conductance curve shows a clear dip. We find that the dip in the tunneling curve in this region fits the relation

$$g_n(V) = g_0 \left[1 + \left({}^{|V|}/_{V^*}\right)^n\right], \qquad (3.1)$$

The energy scale $V^* = \frac{\Delta}{e}$ is the correlation gap [3, 17, 19]. We find that at T=130K at the transition region, the fit of the data to equation 3.1 gives the parameters n =0.85 and Δ=18 meV (The value

of Δ may grow at a lower temperature). The value of Δ near the MIT is fairly close to the value of correlation gap (15 meV) near the MIT measured by barrier tunneling [25] and the ratio $\frac{\Delta}{k_B T_{MI}} \approx$ 1.5. This is much smaller than the correlation gap seen in $LaNiO_3$ at low temperatures when it undergoes a disorder-induced MIT [4]. The exponent $n < 1$ but is close to it, which has been seen in many oxides close to the critical region of MIT. In many oxides, barrier tunneling data show that as the MIT region is approached, n grows from n = 0.5 (expected of a DOS with soft-gap and electron-electron interaction) closer to 1 at the critical region [3, 20, 21]. A value of n = 0.85 is thus consistent with the expectation from the MIT region. To rule out the fact that the dip in conductance is due to the depleted grain boundaries (if any), the data was taken on grain boundaries (GB) at 130 K and 290 K, however, a parabolic nature of differential conductance is consistent with the metallic $g - V$ as shown in Figure 3.3 (c).

The results depicted in Figure 3.2 and 3.3 very clearly show that there are two co-existing phases in the $NdNiO_3$ film that evolve when the temperature changes. A region with depleted DOS shows up for $T > T_{MI}$, which co-exists with a metallic phase. The depletion of DOS is enhanced as the transition region is approached from the metallic side on cooling. Likely, these are precursor regions where the insulating phase nucleates and eventually percolates through the whole sample at the MIT. Our results are in qualitative agreement with the barrier tunneling data reported before [4], which, however, is a spatial average over an extended region. The films used in this work are strain relaxed, and there are definite domains as seen by STM data. It will be tempting to attach the phase separation to the existence of these domains. It is quite likely that they act as nucleating centers for phase separation, but we note that there is an element of stochasticity in the formation of the phase separation. As a result, it is quite unlikely that the observed phase separation is completely determined by these domains. The size of the phase separated regions is much larger than the size of the domains.

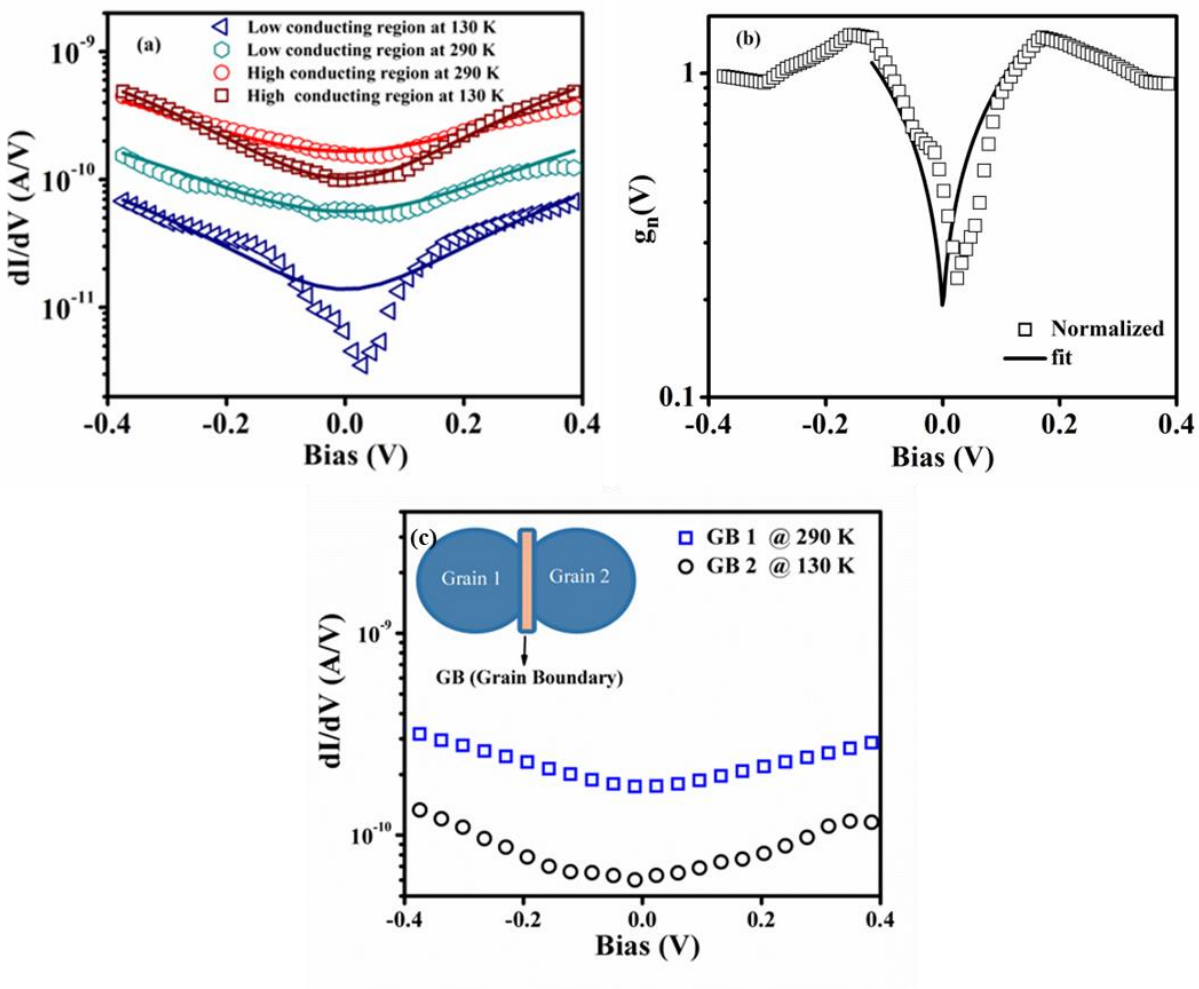

Figure 3.3 (a) The bias dependence of the local tunneling conductance $g = \frac{dI}{dV}$ taken at two locations marked by arrows in Figure 3.2, (b) The normalized tunneling conductance g_n as defined in text for the region with low conductivity at 130 K, the solid line shows the fit to equation 3 and, (c) The parabolic nature of tunneling conductance at the grain boundary (GB).

3.5 Dynamic nature of phase co-existence and $\frac{1}{f}$ noise spectroscopy

In the previous section, we have seen that STS results show that there is a phase co-existence near MIT that consist of regions that have different values of tunneling conductance. It is most likely that the phase with strongly depleted DOS has a low electrical conductance compared to the other phase that has no depletion in DOS and is the metallic part. The phase with depleted DOS may evolve at T << T_{MI} as the insulating phase. But above T_{MI} the depletion of DOS does not mean that the phase is insulating, and we refer to it as a "precursor insulator" (PI) phase.

The phase co-existence for $T > T_{MI}$ cannot be picked up easily by resistivity measurements alone because the metallic regions will carry the bulk of the current and will shunt the less conducting regions. A good probe of the electrical inhomogeneity that arises from such co-existing phases is 1/f noise spectroscopy, which is more sensitive than the resistivity experiment [22]. The observed phase co-existence can be static or dynamic depending on the time scale associated with them. In a dynamic phase co-existence, a conducting (insulating) region can convert to an insulating (conducting) region by crossing an activation barrier that stabilizes the phases. This will give rise to a finite time for the dynamics to change. If that happens, one will get a resistance fluctuation that can be picked-up using 1/f noise spectroscopy, if the time window of the noise spectroscopy is compatible with the time scale of the dynamics. The dynamic phase co-existence leading to large 1/f noise has been reported recently in $SmNiO_3$ as well as in VO_2 at the MIT [23, 24].

The resistance fluctuation (noise) was recorded as a time series of voltage fluctuation $\Delta V(t)$ in a current biased four-probe configuration as shown in Figure 3.4 (a). The measurement was done in a homemade set-up which uses an ac carrier frequency and the noise was measured in a bandwidth of 10 mHz to 10 Hz. The details of the noise measurements are given in chapter 2. At each temperature, the resistance fluctuation data were collected for ~ 16 minutes. The stability in the temperature at a given value during data acquisition was ±5 mK. This ensures that the fluctuation $\Delta V(t)$ data are free from thermal drift, Figure 3.4 (b) represents a flat background (Nyquist noise) at 220 K which itself suggest there is no thermal drift. Figure 3.4 (c) shows the spectral density of the voltage fluctuations across the sample and corresponding background noise, the spectral density of background noise is in good agreement with the theoretical value of $4k_BTR$ at 220 K. The k_B, T, and R represent Boltzmann constant, temperature, and resistance of the sample respectively. For R ~ 200 Ω, the power spectral density of Nyquist noise is of the order of 10^{-18}. This has been shown in Figure 3.4 (b).

We have calculated the normalized spectral power density ($\frac{S_v(f)}{V^2}$) for the whole temperature region from the recorded voltage fluctuation time-series $\Delta V(t)$. The data are shown in Figure. 3.5 (a) taken at different temperature. The spectral power density shows a $\frac{1}{f^\alpha}$ behavior. The exponent α shows a clear dependence on temperature and its value range from 1 to 1.4 and is shown in Figure 3.5 (b).

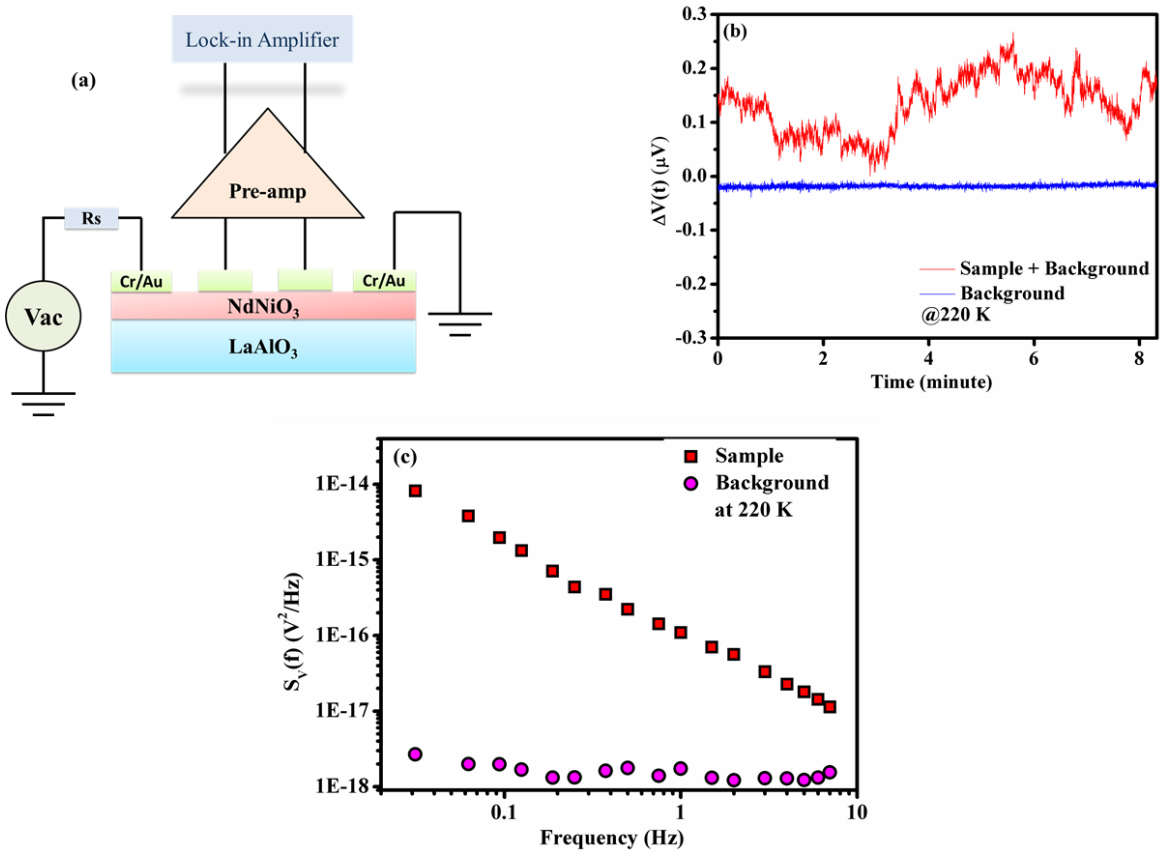

Figure 3.4 (a) Schematic of the noise measurement setup; R_s represents the standard series resistor, (b) The time series of the fluctuation across sample and background at 220 K and (c) The spectral density of the sample noise and background noise.

The temperature variation of the normalized mean square resistance fluctuation ($\frac{\delta R^2}{R^2}$) is shown in Figure 3.5(c) ($\frac{\delta R^2}{R^2} \equiv 1/V^2 \int_{f_{min}}^{f_{max}} S_V(f)df$, where, the f_{min} and f_{max} define the bandwidth of measurement). In the metallic state both the mean square fluctuation $\frac{\delta R^2}{R^2}$ decreases on cooling. The temperature variation of the fluctuation is similar to that seen in metallic $LaNiO_3$, as well as in conventional metals and alloys [25, 26]. This is primarily due to a decrease in defect activation that contributes to the 1/f noise on cooling. However, due to an even sharper rise of R as well, the $\frac{\delta R^2}{R^2}$ decreases below T_{MI}. The transition region marked in Figure 3.5(c) is expanded and shown in the inset. It can be seen that in the transition region there is a rise in $\frac{\delta R^2}{R^2}$ over the small temperature range of 130 K to 149 K. The sharp rise occurring in the transition region is a clear signature of phase co-existence.

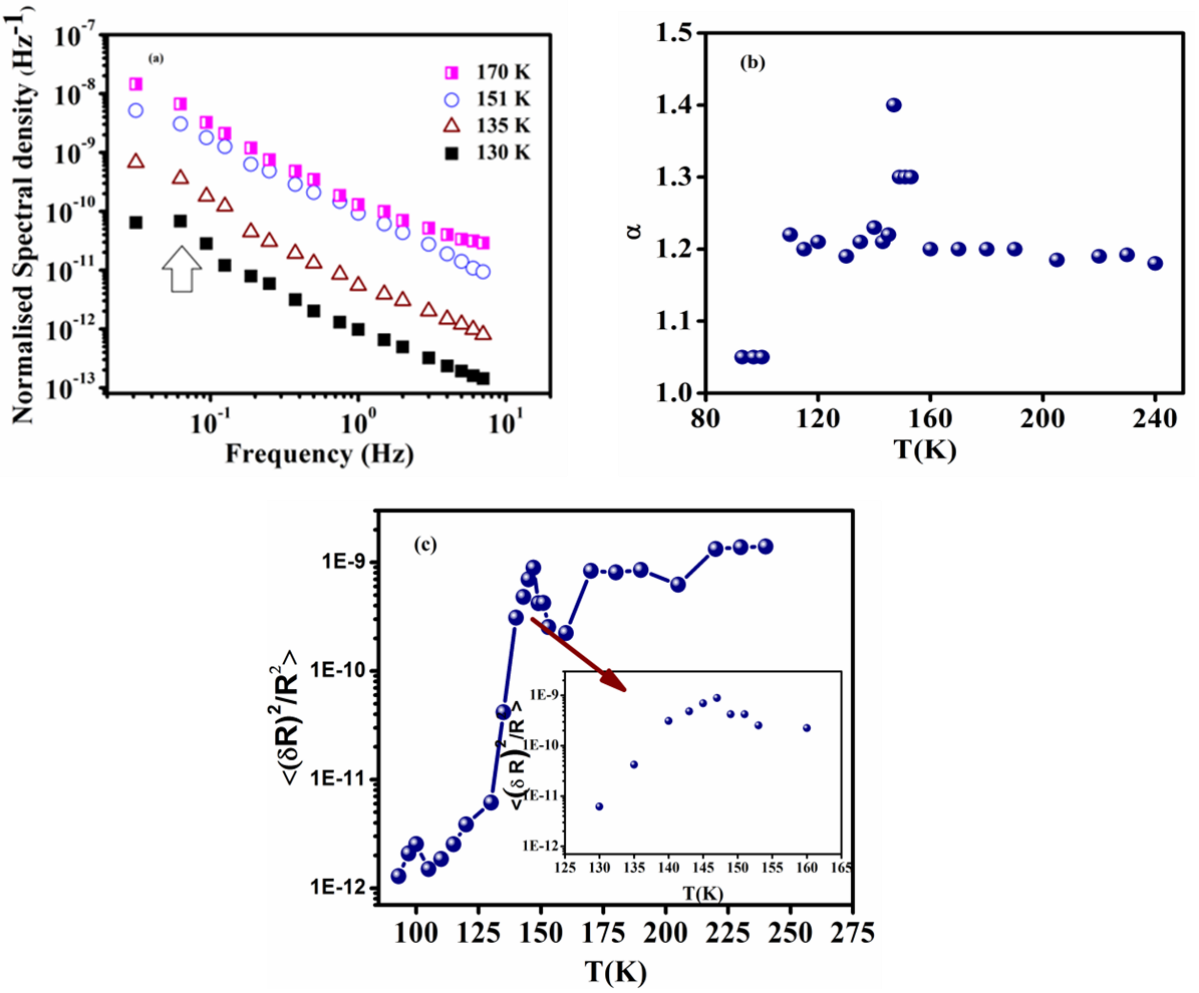

Figure 3.5 (a) Normalized spectral power density of fluctuation as a function of frequency at different temperatures (data taken during a heating cycle), (b) Variation of the exponent α with temperature T, and (c) Normalized mean square resistance fluctuation shown as a function of temperature T. The inset shows the expanded part of the marked region.

This is similar to that seen in the region of MIT in $SmNiO_3$ and VO_2 [23, 24]. We also note that there is a sharp rise in α in the same region where the resistance fluctuation also shows a clear jump. In general in $\frac{1}{f^{\alpha}}$ noise in solids the exponent α is generally ≤ 1.2 when the fluctuation predominantly arises from activated lattice defects that act as electron scattering centers. The sudden rise of α in the transition region would mean that there is a spectral shift of fluctuation in

the low-frequency region. This can be also seen in Figure. 3.5 (a) which shows the shift for the data at two temperatures (130 K and 135 K) close to the transition.

In addition to the change in the spectral power density $S_V(f)$ as well as the fluctuation $\frac{\delta R^2}{R^2}$ evolving with the temperature that shows a clear signature of phase co-existence, we find that the resistance fluctuation becomes strongly non-Gaussian at the transition region ($T \sim T_{MI}$) where there is a sharp rise in the fluctuation. To establish the non-Gaussian behavior we calculate the second spectrum which is given as:

$$S^2(f_2) = \frac{\int_0^\infty <\Delta V^{(2)}(t)\Delta V^{(2)}(t+\tau)>\cos(2\pi f_2 \tau) d\tau}{[\int_{f_L}^{f_H} S_V(f_1) df_1]^2} \qquad (3.2)$$

Where f_1 and f_2 are the frequencies associated with the first and second spectrum respectively. The spectrum has been calculated within the frequency bandwidth of 0.25 Hz, where f_1 is 0.25 Hz, f_L =0.25 Hz, and f_H = 0.5Hz. In Figure 3.6 (a) we show the second spectral density $s^2(f_2)$ as a function of frequency (f_2) at a different temperature, which shows the evolution of $s^2(f_2)$ as we approach the T_{MI}. It can be seen that there is a large jump in the spectral weight as the transition is approached. $s^2(f_2)$ is normalized by the square of the first spectrum so that for a perfect Gaussian fluctuation it is equal to 3. Any deviation from 3 would measure the extent of non-Gaussianity. The large change in the second spectrum close to T_{MI} can be better appreciated from the magnitude of the integrated normalized second spectrum, $\Sigma^2 = \int_0^{f_H - f_L} S^2(f_2) df_2$. Another way to establish the non-Gaussianity is to plot the probability distribution function as a function of mean square fluctuations. The probability distribution function for a Gaussian distribution centered at zero means follows:

$$P(|\Delta V|) = \frac{1}{\sqrt{2\pi\sigma}} \exp\left(\frac{-(|V|)^2}{\sigma}\right) \qquad (3.3)$$

For a Gaussian distribution, plotting lnP(|ΔV|) as a function of $(|V|)^2$ should give a linear plot and any deviation from the linearity would signify the non-Gaussianity. Figure 3.6 (b) represents a clear non-Gaussian tail for 140 K as we approach the phase co-existence region.

Figure 3.7 shows the integrated value of the second spectra Σ^2 over the entire temperature range. It can be seen that there is a rise in Σ^2 of nearly 1.5 orders in the transition region. We also show the $\frac{d\rho}{dT}$ in the same graph. There is a clear dependence of Σ^2 on $\frac{d\rho}{dT}$. At a temperature greater than 180 K (in the metallic region) where $\frac{d\rho}{dT}$ is more or less constant and positive, Σ^2 is low and also constant. For temperature, less than 180 K, as the transition region is approached $\frac{d\rho}{dT}$ changes sign and the resistance starts to change rapidly. At this range, Σ^2 shows a rapid rise and eventually at a lower temperature as $\frac{d\rho}{dT}$ starts to approach a high (negative) value, Σ^2 passes through a peak and also goes to a low value. In the region marked by arrows in Figure 3.7,

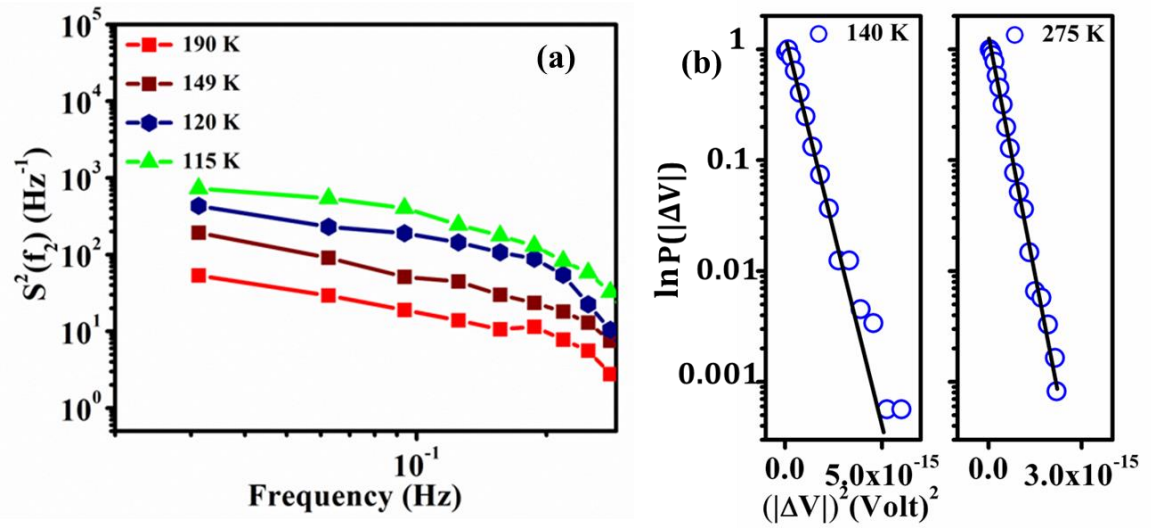

Figure 3.6 (a) Normalized second spectra $S^2(f_2)$ calculated at different temperatures and (b) probability distribution function for a Gaussian and non-Gaussian fluctuation (non-linear tail).

Where the relative volume fraction of the two co-existing phases changes, Σ^2 shows a large value. Figure 3.7 clearly establishes that the inhomogeneity (resulting from the two co-existing phases)

as observed in the spatially resolved tunneling spectra also leads to phase co-existence of two phases with different electrical conductivities which is picked up by the noise data as well.

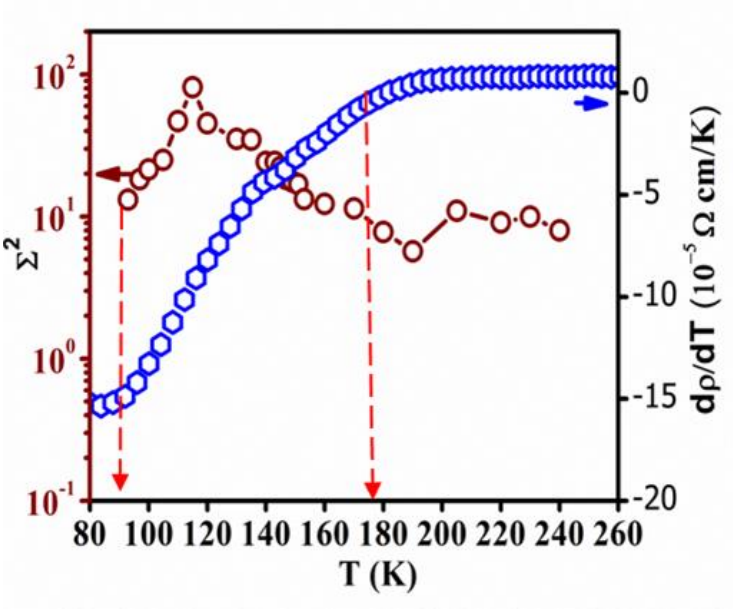

Figure 3.7 Normalized variance (Σ^2) of second spectra and $\frac{d\rho}{dT}$ as a function of temperature T, the arrows mark the region of phase co-existence.

3.6 Additional confirmation of phase co-existence by Impedance Spectroscopy

In this section, we will present an additional confirmation using impedance spectroscopy. The STS as well as the 1/f noise data, clearly establish that there is a phase co-existence of two phases with different tunneling as well as electrical conductivities. These two co-existing phases will have interface regions where the charge relaxation will be controlled by the electrical conductivities of the surrounding regions. Close to MIT, it may happen that regions of higher conductivities will be surrounded by regions of lower conductivities. These regions will then behave as "capacitors". It has been shown recently [27] that the existence of such internal interfaces between co-existing phases may enhance the dielectric constant. We carried out impedance spectroscopy to provide additional support to the observation of phase co-existence.

Impedance spectroscopy in the film was measured using an LCR meter in a frequency range of 40 Hz to 1 MHz in the temperature range 80 K to 300 K. To avoid the stray capacitance from the connecting cables we performed the open circuit and short circuit compensations. The detailed

impedance (Z) data taken in the heating cycle (Total impedance (Z) as a function of frequency and temperature) are given in Figure 3.8 (a) and (b). The impedance data were fitted with a model with equation 3.4. Inset in Figure. 3.10 shows the model. The R_c, C_c, and R_s were modelled as contact resistance, samples capacitance including stray capacitance and sample resistance respectively. The impedance data of the film can then be given by the following relation:

$$Z(\omega) = R_s + \frac{R_c}{1+j\omega R_c C_c} \qquad (3.4)$$

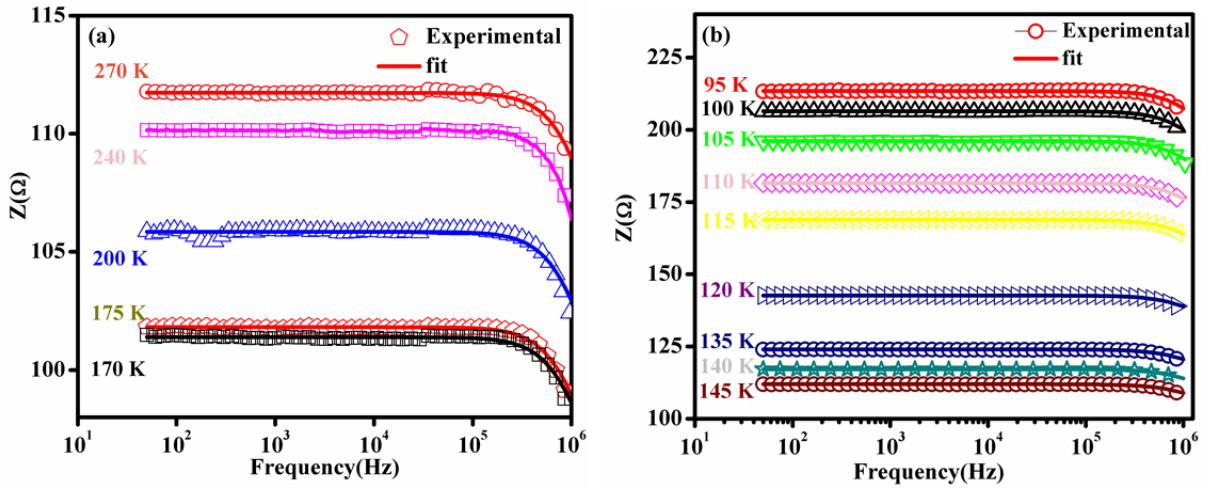

Figure 3.8 Total impedance (Z) as a function of frequency and temperature, the solid lines show the fit to equation 3.4.

In equation 3.4, for $\omega \to 0$, $R_C + R_S \approx$ 2- probe dc sample resistance between the leads. From the values of R_S and R_C obtained from the fit of the data at different temperatures, it was validated that it is indeed the 2- probe dc sample resistance between the leads. This is shown in Figure 3.9. The value of the capacitance C_c as a function of the scaled temperature $\frac{T}{T_{MI}}$ is shown in Figure 3.10. It is interesting that C_c shows a broad peak around $\frac{T}{T_{MI}} \approx 1$ where the resistance fluctuation ($\frac{\delta R^2}{R^2}$) as well as the second spectrum of the fluctuation (Σ^2) also show a peak. The value of the capacitance C_c remains high even well into the metallic phase up to $\frac{T}{T_{MI}} \approx 1.6$ and then starts to go done beyond that. It is likely that at this temperature the phase co-existence begin to appear. This

is corroborated by the temperature variation of the integrated second spectrum Σ^2 (see Figure 3.7) where we observe that Σ^2 starts to rise at T ≈ 180 K.

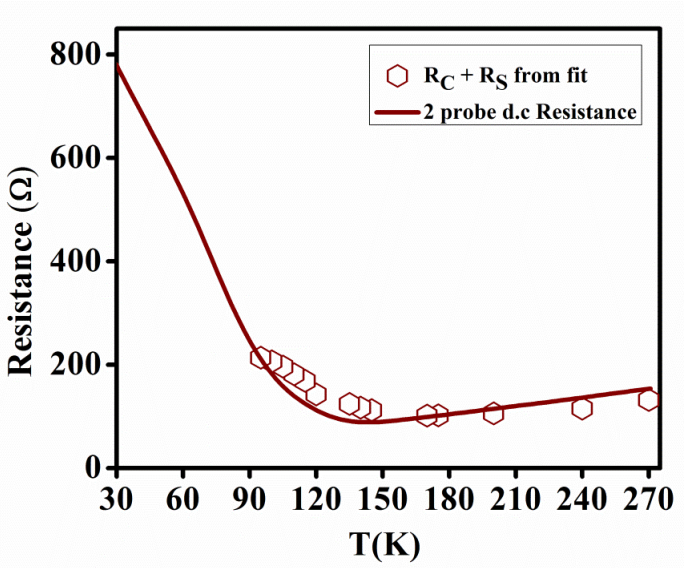

Figure 3.9 The 2 probe dc resistance and the total resistance ($R_C + R_S$) obtained from the fit shown as a function of T.

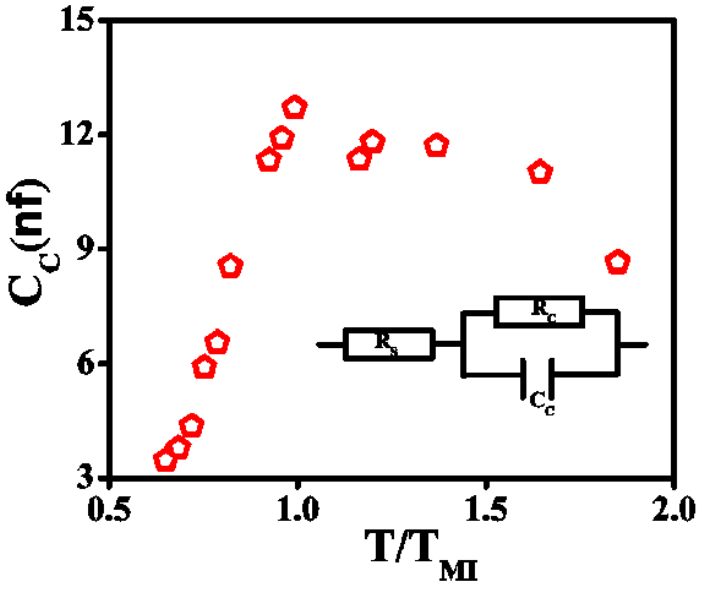

Figure 3.10 Capacitance C_c as a function of T/T_{MI}

3.7 Discussion

The results of the STS presented in this chapter clearly show two co-existing phases (with nanoscopic dimensions), one phase which has a depletion in DOS and a metallic phase which has no depletion in DOS. Using 1/f noise spectroscopy (including analysis of fluctuations of higher moments) as well as impedance spectroscopy we show that these two phases have different electrical conductivities. The volume of these two phases, as well as relative values of their conductivities also evolve on cooling. The low conducting phase (depleted DOS) most likely evolves into the insulating phase. While no claim can be made of the generality of this observation in the case of films of other oxides undergoing MIT, the observation nevertheless has a generic content that may apply to other systems as well.

The observations that we made depend on crucial physics that there is indeed co-existence of a phase with depleted DOS in $NdNiO_3$ and more importantly the DOS in such a system becomes spatially dependent. We argue that recent theoretical developments indeed lead to this type of scenario in strongly correlated oxides. Predictions of a soft-gap in presence of correlation (long-range Coulomb interaction) and disorder with parabolic energy dependence near E_F have been known for a long time [1, 2]. Recently, it has been shown that a soft gap or a depleted DOS (with a power-law density of state) can arise even for short-range interaction [4]. These approaches, however, don't raise the possibility of phase separation of a DOS depleted phase and a metallic phase so that one may have electronic phase-separation and phase co-existence. The possibility of interactions leading to a situation of electronic phase separation has been proposed in the context of manganites [28]. It was proposed that electrons populating the doubly degenerate e_g state (around Mn ions) can have the presence of two types of carriers. One type is a band like electrons and the other type is more localized polaronic states. Existence of strong Coulomb repulsion between the two types of electrons was shown to lead to nanoscopic phase separation. There is an apparent similarity of this picture which has been observed by the STS data. The electrons in nickelates have strong interaction with the lattice and have polaronic nature. However, it is not clear at this stage whether a similar scenario exists in nickelates that one may observe a phase separation. Another scenario may also be considered. It has been suggested that the strain breaks the degeneracy of the Spin-Orbit and Crystal Field-Effect determined e_g orbitals [13, 29]. The occupancy of the orbitals split by the strain would depend on the nature of the strain

(compressive/tensile). Presence of local strain inhomogeneity can, in fact, lead to occupancy of orbitals of different type and thus different phases. More recently the observation of negative magnetoresistance for $NdNiO_3$ films suggest that the emergence of the Zeeman splitting of localized states due to the thermally induced local disorder may also lead to such phase co-existence [30].

Our investigation of phase co-existence deals with two fluctuations: the temporal fluctuation, as recorded by the noise spectral power, and the spatial fluctuation that has been observed through a scanning probe like STS. A pertinent question arises whether a direct connection can be established between the two. The phase co-existence has been probed by both the probes yet it is not straight forward to establish a quantitative connection between the two. This is because of the time scales of observations and data acquisition associated with the two probes are different. The map of the local conductance g from which the spatial fluctuation has been observed has been taken over a time scale of ~ 2.5 sec at a given spot. The noise spectra have been acquired over a time scale of ~ 16 minutes. This gives the time scale (spectrally resolved) of the dynamics that are associated with the resistance fluctuations. In the scale over which the fluctuation is imaged by STS image can thus be considered as a "snap-shot" of the temporal fluctuation. The spatial data also has an averaging effect over a longer time scale due to small and random thermal drift that blurs out some of the contrast in the images of spatial fluctuation. Due to these effects, the time scale associated with the spatial fluctuations cannot be uniquely specified. As a result, no tight quantitative correlation between the temporal fluctuation (noise spectroscopy) and the spatial fluctuation (STS) data can be established although one can image by STS the spatially resolved fluctuation over a finite time scale.

The large resistance noise, in particular, the non-Gaussian fluctuation, arises in the transition range. In this temperature range the STS data show the metallic regions (regions with large tunneling conductance) have low volume fraction and are not connected. However, they can carry large current density, this may lead to a charging and discharging of the metallic islands which are separated by a phase of low conductance. This phenomenon can give rise to large noise due to charge fluctuation. The large non-Gaussian component of the fluctuation arises from the transport through a system that has such isolated metallic islands due to the correlation of the current paths that develop by a random (and dynamic) time-dependent distribution of current paths [31, 32].

3.8 Conclusion

To conclude, our study established that the MIT in a film $NdNiO_3$ shows phase separation in the nanoscopic scale (few tens of nanometers) and phase co-existence. We have used three techniques namely scanning tunneling spectroscopy (STS), noise spectroscopy and impedance spectroscopy (IS) experiments to establish the phase co-existence. The local conductance map generated from the STS shows that how the inhomogeneity is associated with the phase co-existence. The two co-existing phases (with nanoscopic dimensions) have different contribution to the DOS, where one phase has depletion in DOS and a normal metallic phase which has no depletion in DOS. It appears that the phase co-existence may actually start well above the MI transition temperature ($\frac{T}{T_{MI}} \approx 1.6$) and the system becomes highly "inhomogeneous" electronically close to the transition temperature. We suggest that such phenomena reported in the context of $NdNiO_3$ may actually be generic in nature. Such phase separation may be associated with other strongly correlated systems that show a temperature-driven MIT.

Bibliography for Chapter 3

1. N. F. Mott, Metal-Insulator Transition. Taylor & Francis, London (1990).
2. M. Imada, A. Fujimori, and Y. Tokura, Rev. Mod. Phys. 70, 1039 (1998).
3. A. K. Raychaudhuri, K. F. Rajeev, H. Srikanth, and N. Gayathri, Phys. Rev. B 51, 12 (1995).
4. S. James Allen, A. J. Hauser, E. Mikheev, J. Y. Zhang, N. E. Moreno, J. Son, D. G. Ouellette, J. Kally, A. Kozhanov, L. Balents and S. Stemmer, APL Materials 3, 062503 (2015).
5. H. Shinaoka and M. Imada, Phys. Rev. Lett. 102, 016404 (2009).
6. N. Gayathri, A. K. Raychaudhuri, X. Q. Xu, J. L. Peng, and R. L. Greene, J. Phys. Condens. Matter 10, 1323 (1998).
7. D. D. Sarma, A. Chainani, S. R. Krishnakumar, E. Vescovo, C. Carbone, W. Eberhardt, O. Rader, Ch. Jung, Ch. Hellwig, W. Gudat, H. Srikanth, and A. K. Raychaudhuri, Phys. Rev. Lett. 80, 4004 (1998).
8. G. Mattoni, P. Zubko, F. Maccherozzi, A. J. H. van der Torren, D.B. Boltje, M. Hadjimichael, N. Manca1, S. Catalano, M. Gibert, Y. Liu, J. Aarts, J. M. Triscone, S. S. Dhesi and A. D. Caviglia, Nat. Commun. 7, 13141 (2016).
9. G. Catalan, R. M. Bowman, and J. M. Gregg, Phys. Rev. B 62, 7892 (2000).
10. Daniele Preziosi, Laura Lopez-Mir, Xiaoyan Li, Tom Cornelissen, Jin Hong Lee, Felix Trier, Karim Bouzehouane, Sergio Valencia, Alexandre Gloter, Agnes Barthe`lémy,´ and Manuel Bibes, Nano Lett. 18, 2226−2232 (2018).
11. K. W. Post, A. S. McLeod, M. Hepting, M. Bluschke, Yifan Wang, G. Cristiani, G. Logvenov, A. Charnukha, G. X. Ni, Padma Radhakrishnan, M. Minola, A. Pasupathy, A. V. Boris, E. Benckiser, K. A. Dahmen, E. W. Carlson, B. Keimer and D. N. Basov, Nature Physics | VOL 14 | OCTOBER 2018 | 1056–1061
12. T. Katsufuji, Y. Okimoto, and Y. Tokura, Phys. Rev. Lett. 75(19), 3497 (1995)
13. M. K. Stewart, J. Liu, M. Kareev, J. Chakhalian, and D. N. Basov, Phys. Rev. Lett. 107, 176401 (2011).
14. J. Mitra and A. K. Raychaudhuri, Y. M. Mukovskii and D. Shulyatev, Phys. Rev. B 68, 134428 (2003).

15. J. Mitra, M. Paranjape, A. K. Raychaudhuri, N. D. Mathur and M. G. Blamire, Phys. Rev. B 71, 094426 (2005).
16. P. P. Edwards, R. L. Johnston, C. N. R. , Rao, D. P. Tunstall, & F. Hensel, Phil. Trans. R. Soc. Lond. A 356, 5–22 (1998).
17. A.K. Raychaudhuri, Advances in Physics 44 (1), 21-46.
18. http://www.rhk-tech.com/support/tutorials/
19. E. L. Wolf, Principles of Electron Tunnelling Spectroscopy, Oxford University Press, Oxford, 1989.
20. A. K. Raychauduri, K. P. Rajeev, H. Srikanth, and R. Mahendiran, Physica B 197, 124 (1994).
21. Efros A L and Pollak M 1985 Electron-electron interaction in disordered systems (Amsterdam: Elsevier)
22. A. Ghosh, S. Kar, A. Bid, and A. K. Raychaudhuri, , arXiv:cond-mat/ 0402130v1 (2004).
23. S Samanta, A. K. Raychaudhuri, Xing Zhong and A. Gupta, Phys. Rev B 92, 195125 (2015).
24. A. Sahoo, S. D. Ha, S. Ramanathan, and A. Ghosh, Phys. Rev. B 90, 085116 (2014).
25. A. Ghosh and A. K. Raychaudhuri, Phys. Rev. B 64, 10430 (2001).
26. A.K. Raychaudhuri, Curr. Opin. Solid State Mater. Sci., 6, 67–85 (2002).
27. P. Lunkenheimer, S. Krohns, S. Riegg, S.G. Ebbinghaus, A. Reller, and A. Loidl, Eur. Phys. J. Special Topics 180, 61–89 (2010).
28. V. B. Shenoy, T. Gupta, H. R. Krishnamurthy, and T. V. Ramakrishnan, Phys. Rev. Lett. 98, 097201 (2007).
29. I. C. Tung, P. V. Balachandran, J. Liu, B. A. Gray, E. A. Karapetrova, J. H. Lee, J. Chakhalian, M. J. Bedzyk, J. M. Rondinelli, and J. W. Freeland, Phys. Rev. B 88, 205112 (2013).
30. A. Stupakov, O. Pacherova, T. Kocourek, M. Jelinek, A. Dejneka, and M. Tyunina, Phys. Rev. B 99, 085111 (2019)
31. S. Kar, A. K. Raychaudhuri, A. Ghosh, H. V. Lohneysen, and G. Weiss, Phys. Rev. Lett. 91, 216603 (2003).
32. L. M. Lust and J. Kakalios, Phys. Rev. Lett. 75, 2192 (1995).

Chapter 4 Continuous transition from weak localized regime to a strongly localized regime in $Nd_{0.7}La_{0.3}NiO_3$ films

In this chapter, we show how a combination of factors like strain, substrate symmetry, and disorder plays an important role in the transport properties and can change the nature of the metal-insulator transition (MIT). The combination of these factors make substituted nickelates ($Nd_{0.7}La_{0.3}NiO_3$) (that are known to exhibit first-order Mott type transition), undergo a continuous transition as seen in systems undergoing disorder/composition driven Anderson transition. Our investigation was done on $Nd_{0.7}La_{0.3}NiO_3$ films grown on crystalline substrates of $LaAlO_3$ (LAO), $SrTiO_3$ (STO), and $NdGaO_3$ (NGO) by pulsed laser deposition (PLD). The conductivity measurement shows that film grown on LAO experiences a compressive strain and shows metallic behavior with the onset of a weak resistivity upturn below 2 K which is linked to the onset of weak localization (WL) contribution. Films grown on STO and NGO show a cross-over from a Positive Temperature Coefficient (PTC) resistance regime to Negative Temperature Coefficient (NTC) resistance regime at definite temperatures. Our results establish that a cross-over from PTC to NTC does not necessarily constitute an MIT since the extrapolated conductivity at zero temperature ($\lim_{T\to 0} \sigma = \sigma_0$) is small, but finite, which shows a signature of the bad metallic state as well as an absence of an activated transport.

4.1 Introduction

Often the metal-insulator transition temperature (T_{MI}) is identified as a cross-over from a positive temperature coefficient of resistivity (PTC) ($\frac{d\rho}{dT} > 0$) to a negative temperature coefficient of resistivity (NTC)($\frac{d\rho}{dT} < 0$). However, without any qualification, this does not necessarily mean entry to an insulating state and the cross-over temperature cannot be recognized as T_{MI}. For many cases, this identification of metal-insulator transition (MIT) may indeed be correct but the pristine definition of the insulating state tells that the conduction is activated and an absence of conduction by the extended state would mean $\lim_{T\to 0} \sigma \to 0$. There is enough evidence to suggest that a cross-over from PTC to NTC region may occur when $\sigma < \sigma_{Mott}$ and it has been seen in many disordered oxides as well as semiconductors [1-6]. The continuous MIT has been widely studied in oxides like $LaNiO_3$, $SrRuO_3$, $LaNi_{1-x}Co_xO_3$, $NaOsO_3$, and Na_xWO_3 [7-12]. These studies show that the role of disorder, reduced dimensionality, and renormalization of electron-electron interactions at a lower temperature can give rise to an upturn in the resistivity which may be considered as a quantum correction to the conductivity [6-10].

In such a system, the tunneling conductance (that measures the density of states (DOS) at the Fermi level (E_F)) can become temperature dependent due to the presence of correlations. This has been predicted theoretically and also observed in oxides as well as doped semiconductors [13]. It has been seen that quantum-confined $LaNiO_3$ shows such a transition from first-order MIT to Anderson transition [10]. Theoretical investigations have also raised the possibility that disorder in a Mott insulator can tune the MIT to a continuous transition [14, 15]. The disorder-induced continuous transition has been proposed in the context of a half-filled Anderson Hubbard model at a finite temperature where the quenched disorder, as well as the auxiliary field fluctuations, is responsible for Non-Fermi Liquid scaling [14].

Coming to the nickelates, the MIT in substituted nickelates ($Nd_{1-x}La_xNiO_3$) has been investigated for different x. The temperature dependent resistivity measurements show that $Nd_{1-x}La_xNiO_3$ ($x > 0.4$) system is completely metallic with a temperature-driven metallic to semiconductor transition for $x \leq 0.35$ [7, 16]**.** Results on $Nd_{1-x}La_xNiO_3$ thin films suggests that the MIT looks similar to their bulk counterpart, but a change in the lattice constant and the Ni-O bond angle shifts the T_{MI} to a slightly lower temperature [7]. Our study has been principally motivated by the identification of

metallic and insulating state in $Nd_{1-x}La_xNiO_3$ when x is close to x_c and modifications that occur due to strain, quenched disorder (due to substitution) and orthorhombic distortion.

Our investigations focus on $Nd_{0.7}La_{0.3}NiO_3$ system. The substitution of Lanthanum (La) in (Neodymium) Nd ($Nd_{1-x}La_xNiO_3$) poses an interesting set of questions. For x below a certain La concentration x_c ($x_c \approx 0.35$ discussed below) the finite T_{MI} is sustained as expected for a temperature-driven MIT. However, for $x_c \geq 0.35$ the transition may take the characteristics of a composition driven MIT as seen for Anderson transition. It is expected that for a critical concentration of La the transition would show features of both "Mott" and "Anderson" transition, the issues like weak localization (WL) and quantum corrections to conductivity will appear to contribute with the Mott-type transition. In this regime along with strain, factors like quenched disorder (cationic disorder) will also play an important role.

Conventional wisdom says that in a system like $Nd_{1-x}La_xNiO_3$, where the insulating state is severely suppressed due to the presence of La, the cross-over from PTC to NTC does not necessarily mean MIT. This issue assumes particular renewed significance in doped $NdNiO_3$ as in $Nd_{1-x}La_xNiO_3$, where, there exists a critical concentration (x_c) and it becomes metallic for $x > x_c$ (as discussed before). The question that we would like to raise and investigate is whether the transition from PTC to NTC close to x_c can be a continuous transition and the cross-over from a PTC to NTC at some finite temperature T^* need not necessarily signify MIT as one would see in a Mott type transition.

In this chapter, the issue of continuous transition for the substituted $Nd_{1-x}La_xNiO_3$ (x = 0.3) system has been investigated in the context of perturbative effects from physical factors like strain, substrate symmetry, and quenched disorder that can tune the nature of the transition. The particular composition being used here $Nd_{1-x}La_xNiO_3$ (x = 0.3) is at the verge of a composition driven MIT. In the bulk, the sample with x = 0.3 shows a metallic behavior at a higher temperature and an upturn in resistivity at a lower temperature [16]. The resistivity data down to 4.2 K was interpreted using variable range hopping, indicating an insulating state. Thin films (8 Unit Cell) of $Nd_{1-x}La_xNiO_3$ (x = 0.25) grown on $LaAlO_3$ show a metallic resistivity down to 75 K and an upturn in resistivity below 75 K [7]. If upturn in resistivity is taken as T_{MI}, the phase diagram of $Nd_{1-x}La_xNiO_3$ films suggests that $x^* \sim 0.35$ [7]. In both the studies, an upturn in resistivity was

identified as T_{MI}. From the $x - T_{MI}$ phase diagram, it appears that the composition x = 0.3 is on the insulating side though close to the composition driven MIT.

Our investigation has been done on films of $Nd_{1-x}La_xNiO_3$ (x=0.3) grown on single-crystal substrates of $LaAlO_3$ (LAO), $SrTiO_3$ (STO) and $NdGaO_3$ (NGO). The crystal structures of substrates used LAO (100), STO (100), and NGO (100) are rhombohedral, cubic, and orthorhombic respectively, as seen in Figure 4.1.

The main motivation for choosing different substrate are:

- To vary the amount of built-in strain that ranges from compressive to tensile.
- The cubic symmetry imposed by the LAO and STO due to their cubic nature while orthorhombicity for film grown on NGO.
- The orthorhombic distortion imposed by the NGO (100) which can push the transition temperature to a higher value and it has been already reported for $NdNiO_3$ [17].

The question we have asked here is, even if we tune the transition to a somewhat higher temperature (by inducing orthorhombic distortion using NGO (100)), does the nature of transition retain its first order character or it shows a metallic state albeit with very low $\sigma\ (T = 0)$, but finite.

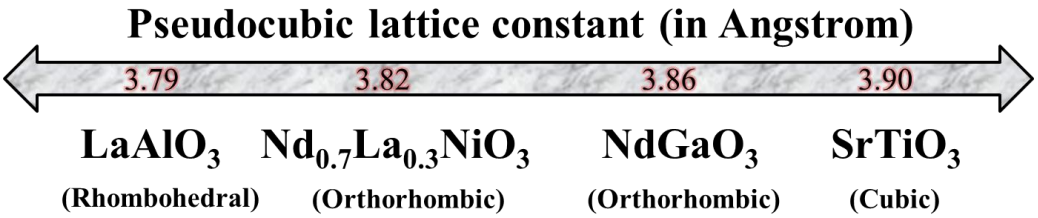

Figure 4.1 The pseudocubic lattice parameters and symmetry of substrates used and $Nd_{0.7}La_{0.3}NiO_3$ bulk.

4.2 Substrate induced strain in $Nd_{0.7}La_{0.3}NiO_3$ films

In this section, we will discuss the nature of strain experienced by the films when they have grown on different crystallographic substrates. The X-ray diffraction (XRD) $\theta - 2\theta$ scan is plotted in Figure 4.2, where the intensity is plotted in log scale. This rules out the presence of any other phase and the data show that the films are free from minority/impurity phases. The monitored XRD peaks for substrates match with their standard Braggs reflection. The full width at half maxima (FWHM)

was calculated by performing a peak fitting. The different 2θ values for films indicate a change in lattice parameters due to the substrate-induced strain. To quantify the strain, in-plane misfit strain ($\epsilon_{in-plane}$) has been calculated as follows:

$$\epsilon_{in-plane} = \frac{a_{sub} - a_{bulk}}{a_{bulk}} \qquad 4(a)$$

Where a_{sub} and a_{bulk} are the pseudocubic lattice parameter of substrate and NLNO bulk respectively. The out of plane strain ($\epsilon_{out\ of\ plane}$) was calculated as follows:

$$\epsilon_{out\ of\ plane} = \frac{2\nu}{(\nu-1)} * \epsilon_{in-plane} \qquad 4(b)$$

Where ν is the Poisson ratio. For $NdNiO_3$, $\nu = 0.25$ [18] and the out of plane strains are given as $\epsilon_{out\ of\ plane}$ = -0.66$\epsilon_{in-plane}$. The orthorhombic NLNO film and NGO substrates can be represented in pseudocubic notation as $a_{pc} = b_{pc} = \frac{1}{2}\sqrt{(a_{or}^2 + b_{or}^2)}$ and $c_{pc} = \frac{c_{or}}{2}$.

The XRD data show that NLNO/LAO and NLNO/STO films are strongly textured in the (110) direction with a similar full width at half maxima (FWHM), while NLNO/NGO film is textured along (100) direction with a relatively low value of FWHM. (The Miller indices of peaks from which FWHM are calculated are given in Table 4.1). The different growth directions and FWHMs can be attributed to the fact that films NLNO/STO and NLNO/LAO have a cubic symmetry while the film NLNO/NGO has an orthorhombic symmetry which arises from the different crystallographic nature of the substrates. In Table 4.1 the relevant structural parameters like lattice parameters (a, b, c), pseudocubic lattice parameters (a_{pc}), crystal structures, strains, growth directions and FWHM are summarized. The in-plane strain is compressive for the film NLNO/LAO while it is tensile for the films NLNO/STO and NLNO/NGO. The in-plane strain is expected to be almost isotropic for the films grown on rhombohedral LAO ($a = b \neq c$) and cubic STO ($a = b = c$) substrates since a, and b can change freely in (110) direction, this has been shown for $SrRuO_3$ (110) and $NdNiO_3$ (110) films [17, 19, 20]. However, due to orthorhombic distortions ($a \neq b \neq c$), the in-plane biaxial strain in the NLNO/NGO film is expected to be anisotropic. The XRD thus establish that the substrate symmetry plays an important role in the film growth and nature of strain experienced.

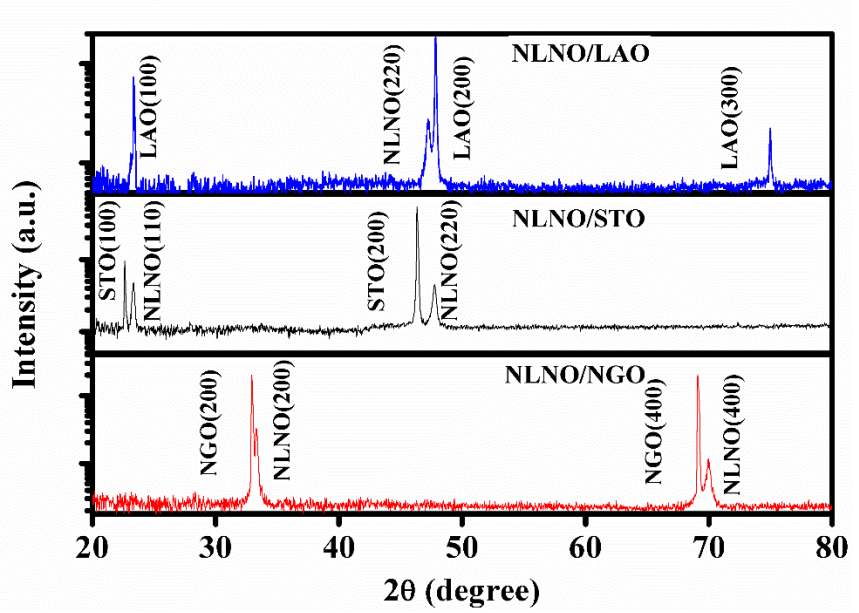

Figure 4.2 XRD scan of NLNO films grown on LAO, STO, and NGO single crystal substrates. The intensities are plotted on log scales.

Due to relatively larger thickness, films are not coherently strained as it happens in very thin films (few unit cells). Nevertheless, a mismatch between substrate and film lattice constants lead to interfacial strain and the relaxation of interfacial strain leads to additional disorder. This adds to the quenched disorder arising from a random substitution of Nd (1.163A°) by La (1.216A°) [21, 22]. This two quenched disorders would contribute to electronic transport in this system.

Table 4.1 Structural parameters of NLNO bulk, substrates, strain, and FWHM as obtained from XRD curves. The subscript in FWHM shows the Miller indices for the peaks for which FWHM was calculated.

Sample	Crystal Structure	a (Å)	b (Å)	c (Å)	a_{pc}(Å)	FWHM(Miller Indices)	$\epsilon_{in-plane}$	$\epsilon_{out\ of\ plane}$
NLNO(bulk) [16]	Orthorhombic	5.403	5.377	7.644	3.82	-	-	-
LAO	Rhombohedral	3.79	3.79	13.11	3.79	$0.27_{(220)}$	-0.79	0.52
STO	Cubic	3.905	3.905	3.905	3.905	$0.30_{(220)}$	2.22	-1.46
NGO	Orthorhombic	5.43	5.50	7.71	3.86	$0.18_{(200)}$	1.04	-0.68

4.3 Resistivity as a function of temperature down to 0.3 K

To check whether the films grown on different substrates show a transition from PTC to NTC, the resistivity as a function of temperature down to 0.3 K was measured in a collinear four-probe configuration. The resistivity (ρ) data for all the films are shown in a linear temperature scale in Figure 4.3. Data have been taken in the heating cycle. At room temperature, ρ is lowest in NLNO/LAO with compressive in-plane strain and highest for the film NLNO/STO which has highest built-in in-plane tensile strain (Table 4.1). The derivative $\frac{d\rho}{dT}$ has been used to mark the cross-over temperature T^* from PTC to NTC behavior. The derivative $\frac{d\rho}{dT} = 0$ defines T^*. A clear cross-over with well-marked T^* has been seen for the films with tensile strains (grown on NGO and STO, marked by arrows) while for the film with compressive strain grown on LAO, no clear T^* is observed. ρ for NLNO/NGO at 300 K is substantially lower than that of NLNO/STO. However, due to rather large $T^* \approx 150$ K, at lower temperature ρ of the film, rises rapidly on cooling and for $T < 50$ K, it becomes larger than that of the NLNO/STO film.

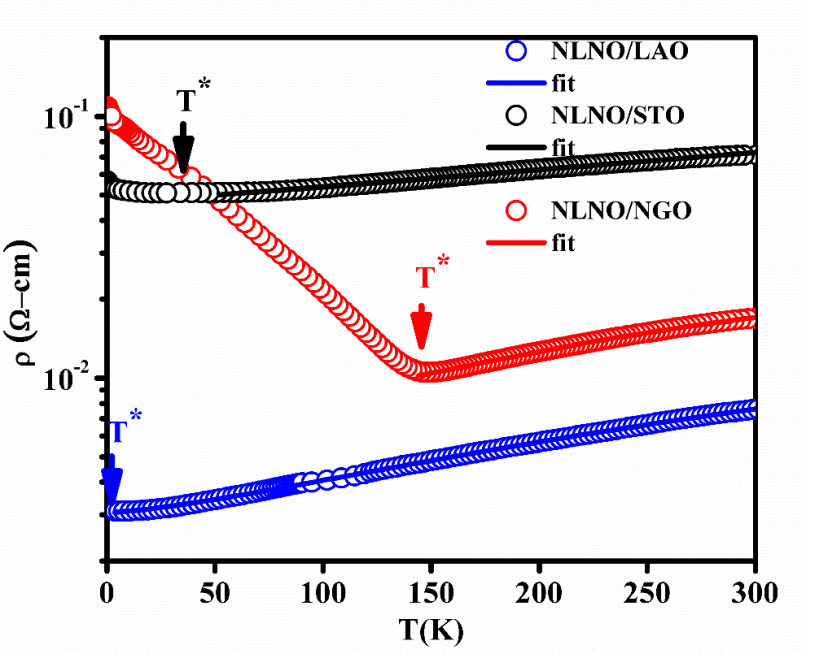

Figure 4.3 Resistivity (ρ) as a function of temperature T for NLNO films grown on LAO, STO, and NGO single crystal substrates. The fit to equation 4.3 are shown as solid lines.

4.3.1 Interpretation of extrapolated zero temperature conductivity

To understand the behavior of conductivity as T → 0, we have converted the resistivity data into conductivity. Conductivity $(\sigma(T))$ data for the three samples for the entire temperature range (0.3 K - 300 K) are shown in Figure 4.4. The films with tensile strain, $\sigma(T)$ shows positive temperature coefficients of conductivity ($\frac{d\sigma}{dT} > 0$) below 100 K, as has been seen at low-temperature limits in transition metal oxides close to the composition driven MIT [2, 3, 13]. It is well known that the power laws at low temperature follow the relation $\sigma = \sigma_0 + mT^p$ for metals and $\sigma = \sigma_0\, exp\left(-\left(\frac{T_0}{T}\right)^p\right)$ for insulators. For metals, $\frac{dln\sigma}{dlnT} \to 0$ as the temperature approaches 0 K while for insulators $\frac{dln\sigma}{dlnT} \to \infty$ as the temperature approaches 0 K [1, 2].

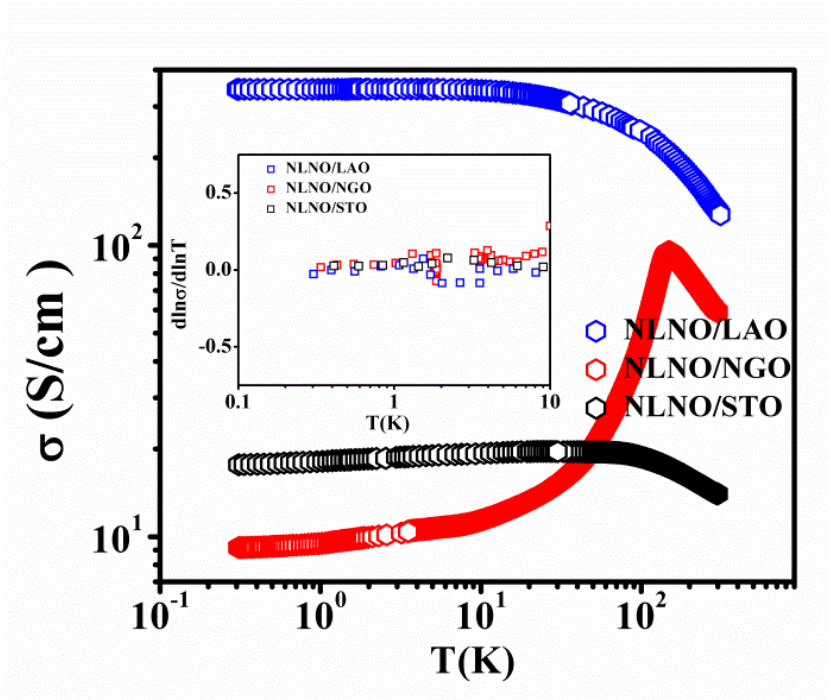

Figure 4.4 Conductivity (σ) as a function of temperature T in the three films of NLNO grown on LAO, STO, and NGO single crystal substrates. The inset shows the derivative $W \equiv \frac{\text{dln}\sigma}{\text{dln}T}$ as a function of temperature for T < 10 K.

To establish that the conductivity though low, reaches a finite value as T → 0 ($\lim_{T\to 0} \sigma(T) \neq 0$), we have plotted the derivative $W \equiv \frac{dln\sigma}{dlnT}$ vs T in the inset of Figure 4.4 for T ≤ 10 K [18, 37]. For an insulator, $\lim_{T\to 0} \sigma(T) = 0$ due to activated nature of the conductivity, and W diverges as T → 0.

On the contrary, when $\sigma(T)$ approaches a finite value however small it may be, $\lim_{T\to 0}\sigma(T) \neq 0$, $W \to 0$ as $T \to 0$. Inset of Figure 4.4 shows that in all the three films indeed $W \to 0$ as $T \to 0$ signifying a finite zero temperature conductivity. This establishes that at low temperatures in all the three films $\lim_{T\to 0}\sigma(T) \neq 0$. For NLNO/LAO $\lim_{T\to 0}\sigma(T) \sim 300$ S/cm, in films with tensile strain, $\sigma(T)$ though finite are very low, particularly in the film NLNO/NGO.

The data thus support the hypothesis that a combination of physical factors like the strain, lattice symmetry, as well as disorder can make the MIT continuously tunable close to a critical composition on La substitution and the first-order MIT seen in NNO is not observed. In general, in a disordered system, it has been shown that strain, hydrostatic pressure, as well as disorder, can tune in a continuous MIT as has been shown in Si:P system close to the critical P concentration [1, 23-26]. This is also well documented for other disordered oxides [1-6, 8-10]. In La substituted NLNO, approach to the MIT thus assumes the nature of a disorder and composition driven Anderson transition.

The approach to MIT in the low-temperature regime in an Anderson transition generally follows a power law in the metallic side of the transition [25]. The $\sigma(T)$ vs T data at low T ($T \leq 2$ K) is fitted with a power-law in linear scale (Figure 4.5 (a)) to derive the limiting conductivity:

$$\sigma(T) = \sigma_0 + \mathrm{AT^n} \qquad (4.1)$$

The low temperature limiting power-law behavior starts in the three films at different temperatures. For NLNO/LAO it starts below 2 K. For NLNO/STO it starts below 20 K and in NLNO/NGO at somewhat higher temperatures. However, to bring them on the same basis, the power laws have been fitted at $T \leq 2$ K for all the films. The exponent n evolves as σ_0 decreases when it approaches to the MIT. The data are very similar to that observed previously on a number of disordered oxides undergoing Anderson type MIT [1-3, 6, 8, 9].

Figure 4.5 (b) shows the evolution of σ_0 as a function of n, which is a parameter that measures closeness to MIT. Of particular interest is the value of $n \approx 1$ seen in the film on NGO substrate, and has the lowest value of σ_0. In oxides with similarities to NNO, it has been seen that close to the MIT, the exponent $n \to 1$ [2]. Often a scale of Mott minimum metallic conductivity (σ_{Mott}) is used as a scale of conductivity that signals a transition to a bad metallic state. For most oxides like

NNO where the charge density is in the vicinity of $10^{22} cm^{-3}, \sigma_{Mott} \sim (5-10) \times 10^2\ S/cm$. Thus for the film NLNO/LAO, $\sigma_0 \sim \sigma_{Mott}$ and for the other two films $\sigma_0 \ll \sigma_{Mott}$ .The value of σ_0 is also a small fraction of the parameter $\sigma_{MIR} (\sigma_0 \ll \sigma_{MIR} \equiv \rho_{MIR}^{-1})$, this makes the metallic state below T* a bad metallic state. We can also make a comparison with σ_{MIR} ($\sigma_{MIR} \equiv \frac{1}{\rho_{MIR}} \approx 3000 - 5000\ S/cm$).

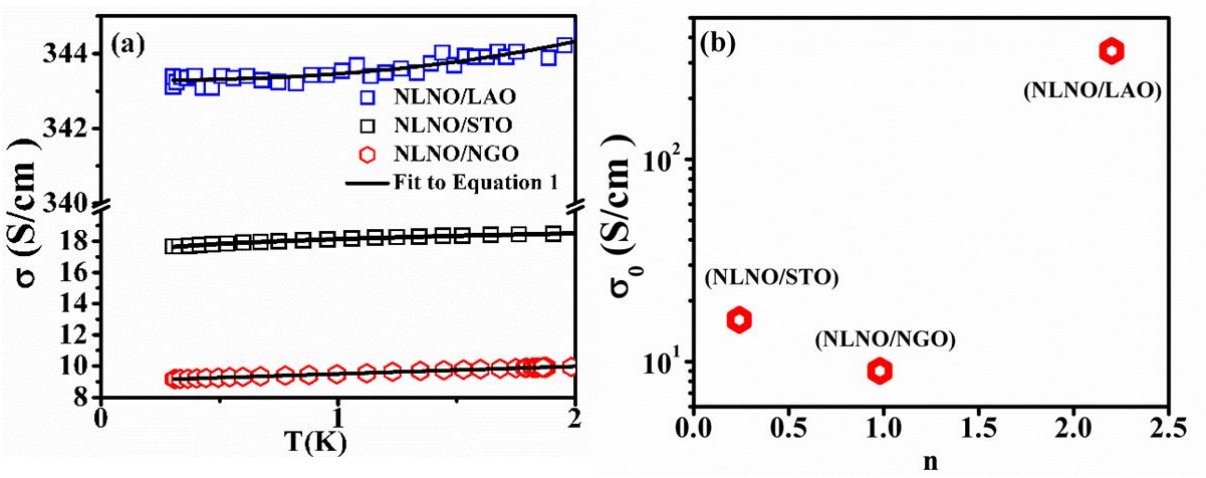

Figure 4.5 (a) The experimental data and fit to equation 4.1 for films grown on all three substrates for the range 0.3 K ≤ T ≤ 2 K and (b) σ_0 as a function of exponent n for NLNO films grown on LAO, STO, and NGO single crystal substrates.

Table 4.2 Parameter values for the fit of conductivity data to equation 4.1 for the range 0.3 K ≤ T ≤ 2 K

Sample	n	σ_0 (S/cm)	A (S/cmK^{-n})
NLNO/LAO	2.20 ± 0.240	343.28 ± 0.02	0.21 ± 0.03
NLNO/STO	0.24 ± 0.008	16.10 ± 0.06	2.03 ± 0.06
NLNO/NGO	1.02 ± 0.007	9.011 ± 0.003	0.494 ±0.004

In NLNO/LAO which has the highest conductivity, the behavior is metallic in all regions (with PTC) and the conductivity is essentially flat below 30 K with a small $\frac{d\sigma}{dT}$ as expected from corrections to conductivity arising from weak localization [2,25]. In this regime, the correction to conductivity due to disorder is small and is given by [25]:

$$\sigma(T) = \sigma_0 + kT^{p/2} \qquad (4.2)$$

Where the factor $k \equiv \frac{2e^2}{\xi h \pi^2}$, e is the electronic charge and ξ(de-phasing length scale) is related to the Thouless length $L_{TH} = \xi \mathrm{T}^{-\mathrm{p}/2}$. From weak localization theory, when the interaction effect is weak $p \approx 4$ [39], experimentally observed $n \approx 2.2$ (Table 4.2) is very close to the expected value of $p/2$. The accuracy of the estimation of n is limited due to very weak temperature dependence. In NLNO/STO, the exponent $n = 0.24$ is somewhat smaller than what is expected in this regime when electron-electron interaction is associated with weak localization. The value of n is ½ in such cases. In this case, the de-phasing length is such that it is dominated by thermal effects. As the transition is approached, the exponent in many oxides approaches a value of $n = 1/3$, which has been explained as an exponent in the metallic side close to the critical region of MIT [1]. It may happen that the Thouless length is much greater than the thickness of the film. In that case, the dominant length scale will be determined by the thickness, being smaller than Thouless length. This may also modify the exponent. There is no theory available that explains the evolution of the exponent in such a confined sample size.

4.3.2 High-temperature resistivity data ($\mathbf{T > T^*}$): A transition from Fermi liquid behavior to non-fermi liquid behavior

The resistivity $\rho(T)$ data in the temperature range $\mathrm{T} > \mathrm{T}^*$ for all the three films are fitted with a power-law of T to check whether there is a Non-Fermi Liquid (NFL) behavior present in these systems. Past studies on NNO films with compressive strain have shown the existence of NFL behavior [27, 28]. To investigate this, the data are fitted to the equation below:

$$\rho(T) = \frac{\rho^*(T)\rho_{sat}}{(\rho_{sat}+\rho^*(T))} \qquad (4.3)$$

where $\rho^*(T) = \rho_0 + B\mathrm{T}^{\mathrm{m}}$ and ρ_{sat} is a parallel high resistance when resistivity approaches the Mott-Ioffe-Regel limit [27]. The value of exponent m is 2 for a Fermi Liquid (FL) and $\frac{5}{3}$ for a NFL [27]. B defines the strength of electron-electron scattering. The fit of the data is shown in Figure 4.3 as solid lines. The results are tabulated in Table 4.3.

Table 4.3 Parameter obtained from fit of high-temperature resistivity data to equation 4.3

Sample	m	ρ_{sat} (Ω-cm)	ρ_0 (mΩ-cm)
NLNO/LAO	1.43 ± 0.10	0.060 ± 0.01	3.22 ± 0.03
NLNO/STO	2.14 ± 0.01	0.086 ± 0.01	55.02 ± 0.19
NLNO/NGO	2.01 ± 0.06	0.029 ± 0.02	9.80 ± 0.27

It can be seen that the films with tensile strain have $m \approx 2$. However, for the film NLNO/LAO, $m \approx 1.43$, which is close to $m = \frac{5}{3}$. The observed behavior in NLNO/LAO is in conformity with the observations and proposed strain-driven phase diagram for NNO [27].The observed ρ_{sat} in the NLNO/STO and NLNO/LAO films are similar in order, while in NLNO/NGO, it is somewhat smaller although of the same order. ρ_{sat} is proportional to the inter-band spacing, which arises due to the formation of conducting channel because of inter-band scattering [27].Typical values for Mott-Ioffe-Regel limit (ρ_{MIR}) for nickelates is 0.2-0.3 mΩ-cm [27, 28]. All the films here show $\rho_{sat} > \rho_{MIR}$ suggesting bad metallic nature of films. The value of ρ_0 seems to depend on the built-in strain. It is largest in the most strained film NLNO/STO. For the films NLNO/STO and NLNO/LAO, the observed ρ_0 from the high-temperature fit is very close to $\frac{1}{\sigma_0}$ obtained from the conductivity data below 2 K (see Table 4.2). Interestingly, due to the large temperature variation of σ in NLNO/NGO, $\rho_0 \ll \frac{1}{\sigma_0}$.

4.4. How good are the metallic states?

All three films show metallic behavior at high temperature ($T > T^*$), but they have different resistivity. The film NLNO/NGO shows a very low conducting (highly resistive) state below T^*. We ask the question of whether we observe an anomaly in the DOS at Fermi level $E_F(N(E_F))$. We obtained a measure of $N(E_F)$ from the tunneling conductance data $g(V)$ measured as a function of bias V applied to film as the tip was grounded with respect to the film. The $g - V$ data for the films at room temperature and 120 K are shown in Figure 4.6. For all the films, the tunneling conductance $g(V)$ has a parabolic dependence on bias V, as expected for tunneling of electrons between two metal electrodes (tip and the film) through the symmetric trapezoidal barrier. Any

asymmetry in the trapezoidal barrier would lead to an offset (V') from parabolic behavior at low bias [29]. Due to the asymmetric nature of the $g - V$ curve, the tunneling data are fitted to the parabolic equation that incorporates V' [29]:

$$g(V) = \alpha + 3\gamma(V - V')^2 \tag{4.4}$$

where α is a measure of DOS, γ is related to mean barrier height and V' is the offset from parabolic behavior due to the asymmetric trapezoidal barrier. The quadratic term contains a term V' that accounts for any small shift of the minimum of $g(V)$ from the origin. The fit to the data are shown as solid lines and the parameters α, γ, V' are obtained. The values of V' as obtained from the fit (shown in Figure 4.7 (b)) is small and negative. Deviation from parabolic tunneling equation (equation 4.4) can occur if applied bias is comparable to the work function leading to a departure from the trapezoidal barrier and also if the bands from which electrons tunnel are narrow (d-bands) so that assumption of a flat DOS cannot be made.

In oxides like NNO, the d band (hybridized with Ni^{3+} orbitals) has a width of ~1 eV. The tunneling conductance has been measured with a bias V < 0.2eV. At this small bias deviation from parabolic tunneling, the equation is not expected. Since α is a measure of $N(E_F)$, $\frac{\alpha(T)}{\alpha_{293}}$ as a function of T would measure the temperature variation of $N(E_F)$. Data for the three films are shown in Figure 4.7 (a).

Note: To rule out the possibility of the offset coming from broadband noise or offset in preamplifier gain of the STM unit, we have recorded the I-V characteristics of an artificial tunneling simulator (Resistance 100 MΩ) in a narrow voltage range (± 50 mV). No offset in the voltage has been observed. The detailed measurement circuit is given in the experimental section of chapter 2.

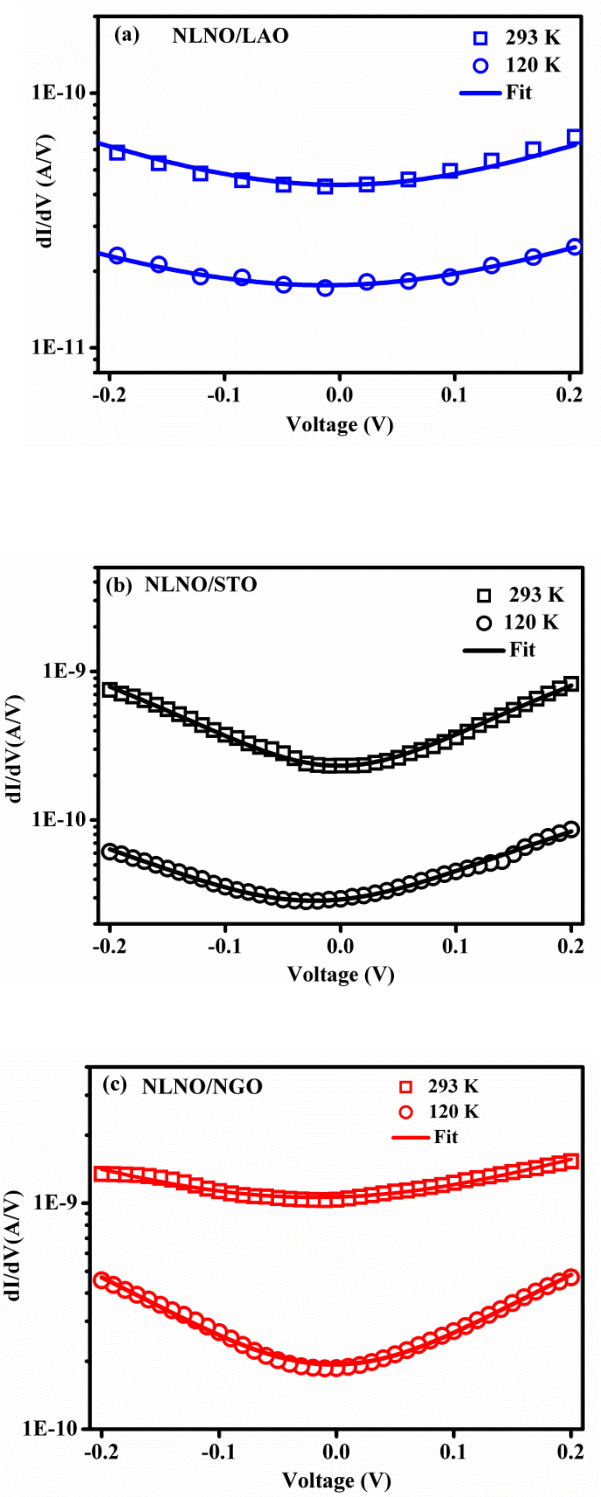

Figure 4.6 $g = \frac{dI}{dV}$ as a function of bias voltage V at 120 K and 293 K for the three NLNO films. The lines through the data are fit to equation 4.4.

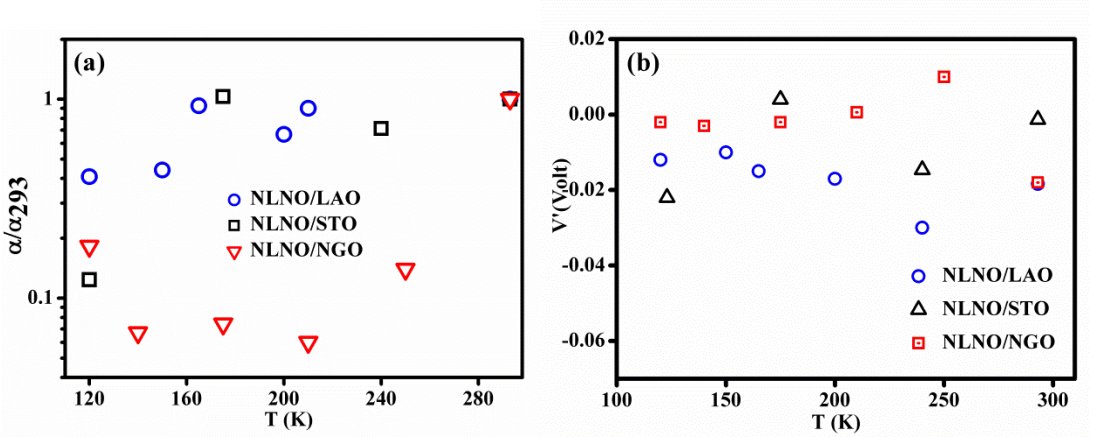

Figure 4.7 (a) $\frac{\alpha(T)}{\alpha_{293}}$ as a function of temperature for the three NLNO films and (b)The variation of V' as a function of T in all the films. The magnitude of V' is less than 20 meV.

For the NLNO/LAO, $N(E_F)$ is more or less temperature independent as it should be in metal, barring a steep decrease at around 150 K. For NLNO/STO, which has a distinct T* the $N(E_F)$ shows a drop below 150 K as well. Interestingly, the temperature range is close to the temperature T*. In NLNO/NGO, which lies closest to the MIT boundary, there is a large drop in $N(E_F)$ on cooling even in a state where the resistivity shows PTC. In a strongly correlated metal, it has been shown that due to electron-electron correlation the DOS can be depressed close to the Fermi energy E_F and it also has a temperature dependence where the depression close to E_F enhances on cooling [13]. The tunneling conductance data thus establish that the NLNO/NGO differs strongly from a conventional metal due to strong correlation.

4.5 Effect of disorder: Magnetoconductance at low temperature (T < 2 K)

In this section, we discuss the magnetoconductance in all the films as it is a potent tool to study MIT and electron localization. Two factors with opposite signs can contribute to the magnetoconductance (MC) close to MIT. The quantum interference (QI) arising due to backscattering in a disordered metal leads to weak localization (WL). QI is suppressed in an applied magnetic field due to lack of time-reversal symmetry. This leads to a positive MC (This we refer as WL contribution) [30]. The other contribution arises from localized spins. Near the MIT, localization of electrons leads to the formation of localized spins at energies close to the Fermi level [25, 31, 32]. The localized spins can lead to weak magnetism and can also participate

in electron scattering, giving rise to negative MC. Since the contribution comes from the exchange-correlation of spins at a different site, we refer to this contribution as EC.

The films studied being close to the transition region (at least 2 of them), the MC is expected to have comparable contributions from both the effects. These two contributions will add-up and would give rise to a non-trivial dependence of MC on the applied magnetic field (H). Since direct measurement of weak magnetic moments through magnetic measurements (like magnetization) in such films become difficult, the MC measurements give us an alternate way to gain information of the existence of spins in such films. The MC data are shown in Figure 4.8 at 0.3 K and 1.8 K in all the three films. The magnitudes of the MCs are small and they decrease rapidly above 2 K. At 0.3 K at a field of 8 T (data not shown), the maximum MCs observed are 1.1 %, 3.9 % and 8.0 % in the films NLNO/LAO, NLNO/STO, and NLNO/NGO respectively. In all the films, at T = 5 K, $\frac{\Delta\sigma}{\sigma} \leq 0.1\%$. For this reason, the data analysis is restricted in the temperature range below 2 K.

In general, the contribution of WL to MC ($\frac{\Delta\sigma}{\sigma}$) has a characteristic dependence $\sim\sqrt{H}$ [37, 40]. The EC contribution to MC is given by the phenomenological relation:$\frac{\Delta\sigma}{\sigma}(H) = -A * \frac{H^2}{H^2+(H_e^2)}$, where H_e is field required for spin alignment [31-32]. For$H \gg H_e$, $\frac{\Delta\sigma}{\sigma}(H)$ saturates. At low field ($H \ll H_e$), $\frac{\Delta\sigma}{\sigma}(H) \sim H^2$.

Assuming that the MC contributions are additive, the MC is fitted to the relation below:

$$\frac{\Delta\sigma}{\sigma}(H) = -A(T) * \frac{H^2}{H^2+(H_e^2)} + B(T)\sqrt{H} \qquad (4.5)$$

where *A(T)* and *B(T)* is temperature dependent but field independent constants.

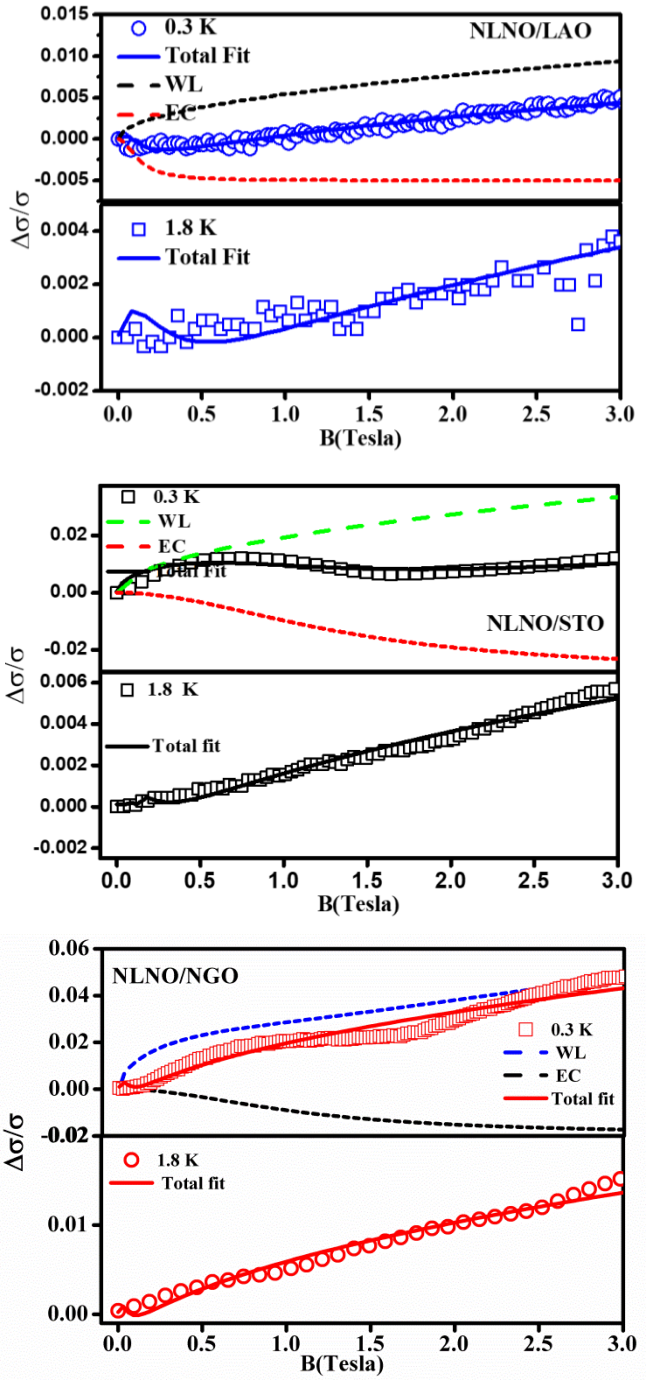

Figure 4.8 Magnetoconductance data for all the films at 0.3 K, and 1.8 K. The solid lines through the data are the fit to equation 4.5. Individual contributions are shown by dotted lines.

In Figure 4.8, the two contributions are shown separately. The coefficients *A* and *B* decrease on heating (Table 4.4) leading to weakening of MC on heating. In the case of WL, enhanced temperature leads to enhanced thermal de-phasing and the field-induced suppression of WL

becomes less effective. This also happens with the negative MC contribution because the ground state spin population decreases at a higher temperature.

The values of MCs have a small dependence on the direction of field scans (field- up or field-down scans) in films NLNO/ STO and NLNO/NGO. It is likely that the spins get aligned by the random anisotropy field leading to hysteresis in MC for the field scan-up and scan-down. In order to keep the state of the film unaffected by the history of the applied field, the data shown are for field scan-up direction only. The values of H_e are ~ 0.4 T, 0.05 T and 0.17 T for NLNO/LAO, NLNO/NGO and NLNO/STO respectively. In all the three films, the values of H_e are temperature independent which strongly suggest that H_e may arise from local anisotropy like a random field. The values for the coefficient *A* for the films on NLNO/LAO and NLNO/STO are low. However, for the film NLNO/NGO which is on the verge of becoming insulating, the coefficient *A* is much larger. Stronger localization of electrons in NLNO/NGO leads to enhanced effects from localized spins.

Table 4.4 Fitting parameter A and B obtained from fitting data to equation 4.5 for the films for field scan-up H (0-3T).

T(K)	(NLNO/LAO)		(NLNO/STO)		(NLNO/NGO)	
	A	B	A	B	A	B
0.3	0.005	0.005	0.0028	0.015	0.012	0.033
1.8	0.0047	0.004	0.0015	0.005	0.004	0.010

4.6 Discussion

The main results obtained in this chapter establish that the resistivity upturns in films NLNO/STO and NLNO/NGO below the temperature T^* do not mean entry into an insulating state, rather there is an entry into a metallic phase with NTC but a finite $\sigma_0 \ll \sigma_{Mott}$. The results also establish that even with the same value of $x \approx 0.3$ in NLNO the limiting resistivity at $T \to 0$, can be tuned by a factor of nearly 40 by changing the strain, substrate symmetry, and the orientation of the films grown. In particular, the presence of orthorhombic distortion (as in the film NLNO/NGO) appears to have a strong effect that it almost drives the film to a critical region of MIT. The observed MIT has the features of an Anderson transition (continuous transition) in contrast to first-order Mott type transition seen in NNO. The La substitution in NNO close to the critical composition thus

changes the nature of the transition. The T_{MI}, in this case, turns into a cross-over temperature that marks the change from a PTC region to an NTC region. Theoretical investigations on the half-filled Anderson Hubbard model have shown that the resistivity scaling strongly depends on the strength of interaction and disorder [14]. Also, the quantum corrections to conductivity at lower temperature have been seen in disordered $LaNiO_3$ system and modeled as electron-electron interaction and 3-D weak localization [10].

In the three films we have studied, the effect of strain, as well as substrate symmetry, play a dominant role in deciding the nature of the low-temperature transport. The higher value of ρ_{sat} in NLNO/STO compared to that of ρ_{sat} in NLNO/NGO can be understood in terms of strain-induced e_g orbital splitting [27]. Table 4.1 shows the magnitude of strain is highest for NLNO/STO. Higher tensile strain in the film NLNO/STO leads to higher ρ_{sat} while it is independent of the disorder. If the magnitude of strain is solely responsible for T^*, one would expect higher T^* for NLNO/STO. However, the cross-over temperature is less than that of the NLNO/NGO. Interestingly, due to higher T^* in NLNO/NGO films, its resistance starts to rise in this film much faster than that of NLNO/STO films when cooled to lower temperatures and eventually in NLNO/NGO the conductivity σ_0 becomes lower than that of NLNO/STO by a factor of nearly 1.7.

Recent work on the $NdNiO_3$ films grown on NGO, Lanthanum aluminate-strontium aluminum tantalite (LSAT) and LAO substrates, which possess orthorhombic, cubic and rhombohedral symmetries respectively show that the transport properties change drastically and depend on the tilting pattern of oxygen octahedra at film/substrate interface. It has been suggested by imposing the specific tilts of oxygen octahedra using NGO (111) substrate, the MIT can be pushed to 335 K [33,34]. Thus the unconventional direction of substrate used for growing nickelates film changes the transition temperature dramatically. The existence of higher T^* in NLNO/NGO likely happens due to substrate-induced lattice orthorhombic distortion which is consistent with the earlier results on $NdNiO_3$ [17]. In our case, the (110) direction of NLNO/STO allows the in-plane lattice parameters to get fixed with the substrate, Koster et. al suggested for such cases the NiO_6 octahedra can rotate freely in the in-plane direction and the rotation follows a Glazer tilt ($a^+a^-c^0$) [19-20]. In that case, the orthorhombicity, $\frac{a}{b} \rightarrow 1$, while for the film NLNO/NGO with growth direction (100), the "b" parameter is fixed to the substrate (5.50 angstrom) and out of the plane "a" can be measured from XRD (5.32 angstrom). For this film $\frac{a}{b} = 0.976$, lower $\frac{a}{b}$ means more orthorhombic distortion. It is thus clear that the substrate induced orthorhombic distortion makes the T^* higher

for NLNO/NGO. Note: While preparing this thesis we came across a recent thesis by Jennifer Fowlie, where an unusual discontinuity in T_{MI} has been observed near x = 0.2 for $Nd_{1-x}La_xNiO_3$ solid solution, and this composition was identified as an onset for first-order phase transition [35].

The observed MCs in NLNO films though very small have distinct behavior that has not been observed before in nickelates. The MC shows a contribution from the weak localization and contribution arises from the formation of local moments at energies close to the E_F at the approach of MIT. The two contributions add up and give the non-trivial temperature dependence of the MC. Both the components are enhanced as σ_0 decreases and MIT is approached. The appearance of local moments close to the critical region is an important hallmark of Anderson Transition [25]. The MC result thus reinforces the inference that the substitution leads to a regime of Anderson type transition.

The results presented in this chapter show that transport properties have dominant contributions from strain, as well as substrate lattice symmetry. The strain is responsible for tuning the transition from compressive (NLNO/LAO) to tensile strain (NLNO/STO or NLNO/NGO) but the substrate symmetry and orientation plays an important role in the case where transport is investigated on films experiencing tensile strain (NLNO/STO and NLNO/NGO in this case). This, however, masks any systematic dependence on the disorder. Nevertheless, there exists a role of disorder in the films.

4.7 Conclusion

In this chapter, we show that the first order MIT (like a Mott transition) in $NdNiO_3$ changes its nature when Nd is substituted by La close to the critical region of a composition driven MIT as in an Anderson type transition. The distinct T_{MI} changes to a cross-over temperature T^* that marks a change from a PTC of resistivity at $T^* > T$ to NTC of resistivity at a lower temperature. The transition can be further tuned by a combination of factors like strain, substrate symmetry, and quenched disorder. Probes like structural study and introduction of controlled disorder would help further the scientific community to understand the detailed underlying mechanism of such a phenomenon. A further detailed crystallographic analysis is necessary to understand the effect of strain and lattice symmetry on the NiO_6 octahedra in NLNO films. Also, introducing the disorder in a controlled manner retaining other factors unchanged would clarify the role of disorder in MIT of such systems (In the chapter 6 we extend our investigation in this context and discuss the role of disorder in the context of MIT).

Bibliography for Chapter 4

1. A. Möbius, Critical Reviews in Solid State and Materials Sciences 0 1-55 (2017).
2. A. K. Raychaudhuri, Adv. Phys.44 21 (2006).
3. K. P. Rajeev and A. K. Raychaudhuri, Phys. Rev. B 46 1309 (1992).
4. A. K. Raychaudhuri, K. P. Rajeev, H. Srikanth, and R. Mahendiran, Physica B 197 124-132 (1994).
5. N. F. Mott, (Taylor & Francis, London) (1990).
6. M. Imada, A. Fujimori, and Y. Tokura, Rev. Mod. Phys. 70 1039 (1998).
7. A. S. Disa, D. P. Kumah, J. H. Ngai, E. D. Specht, D. A. Arena, F. J. Walker, and C. H. Ahn, APL Mater.1 032110 (2013).
8. J. Son J, P. Moetakef, J. M. LeBeau, D. Ouellette, L. Balents, J. S. Allen, and S. Stemmer, Appl. Phys. Lett. 96 062114 (2010).
9. K. P. Rajeev, G. V. Shivashankar, and A. K. Raychaudhuri, Solid State Commun.79 591 (1991).
10. E. J. Moon, B. A. Gray, M. Kareev, J. Liu, S. G. Altendorf, F. Strigari, L. H. Tjeng, J. W. Freeland, and J. Chakhalian, New J Phys 13 073037 (2011).
11. G. Herranz, B. Martinez, J. Fontcuberta, F. Sanchez, C. Ferrater, M. V. Garcia-Cuenca, and M. Varela, Phys. Rev. B 67 174423 (2003).
12. Y. G. Sh, Y. F. Guo, S. Yu, M. Arai, A. Belik, A. Sato, K. Yamaura, E. Takayama-Muromachi, H. F. Tian, H. X. Yang, J. Q. Li, T. Varga, J. F. Mitchell, and S. Okamoto, Phys. Rev. B 80 161104 (2009).
13. A. L. Efros, M. Pollak, Electron-Electron interaction in disordered systems (1985).
14. N. D. Patel, A. Mukherjee, N. Kaushal, A. Moreo, and E. Dagotto, Phys. Rev. Lett. 119 086601 (2017).
15. W. S. Oliveira, M. C. O. Aguiar, and V. Dobrosavljevic, Phys. Rev. B 89 165138 (2014).
16. J. Blasco and J. Garcia, J. Phys.: Condens. Matter 6 10759-10772 (1994).
17. X. K. Lian, F. Chen, X. L. Tan, P. F. Chen, L. F. Wang, G. Y. Gao, S. W. Jin, and W. B. Wu, Appl. Phys. Lett. 103 172110 (2013).
18. R. Scherwitzl, Metal-insulator transitions in nickelate heterostructures, Ph.D. thesis, University of Geneva (2012).

19. A. Vailionis, H. Boschker, W. Siemons, E. P. Houwman, D. H. A. Blank, G. Rijnders, and G. Koster, Phys. Rev. B 83, 064101 (2011).
20. A. Vailionis, W. Siemons, and G. Koster, Appl. Phys. Lett. 93, 051909 (2008).
21. Y. Kumar, R. J. Choudhary, S. K. Sharma, M. Knobel, and R. Kumar, Appl. Phys. Lett. 101 132101 (2012).
22. R. D. Shannon, ActaCryst. A **32**(5) 751 (1976).
23. W. N. Shafarman, D. W. Koon, and T. G. Castner, Phys. Rev. B 40 1216 (1989).
24. N. F. Mott and M. Kaveh, Philosophical Magazine B 47 577-603 (1983).
25. P. A. Lee and T. V. Ramakrishnan, Rev. Mod. Phys.57 287 (1985).
26. E. Gati, U. Tutsch, A. Naji, M. Garst, S. Köhler, H. Schubert, T. Sasaki, and M. Lang, Crystals 8 38 (2018).
27. E. Mikheev, A. J. Hauser, B. Himmetoglu, N. E. Moreno, A. Janotti, C. G. Van de Walle, and S. Stemmer, Sci. Adv. 1 e1500797 (2015).
28. S. Das, V. E. Phanindra, S. S. Philip, and D. S. Rana, Phys. Rev. B 96 144411 (2017).
29. E. L. Wolf, 1989 (Oxford University Press).
30. A. Kawabata, J. Phys. Soc. Jpn. 49 628 (1980).
31. A. Frydman and Z. Ovadyahu, Solid State Commun. 94 745 (1995).
32. A. Vaknin, A. Frydman, Z. Ovadyahu, and M. Pollak, Phys. Rev. B 54 13604 (1996).
33. S. Catalano, M. Gibert, J. Fowlie, J. Iniguez, J. M. Triscone, and J. Kreise, Rep. Prog. Phys. 81 046501, (2018).
34. S. Catalano, M. Gibert, V. Bisogni, F. He, R. Sutarto, M. Viret, P. Zubko, R. Scherwitzl, G. A. Sawatzky, T. Schmitt, and J.-M. Triscone, APL MATERIALS 3, 062506 (2015)
35. Jennifer Fowlie, Electronic and Structural Properties of $LaNiO_3$ Based Heterostructures, Doctoral Thesis accepted by the University of Geneva.

Chapter 5 Electroresistance in $NdNiO_3$ films

In this chapter, we discuss the electroresistance effect observed in the $NdNiO_3$ film grown on the $SrTiO_3$ (111) single crystal substrate using pulsed laser deposition. The film shows a metal-insulator transition near 220 K. The resistivity measurement down to 10 K at different current shows suppression of resistivity by nearly an order without affecting the metal-insulator transition temperature. To rule out the possibility of such suppression in resistivity due to Joule heating, we have performed current-induced resistivity switching measurement which shows a transient behavior of the resistance. In addition to that, the continuous I-V and pulsed I-V measurements show the absence of Joule heating contribution below a certain current (1.8 mA). Even at highest current bias, the maximum temperature rise is 12 K, which is insufficient for such a change in resistivity by an order. The results thus suggest that the observed effects are due to the intrinsic electroresistance effect in the $NdNiO_3$ film. We discuss a certain scenario of the phase co-existence of the high temperature metallic and low-temperature insulating filaments that may lead to this observation.

5.1 Introduction

As discussed in earlier chapters also, the metal-insulator transition (MIT) in rare-earth nickelates can be modulated widely using a number of physical parameters like substrate-induced strain, electric field controlled strain, lattice symmetry, etc [1-7]. In rare-earth manganites like $LaMnO_3$ as well as in hole-doped La-Ca/Sr-Mn-O systems, colossal electroresistance effects have been observed and reported by a number of authors [8-15]. Further, it has been shown that in some cases the metal-insulator transition temperature (T_{MI}) can be modulated by the current bias while for some of the cases the T_{MI} remains unaffected [12]. The different literature existed in this context have a different interpretation. Whereas, the exact interpretation of such results is still debatable. In many cases, it has been understood as a consequence due to the ion ionization mechanism, hot electron theory, and co-existence of different phases [8-15]. However, for most of the cases, the melting of charge ordering state was accounted for the suppression of resistivity nevertheless the phase co-existence of ferromagnetic metal and the antiferromagnetic insulator also plays an important role [12].

Observation of colossal electroresistance motivated us to look into the electroresistance study of the nickelates $NdNiO_3$. Not withstanding the differences of $NdNiO_3$ and $LaMnO_3$ in terms of basic physics of the insulating state, it is felt that destabilizing the MIT in $NdNiO_3$ by a current/electric field will lead to new phenomenology that has not been yet investigated in the nickelates. Though it's debatable, the insulating state of the nickelates is interpreted as a charge ordering state. It will be tempting to see how electric current acts on charge order state in the nickelates. Yet another reason to look into the electroresistance phenomenon is the phase co-existence of the high temperature paramagnetic metallic state and the low temperature antiferromagnetic insulating state in $NdNiO_3$ system [16].

In this study, we have grown the $NdNiO_3$ film on different $SrTiO_3$ single crystal orientation of (100) and (111). In both the films, we have seen suppression of resistivity on the application of the current bias without affecting the $T_{MI.}$ We report the detailed results on film that is grown on (111) orientation of $SrTiO_3$ single crystal substrate [17, 18]. To understand the electroresistance in this film we have also studied the current induced resistive switching using a two-level pulse train measurement. To avoid the Joule heating phenomenon we have also incorporated the pulsed I-V technique that mitigates the Joule heating contribution. In the pulsed I-V technique, during the off

state of the pulse, the dissipated power will drain out of the system to the Cu base that mounts the sample through the intervening Ge Varnish and N grease interfaces [19, 20]. This will lead to cooling down of the film. I-V, Pulsed I-V and current-induced resistive switching data were taken in 2 probe configuration (between probe 1 and 3).

5.2 Resistivity as a function of temperature at different current

The films were deposited by the pulsed laser deposition (PLD) technique as described in chapter 2. The reciprocal space mapping (RSM) shows that the film is highly oriented in the (111) direction of the substrate. The pseudocubic (103) Bragg spot further suggests that the films are partially strained relaxed. The 3 μm atomic force microscope (AFM) micrograph shows the surface roughness of the film is nearly 0.44 nm. In Figure 5, we present the results of RSM and AFM.

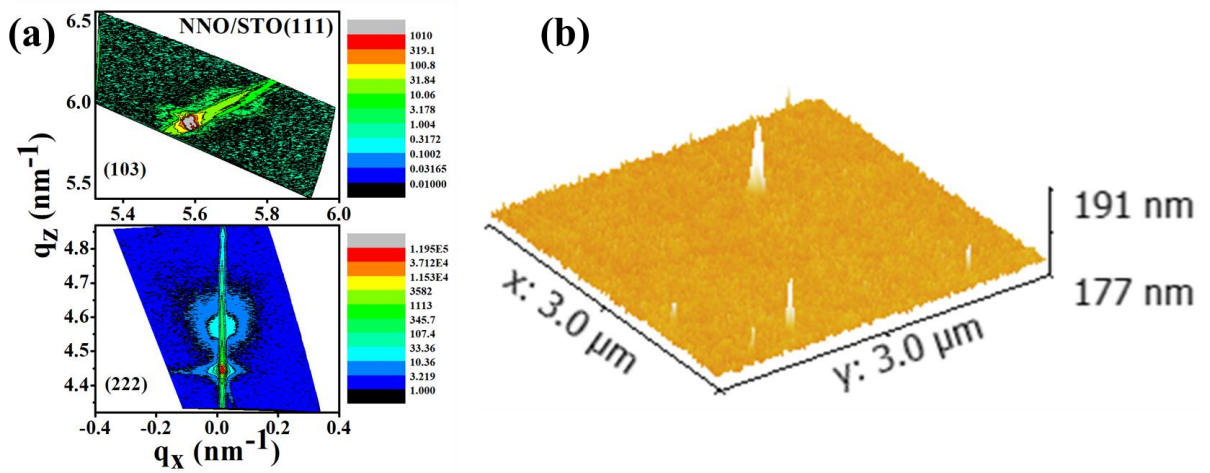

Figure 5 (a) The reciprocal space mapping (RSM) and (b) the AFM image of the $NdNiO_3$ film grown on $SrTiO_3$ (111) single crystal substrate.

The resistivity as a function of temperature at different current was taken in a collinear four-probe configuration down to 10 K. The initial current range used for the resistivity measurement was from 1 μA to 5 mA. The upturn in resistivity as well as the change in the slope of $\frac{d\rho}{dT}$ was identified as the metal-insulator transition temperature (T_{MI}). For the films used in the experiment the T_{MI} was observed at 220 K as can be seen from Figures 5.1(a) and (b), in particular, the inset of Figure 5.1 (b) where we have plotted the zoomed version near the transition region.

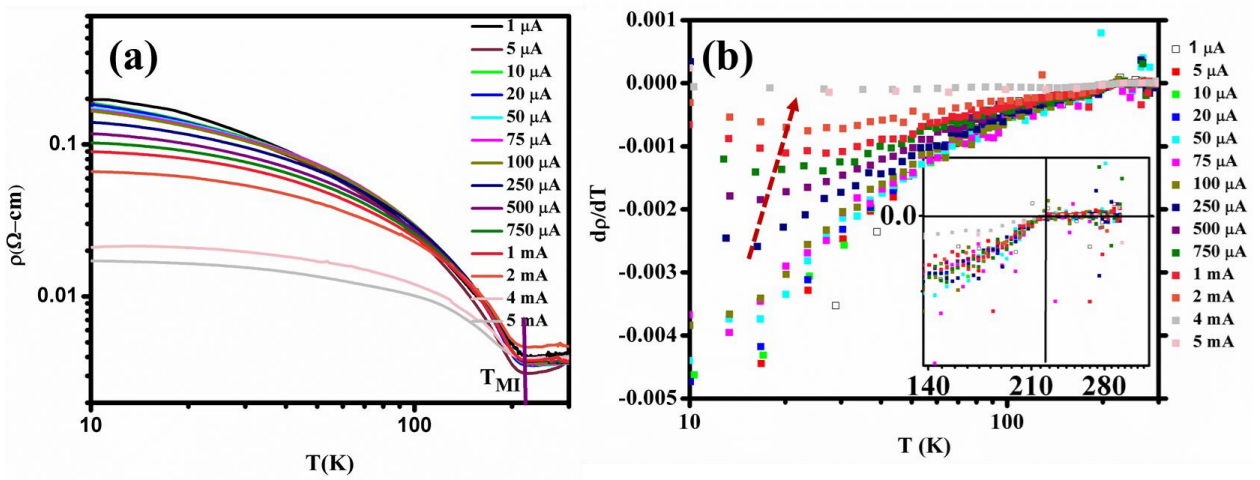

Figure 5.1 (a) The resistivity data as a function of temperature for different current bias and (b) corresponding $\frac{d\rho}{dT}$ for $NdNiO_3$ film grown on $SrTiO_3$ (111) single crystal substrate (Note the logarithmic scales). Inset shows the zoomed version of (b), around the transition region. T_{MI} identified as the crossing of two lines viz. change in slope.

The resistivity plot shows a very important result that there is no change in the T_{MI} on changing the current bias as shown in Figure 5.1 (a). The data $\rho - T$ as well $\frac{d\rho}{dT} - T$ both shows no change in T_{MI} but there are changes in resistivity. To accentuate the changes more and to identify the T_{MI}, we have plotted the zoomed version of the $\frac{d\rho}{dT}$ on a smaller scale. The data thus shows that T_{MI} is unaffected by the current bias. Further, it shows that the softening of $\frac{d\rho}{dT}$ in temperature dependence, as can be seen in Figure 5.1 (b). The onset of softening moves to higher values with higher current and $\frac{d\rho}{dT} \rightarrow 0$ at the highest measurement current.

Figure 5.1 (a) also shows a monotonous decrease in resistivity below T_{MI} on the application of high current bias. Figure 5.2 shows that contour plot of the resistivity as a function of temperature at different current bias. The resistivity data reflects a change in the resistivity by a factor of nearly 90 % on application of highest and lowest current (1μA and 5 mA) at 10 K. This suggests that the observed suppression of resistivity on the application of high current is due to the electroresistance effect. The electroresistance was calculated as

$$\text{ER (\%)} = \frac{R(I_{high}) - R(I_{low})}{R(I_{low})} \times 100 \qquad (5.1)$$

and plotted as |ER| as a function of temperature. In Figure 5.3 (a), we show the electroresistance calculated from the resistivity data for I_{high} (5 mA) and I_{low} (1µA) as shown in Figure 5.1 (a). An enormous change in the electroresistance has been observed.

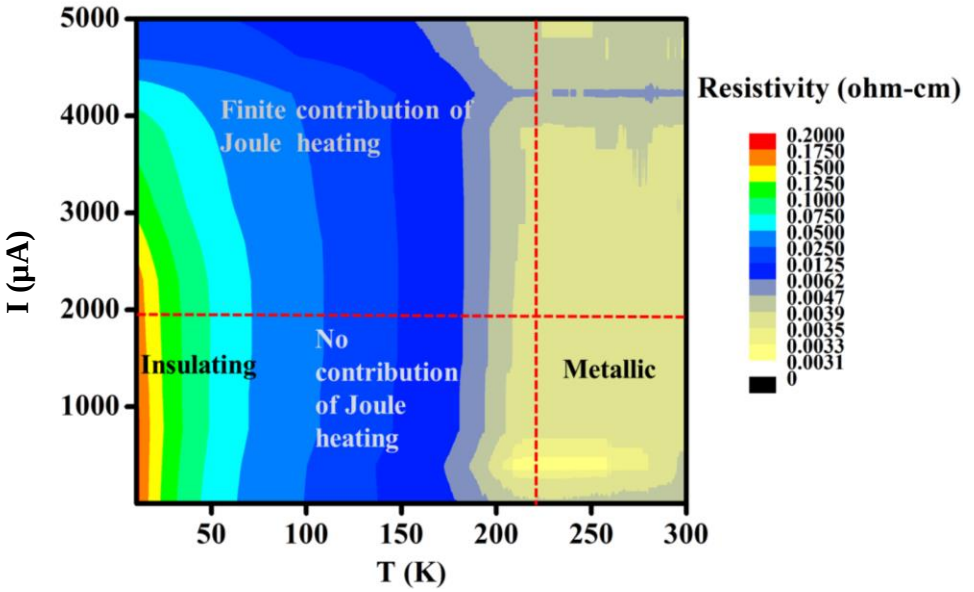

Figure 5.2 Contour plot of the temperature for $NdNiO_3$ film grown on $SrTiO_3$ (111) single crystal substrate at different current bias.

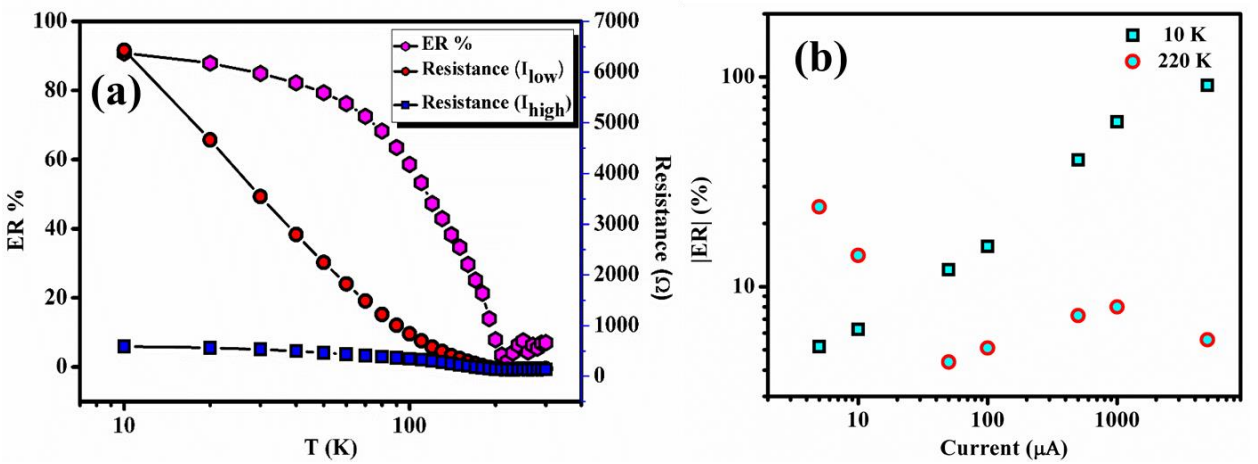

Figure 5.3 (a) The resistivity data for the lowest and highest current and electroresistance as a function of temperature for $NdNiO_3$ film grown on $SrTiO_3$ (111) single crystal substrate and (b) Electroresistance as a function of current bias at 10 K and 220 K respectively.

Below the MIT, particularly at lower T, the electroresistance is substantial and increases with the bias current. In contrast, the effect is small at the MI transition temperature and does not have a clear dependence on the current bias. This is shown in Figure 5.3 (b). Our results show that the T_{MI} remains unchanged even on the application of a high current bias of nearly 5 mA. In Appendix C (Figure C), we show that on the application of the high current bias, the suppression in the resistivity for $NdNiO_3$ film grown on $SrTiO_3$ (111) substrate without affecting the T_{MI} is consistent with the $NdNiO_3$ film grown on other orientation (100) of $SrTiO_3$ single crystal substrate.

For materials that show negative temperature coefficient of resistivity ($\frac{d\rho}{dT} < 0$) such a suppression of the resistivity can occur from Joule heating. We show below to what extent Joule heating affects the data and establish that a good part of the observed data is not a consequence of heating arising from Joule heating. In our experiment, a change in sample current from 5 mA to 1 µA changes the dissipated power by nearly 6 orders of magnitude from 15 mW to 6.75 nW at the lowest temperature measured 10 K. In conventional wisdom, such a significant change in the dissipating power may increase the temperature of the sample due to the Joule heating, which may also suppress the resistivity of the insulating state. Nevertheless, if these effects are intrinsic and are not an artifact due to the Joule heating, one would expect a current induced resistance switching in such systems similar to that observed in manganite systems [10,11]. In later sections, we will address these issues in details.

Briefly, one way to separate out the Joule heating effects is to use pulsed currents with small duty cycles (~20%) and in such cases, during the OFF period the film can cool down if there is any heating. If the data is now taken with different duty cycle the electro-resistance will become a function of the duty cycle. In the sections below we follow this procedure.

5.3 Current induced resistive switching

To understand the suppression of resistivity on the application of different current bias, we have adopted the pulsed current technique and measured the resistivity with a two-level current pulse as a function of time. This type of measurement is also called as the current induced resistivity switching in the literature [8, 10]. In Figure 5.4, we show the schematic of the current induced resistivity switching measurement on application of a two-level pulse train. The input current pulse after passing through the samples shows a transient response. In our measurements, the choices

of high and low current values were made from the I-V data (As shown in the next section). The choice has been made on the following consideration, (1). At such value of currents, the I-V data doesn't show any hysteresis effect. (2). The I-V is linear for the low current while it is non-linear for the high value of current. Thus taking the I-V data as a guide, we have fixed the minimum current (I_{min}) at 1µA and the maximum current (I_{max}) at 1.8 mA. In terms of power at the lowest T of 10 K, this leads to the power dissipation of nearly 10 mW.

Figure 5.4 Schematic of two-level current-induced resistivity switching.

The adoption of this technique further allows us to record the Joule heating also. In our C++ program for data acquisition, the switching time between high and low current pulses was set approximately 167 µs. The instant voltage response to the current pulse was measured with a sampling time of 20 ms and a precision of $5\frac{1}{2}$ digits resolution [21]. Importantly there was no filter used during the data acquisition as it would contribute a delay time to the measurements. The time constant of the RC circuit formed due to the samples resistance and cable capacitance (300 pF) and other spurious capacitance was nearly 4 order of magnitude less than the sampling time. In Figure 5.5, we see that the resistance of the sample changes reversibly on the application of the pulse train and is shown for four cycles.

Figure 5.5 further suggests that the resistance takes some time to reach a steady value. In our data acquisition program, we have used the ON/OFF states time such that for high as well as for the low pulse the resistance reaches a time independent steady value. As mentioned in the previous paragraph, the samples resistance value of nearly 14000 ohms and cable capacitance of 300 pF would lead to a time constant 4.2 µs, which is much smaller than the sampling time (20 ms) for the data collection. This suggests the resistance relaxation is an intrinsic effect associated with the sample and didn't arise due to an artifact from the instrument parameters [8]. In Figure 5.6 (a) and (b), we show the transient response on the application of the high and low current pulse. Such

transient response of resistivity has been observed for manganites. In the context of manganites, this transient nature of resistivity has been interpreted as a decoupling of electrons and phonons temperature [8, 10]. Whereas in the present case for nickelates we don't have an understanding of this transient nature of resistivity for the current induced resistive switching.

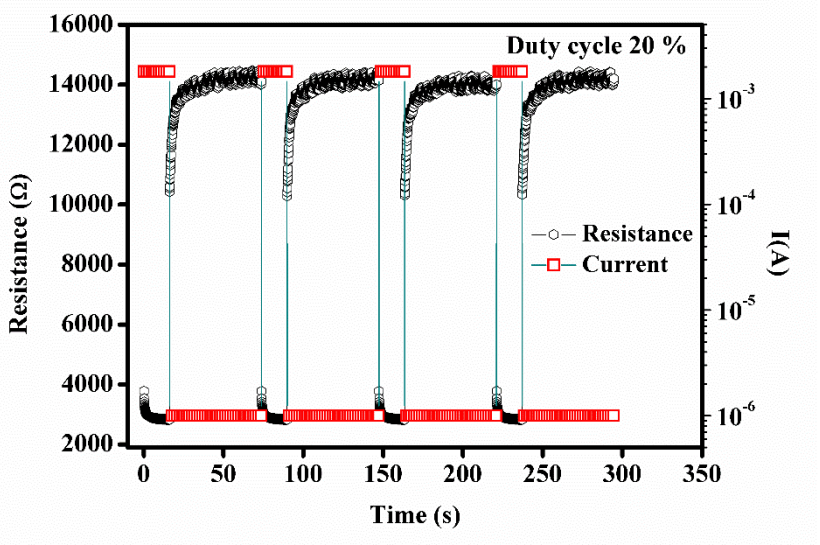

Figure 5.5 Current induced resistive switching for $NdNiO_3$ film between two current pulses of the magnitude I_{high} and I_{low}. Power dissipation at the lowest current and highest current is 14 nW and 10 mW respectively.

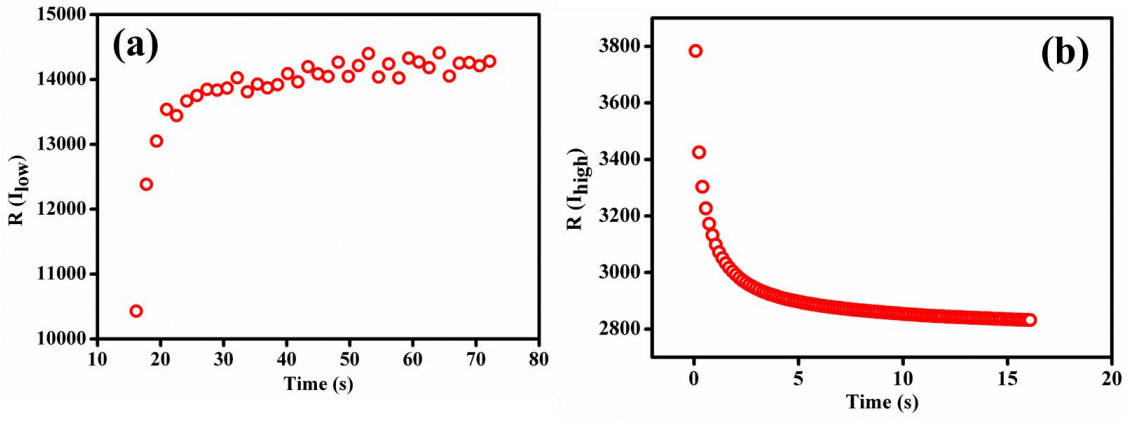

Figure 5.6 The resistance relaxation of $NdNiO_3$ film for two current pulses (a) I_{low} and (b) I_{high}.

5.4 Issue of Joule heating

It is important to understand whether this change in resistivity is due to the Joule heating or it is primarily due to the electroresistance effect. To capture the change in samples temperature due to

the joule heating, if any, we have followed the relation below to estimate the temperature rise due to Joule heating.

$$\Delta T = R_{th} Q' \qquad (5.2)$$

where ΔT is the temperature rise due to the power dissipation Q' in sample and R_{th} $(= \frac{x}{kA})$ is the total thermal boundary resistance calculated according to the geometry of sample mounting as shown in Figure 5.7(b), Here x is the thickness of the material, k is the thermal conductivity and A is the area. In our case, the total thermal boundary resistance can be written as $R_{th} = R_{STO} + R_{Ge\,Varnish} + R_{N\,Grease}$ and the modified relation for the temperature rise can be written as $\Delta T = (R_{STO} + R_{Ge\,Varnish} + R_{N\,Grease})\,Q'$. The thermal boundary resistance was calculated using the available data of thermal conductivity for GE varnish (Thickness ~ 0.1 mm, Area 10 mm^2), Apiezon N Grease (Thickness ~ 0.1 mm, Area 1 cm^2), and $SrTiO_3$ (Thickness ~ 0.5 mm, Area 10 mm^2) from manufacturers [23, 24] and the temperature-dependent value of k in the calculation for STO was used from reference 22. Due to the very low R_{th} of mica sheet (< 1 K/W), we have neglected its contribution in the calculation.

As discussed above, at 1 μA current the maximum power dissipated at 10 K is 6.75 nW, and it is insufficient for producing any Joule heating effect. Now if we assume that the entire suppression in the resistance for higher current is due to the Joule heating then one can write the dissipated power as $Q' = I^2 R_{T+\Delta T}$. According to this relation, the power dissipation for higher current can be written as

$$Q'(I) = I^2\,(R\,(1\mu A) + R\,(I)) \qquad (5.3)$$

where R (1μA) is the resistance corresponding to 1μA current and R (I) is the resistance corresponding to the current I. Below we show that the temperature rises at different bath temperature for 2 mA and 5 mA.

Table 5 Temperature rise (ΔT) due to the current bias at base temperature T calculated at two different current according to equation 5.2.

T (K)	ΔT (K) for 2 mA current bias	ΔT(K) at 5 mA current bias
10	12.91	65.10
100	0.36	1.68
300	0.04	0.23

Table 5 thus suggests the rise in samples temperature due to the Joule heating effect is maximum at 10 K. However at 2 mA or below, this temperature is insufficient to change the resistivity by one order. In various systems, it has been observed that joule heating may give rise to the non-linear conduction which may develop hysteresis also [12, 25]. Further, it is known that the I-V will follow a non-linear relation for an electroresistive material, we will see the non-linear behavior of the I-V curve in the upcoming section. In nanostructured $NdNiO_3$ this non-linear conductance below 2 K was described by the Landau Zener breakdown relation [26]. To understand the issue of Joule heating in our sample, we have performed the two probe I-V measurement at different temperature. We have employed two methods to take the I-V data. In the first method, we have swept the voltage continuously and measured the value of current, in the second method, we have changed the voltage in a pulse mode and measured the current (As shown in Figure 5.7 (a)).

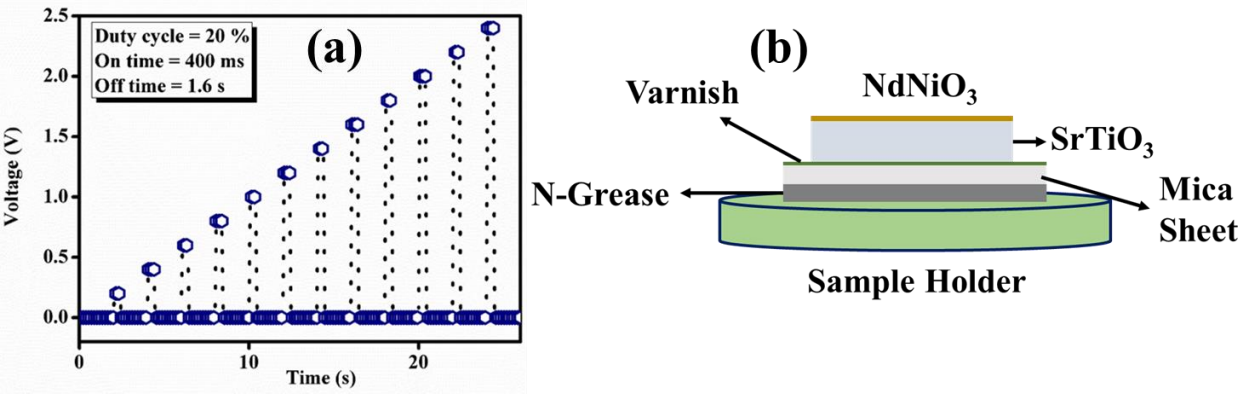

Figure 5.7 (a) The Pulsed Voltage as a function of time for the duty cycle 20 % and (b) Schematic of the thermal mounting of the sample.

The advantage of using pulsed voltage is that during the off state of the voltage pulse the associated power can be released to the metallic sample holder via Ge Varnish and N grease (Figure 5.7 (b) shows the thermal mounting of the sample). In Figure 5.8 (a) and (b), we show the continuous I-V as well as the pulsed I-V data taken at different temperature. As can be seen from the continuous I-V data, the I-V develops a hysteresis as the temperature decreases down to T_{MI}. Above the T_{MI} the I-V is more or less linear as expected for an ohmic system. Interestingly, the scale of hysteresis and the width of the hysteresis decreases significantly in the pulsed I-V data. This suggests above a critical current there is a Joule heating in the system. In Figure 5.8 (a) and (b) we have marked a critical current value of 1.8 mA (which we have used as an upper limit of the current pulse train in

the current induced resistance switching measurement as described in the previous section) below which all the hysteresis effects have diminished. This value of critical current does involve any hysteresis effect in both continuous and pulsed I-V data. In the temperature range above $T_{MI,}$ we have limited the voltage range up to 1 V to avoid unnecessary heating of the sample.

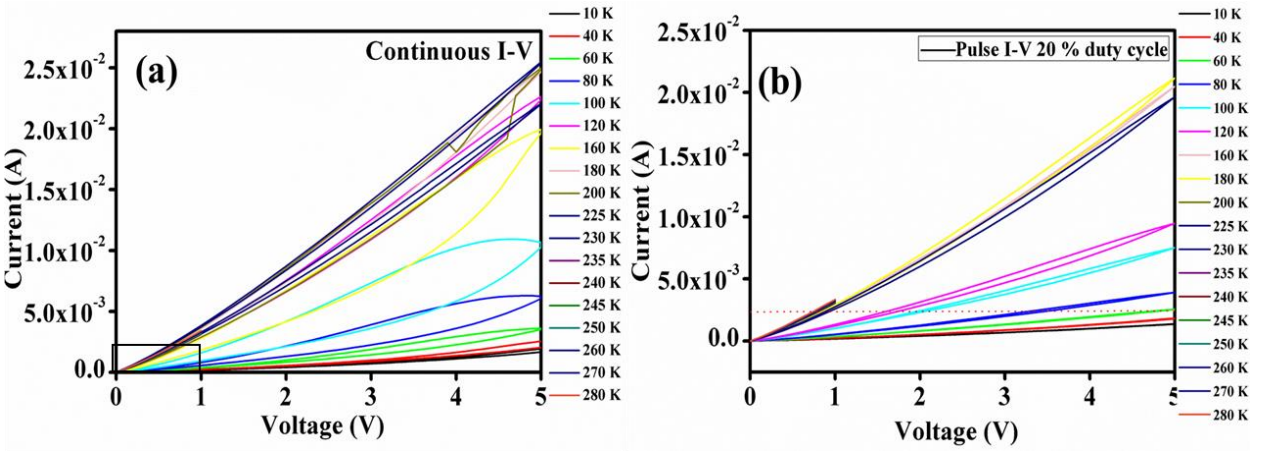

Figure 5.8 (a) The continuous I-V sweep at different temperature and (b) The Pulsed I-V for 20 % duty cycle voltage pulse at different temperature for $NdNiO_3$ film grown on $SrTiO_3$ (111) single crystal substrate.

Further, if there is any contribution from Joule heating in the resistivity data below 1.8 mA, it will reflect in the current induced resistance switching data on changing the on-time ($T(I_{high})$) for a current pulse. As increasing the on-time will dissipate more energy (E = I*V*t, where E, I, V and t represent the energy, current, voltage and on time respectively). To explore this, we have varied the duty cycle of the current pulse. In our measurement, we have fixed the off-time ($T(I_{low})$) for the current pulse and varied the $T(I_{high})$. In Figure 5.9, we have shown the electroresistance ER (%) = $\frac{R(I_{high})-R(I_{low})}{R(I_{low})} \times 100$, as a function of the duty cycle. The I_{low} and I_{high} were set as 1μA and 1.8 mA respectively. The time independent value of resistance was used in the calculation of electroresistance. Figure 5.9 shows that the electroresistance changes less than 2% as a function of the duty cycle at 10 K. This suggests that the electroresistance effect in the sample is the intrinsic property and there is merely any Joule heating in the sample at such measuring current. Thus, the I-V and the electroresistance measurement shows that the associated electroresistance is not associated with any joule heating.

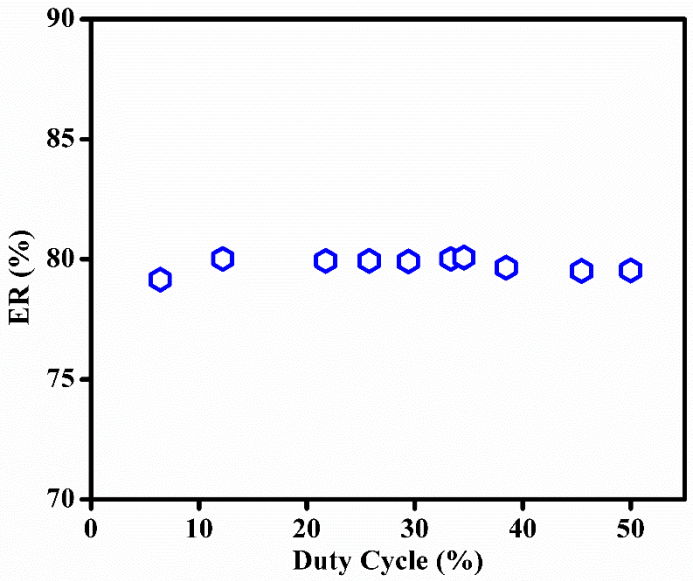

Figure 5.9 Electroresistance of $NdNiO_3$ film grown on $SrTiO_3$ (111) single crystal substrate as a function of the duty cycle at 10 K.

To further rule out the contribution of Joule heating, we perform further analysis using pulsed I-V data, in our sample, the associated Joule heating can be dissipated to the base of the sample via GE Varnish and N grease. In that case, one can write a heat balance equation as suggested by the Fursina and co-workers [27]:

$$C\frac{dT}{dt} = \frac{d}{dt}(Q_{in} + Q_{out}) \tag{5.4}$$

$$C\frac{dT}{dt} = IV - \frac{C(T-T_s)}{\tau} \tag{5.5}$$

Using, $\tau = R_{Th}C$ *and* $P = IV$, where τ, R_{Th}, T_s *and* C are the thermal relaxation, thermal boundary resistance, base temperature, and heat capacity respectively [27].

$$\frac{dT}{dt} = \frac{P}{C} - \frac{(T-T_s)}{\tau} \tag{5.6}$$

The solution of the equation 5.6 is given below [27]:

$$T(t) = T_s + \frac{P\times\tau}{C}\left(1 - \exp\left(\frac{-t}{\tau}\right)\right) \tag{5.7}$$

We have calculated the thermal relaxation time from Figure 5.6 (b) using the curve fitting of exponential decay function, R = R_0 exp $(\frac{-t}{\tau})$ +A, where A is the time independent resistance. Assuming the thermal relaxation is same in the present case as it has been calculated from current induce resistivity switching data. Now using the value of $\tau = 1.09$ s from the fit and the value of thermal boundary resistance as described in the previous section. The temperature rise during the

ON state of voltage was calculated according to equation 5.7. In Figure 5.10, we show that the maximum rise in the temperature from pulse I-V is nearly 4.2 K which is less than the value of ΔT (T- T_s) at 10 K from Table 5, as expected for pulse I-V characteristics.

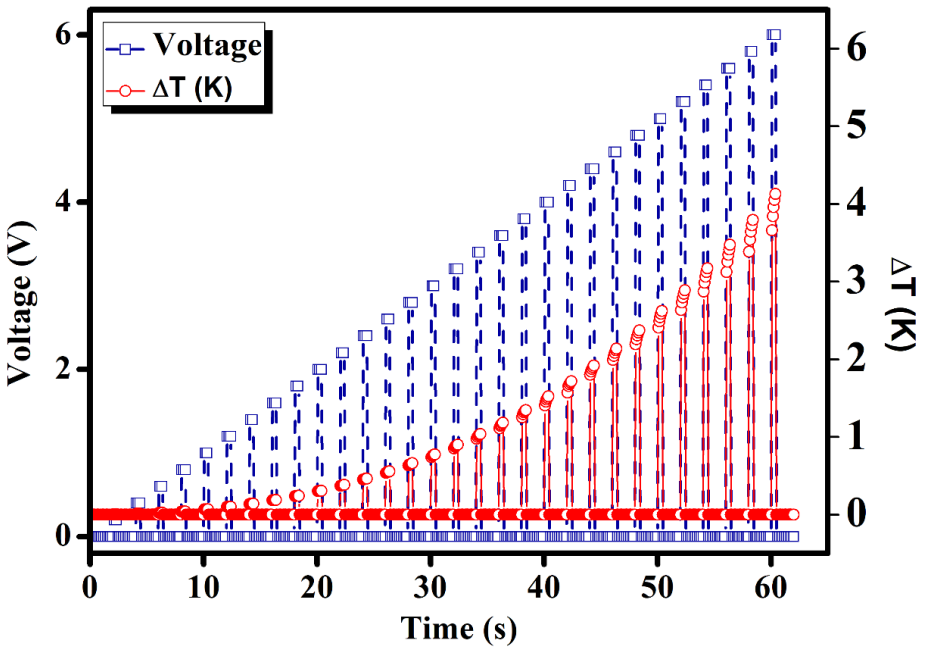

Figure 5.10 The rise in temperature as a function of time for different voltage pulse. The total temperature rise is nearly 4.2 K. The pulse data was taken for a 20 % duty cycle of the voltage pulse.

In this section, we show that the amount of temperature rise due to the Joule heating is very small (nearly 12 K) and such small rise in temperature is not sufficient to change the resistivity by an order or to change the T_{MI}. In the next section, we discuss certain scenarios which lead to such a phenomenon in nickelates.

Note: In conventional wisdom, the pulsed data should always lower the heating effect which we have also seen in this section. While the calculation is done from equation 5.2 uses a continuous current, the calculation done from equation 5.7 uses a pulsed I-V. This additionally suggests that Joule heating is unlikely a reason for the observed electroresistance effect below 1.8 mA.

5.5 Discussion

The previous report of such an observation in nickelates [28] has argued that the destruction of charge ordering state due to the dc current bias essentially changes nickel oxygen bond and further changes the tilt of NiO_6 octahedra environment which lead to suppression in the resistivity and change in T_{MI}. There is no other experiment in support of this hypothesis. In the context of nickelates, our results don't match with earlier results reported for the $Sm_{0.6}Nd_{0.4}NiO_3$ (SNNO) thin film grown on $LaAlO_3$. The results reported on SNNO show that the T_{MI} varies monotonically on the application of a high current density [28]. In contrast, the observation made by us has been seen for phase-separated manganites [29-32] where a large change in resistivity on the application of a high current density has been observed without affecting the T_{MI} [29-32]. In thin films of the nickelates, the T_{MI} and Neel temperature doesn't coincide with each other as seen for bulk. Even if the destruction of charge ordering is the reason for the observed electroresistance, the change in T_{MI} in reference 28 is still not understood. Further, the report shows that an increase in sample temperature by 40 K (as a consequence of Joule heating) which in our opinion can really suppress the resistivity by 4 times as reflected in the RT data provided by the authors. Thus the Joule heating is likely associated with the observed electroresistance in the past report [28].

In many cases it has been seen that the metal-insulator transition can be induced because of the Joule heating, such observations are reported by many authors for VO_2 thin films and even for manganites also [27,33,34]. It has been proposed in the context of manganites that the metal like region on the application of high current grows while an insulating phase shrinks. Similar results have been seen for the VO_2 film under applied bias. In most of manganites system, it has been argued due to the fact of co-existence of ferromagnetic metallic phase and antiferromagnetic insulating phase [29, 32]. In this scenario, nickelates show a transition from paramagnetic (metallic) to the antiferromagnetic (insulating) phase-transition. The antiferromagnetic state is a charge order state for the nickelates.

We link such results to the observation of phase co-existence present in the nickelates, which has been shown in chapter 3. The co-existence of the two phases can be really affected by the applied current. As it has seen that the electric field really affects the direction of the orbitals which is essentially an electron cloud [35]. Thus, the co-existence of the two phases will have a different response to the electric current [36]. The electric field hence may change the orbital occupancy

which may lead to the co-existence of phases and thus different conductivity on the different current bias. Near the MIT the population of metallic filament is large as compared to the insulating filaments even if there is weak phase separation. As the density of insulating filaments increases (on going to lower temperature), the current distribution would be non-uniform and may change the effective electron-electron interaction and may lead to suppression of resistivity without changing the T_{MI}. The suggestions made above are speculative and more definitive experiment that can capture the changes occurring within the film on the application of current are needed.

5.6 Conclusion

- The resistivity of the insulating region is highly suppressed in the application of different current bias without affecting the metal-insulator transition temperature.
- Joule heating is unlikely responsible for the observed effect below a certain bias current.
- The observed suppression in the resistivity without affecting the metal-insulator transition temperature was attributed due to the co-existence of high temperature metallic and low-temperature insulating phase.
- The bias dependent Raman spectroscopy at low temperature can give more insight into how the insulating fraction changes on the application of current bias. As expected the Raman modes associated with the monoclinic structure may diminish or may get weaken on the current bias.

Bibliography for Chapter 5

1. J. B. Torrance, P. Lacorre, A. I. Nazzal, E. J. Ansaldo, and Ch. Niedermayer, Phys. Rev. B **45**, 8209 (1992).
2. G. Catalan, Phase Trans. **81,** 729-749, (2008).
3. N. Gayathri, A. K. Raychaudhuri, X. Q. Xu, J. L. Peng and R. L. Greene, J. Phys. Condens. Matter **10,** 1323 (1998).
4. G. Catalan, R. M. Bowman, and J. M. Gregg, Phys. Rev. B **62**, 7892 (2000).
5. E. Mikheev, A. J. Hauser, B. Himmetoglu, N. E. Moreno, A. Janotti, C. G. Van de Walle and S. Stemmer, Sci. Adv. **10,** 1500797 (2015).
6. M. L. Medarde, J. Phys.: Condens. Matter 9 1679 (1997).
7. S. Middey, J. Chakhalian, P. Mahadevan, J. W. Freeland, A. J. Millis and D. D. Sarma, Annual Review of Materials Research vol 46, ed D R Clarke (2016)
8. Himanshu Jain, Ph.D. thesis submitted at IISc Bangalore 2008
9. Himanshu Jain, A. K. Raychaudhuri, Ya. M. Mukovskii and D. Shulyatev, "Solid State Communication 138, 318 (2006)
10. Himanshu Jain, A. K. Raychaudhuri, Ya M. Mukovski and D. Shulyatev, Appl. Phys. Lett. 89, 152116 (2006)
11. Himanshu Jain, A. K. Raychaudhuri, Nilotpal Ghosh and H. L. Bhat, Phys. Rev B 76, 104408 (2007)
12. P. Padhan, W. Prellier, Ch. Simon, and R. C. Budhani, Phys. Rev. B 70, 134403 (2004)
13. C N R Rao, A R Raju, V Ponnambalam, S Parashar, and N Kumar, Phys. Rev. B 61 594 (2000)
14. S Mercone, A Wahl, Ch Simon, and C Martin, Phys. Rev. B 65 214428 (2000)
15. Y Yuzhelevski, V Markovich, V Dikovsky, E Rozenberg, G Gorodetsky, G Jung, D A Shulyatev, and Y. M. Mukovskii, Phys. Rev. B 64 224428 (2004)
16. R. S. Bisht, S. Samanta, and A. K. Raychaudhuri, Phys. Rev. B 95 115147 (2017)
17. S Catalano, M Gibert, J Fowlie, J Íñiguez, J-M Triscone, and J Kreise, Rep. Prog. Phys. 81, 046501, (2018).
18. Eric Breckenfeld, Zuhuang Chen, Anoop. R. Damodaran, and Lane W. Martin, ACS Appl. Mater. Interfaces, 6, 22436−22444, 2014

19. https://www.apiezon.com/products/vacuum-greases/n-grease
20. https://www.lakeshore.com/products/categories/overview/temperature-products/cryogenic-accessories/varnish
21. http://research.physics.illinois.edu/bezryadin/labprotocol/Keithley2400Manual.pdf
22. E. Langenberg, E. Ferreiro-Vila, V. Leborán, A. O. Fumega, V. Pardo, and F. Rivadulla, APL MATERIALS 4, 104815 (2016)
23. https://www.lakeshore.com/products/categories/specification/temperature-products/cryogenic-accessories/varnish
24. https://www.lakeshore.com/products/categories/specification/temperature-products/cryogenic-accessories/grease
25. J. Gao, S. Q. Shen, T. K. Li, and J. R. Sun Appl. Phys. Lett., 82, 26, 2003
26. Will J. Hardy, Heng Ji, Evgeny Mikheev, Susanne Stemmer, and Douglas Natelson, Phys. Rev. B 90, 205117 (2014)
27. A. A. Fursina, R. G. S. Sofin, I. V. Shvets, and D. Natelson, Phys. Rev. B **79**, 245131 (2009)
28. Haoliang Huang, Zhenlin Luo, Yuanjun Yang, Yu Yun, Mengmeng Yang, Dechao Meng, Haibo Wang, Sixia Hu, Jun Bao, Yalin Lu, and Chen Gao, AIP Advances **4**, 057102 (2014)
29. P. Padhan, W. Prellier, Ch. Simon, and R. C. Budhani, Phys. Rev. B. 70, 134403 (2004).
30. J. F. Wang, L. P. Chen, Y. C. Jiang, and J. Gao, J. Appl. Phys. 113, 17E151 (2013).
31. F. X. Hu, J. Gao, and X. S. Wu, Phys. Rev. B. 72, 064428 (2005).
32. T. Wu, S. B. Ogale, J. E. Garrison, B. Nagaraj, Amlan Biswas, Z. Chen, R. L. Greene, R. Ramesh, T. Venkatesan and A. J. Millis OLUME 86, NUMBER 26 Phys. Rev. Lett. 86, 25 (2001).
33. Dasheng Li, Abhishek A. Sharma, Darshil K. Gala, Nikhil Shukla, Hanjong Paik, Suman Datta, Darrell G. Schlom, James A. Bain, and Marek Skowronski, ACS Appl. Mater. Interfaces 8, 12908−12914 (2016)
34. Gi Yong Lee , Howon Kim a , Bongjin Simon Mun , Changwoo Park, Honglyoul Ju, Current Applied Physics 17 (2017) 1444e1449
35. 6Y. Tokura and N. Nagaosa, Science 288, 462 (2000)
36. Teruo Kanki, Kenichi Kawatani, Hidefumi Takami, and Hidekazu Tanaka, Appl. Phys. Lett. 101, 243118 (2012)

Chapter 6 Disorder induced signature of Anderson transition in a Mott system

Presence of disorder in a system undergoing a correlation driven transition is a topic of great interest from last decade. We show that the introduction of disorder in a controlled way using swift heavy ion irradiation suppresses the correlation driven metal-insulator transition (MIT) in $NdNiO_3$ films and makes the system looks like a heavily disordered metal governed by weak localization. The disorder (atomic displacement up to 2% of the total atoms) in the $NdNiO_3$ films was created using 1 MeV Ar^{4+} ion irradiation. The extent of disorder was varied by different irradiation time. We show, that the pristine film shows an MIT at 180 K and consistent with the Mott type behavior of the MIT. At low temperature, such a film shows Variable Range Hopping (VRH) with conductivity $\sigma \rightarrow 0$ at $T=0$. For disorder, up to 1% of displaced atoms or lower the insulating state is suppressed and the system shows a weak localization behavior with $\sigma \neq 0$ at $T=0$. Supporting evidence from Raman Spectroscopy as well as X-Ray studies show that these effects of Anderson transition and proximity to a disordered metallic state persist till the basic integrity of the NiO_6 octahedra is preserved.

6.1 Introduction

As discussed earlier, being one of the oldest problems, the metal-insulator transition (MIT) is still one of the interesting problems in the scientific community, particularly in oxides. The oxides are widely used to understand the phenomenon and to probe different issues like charge ordering, orbital ordering, spin ordering, phase separation, and nature of insulating states [1, 2]. In oxides like rare earth nickelates ($RNiO_3$), that is well known to show the first order MIT for all rare earth except Lanthanum (La), a plethora of external stimuli can change the metal-insulator transition temperature (T_{MI}). While the effect of strain, lattice symmetry, pressure, and carrier doping is widely investigated for $RNiO_3$, the effect of disorder is not looked into with much details [3].

It is interesting, as it is emerging in last decade or so that the MIT has aspects of both Mott transition and Anderson transition so that one has mixed first-order and second-order transitions with co-existence of different electronic phases. As it is known that the presence of disorder in an interacting system gives rise to various physical phenomenon [4-7]. It is well known for correlated metals that sufficient disorder can lead to localization effect which further decreases the conductivity along with an opening up of a soft gap (Note: This transition is from a metal to a metal with a disorder that may have higher resistance on opening of a soft gap). Many theoretical and experimental works have shown such behavior [8].

Theoretically near the MIT, it has been shown that for a weak disorder, the phase co-existence in the system doesn't change and it looks similar to a clean system [6]. Whereas on increasing the disorder, Anderson localization comes into the picture and it has a wide impact on the phase coexisting regime. It was shown that the phase co-existence region shrinks for the sufficiently strong disorder [6]. We note that most of the problems on the introduction of the disorder were approached from metallic side. More recently it has been shown that isovalent substitution of Ru in $Sr_3(Ir_{1-x}Ru_x)_2O_7$ for $(0 \leq x \leq 0.5 \leq)$ drives the system to an antiferromagnetic metallic state. In this case, the problem was approached from the insulating side and it has been shown that the disorder can also open up a V shape gap in the Mott system [9].

Earlier reports show 200 MeV Ag^{15+} ion irradiation on $NdNiO_3$ induces strain in the sample and suppress the metal-insulator transition (T_{MI}) by increasing the bandwidth of d bands [10]. It has been shown that at such choice of ion and fluence the dominant contribution to the transport is

mainly by strain induced by a lattice. A recent report of He irradiation on $LaNiO_3$ shows that there is a thermal cross-over from metal to insulator regime, however, the extrapolated zero temperature conductivity rather looks finite in insulating state and is nearly equal to the mott minimum conductivity (σ_{mott}) for such oxides [11]. The present work is motivated by keeping the earlier reports in mind where we would like to study how disorder induced by ion irradiation can be used as a probe to understand the effect of localization in a correlation driven Mott system [6-12]. Specifically, we address the problem from the insulating side. We would like to investigate how a system, driven into an insulating state by correlation driven transition (e.g. Mott transition) can change on introduction of disorder. In particular, the specific question we address is whether the Mott type of transition can be suppressed by disorder and the insulating state can be driven into a metallic state although disordered showing weak localization.

In this chapter, the structural analysis and transport measurement were done on $NdNiO_3$ (NNO) films irradiated by Ar^{4+} ions to introduce disorder. The doses of Ar^{4+} were varied with a Fluence of 1×10^{14} ions/cm^2, 5×10^{14} ions/cm^2, and 1×10^{15} ions/cm^2. The irradiated films show that transport properties are completely dominated by the induced disorder and the disorder indeed can suppress the correlation driven Mott transition. Further confirmation was done by Raman spectra which shows a broadening of peaks that can be observed as going from lower fluence to higher fluence. Our result thus suggests that instead of in-plane compressive strain in NNO films at such fluence, the disorder plays a dominant role in transport properties and drive the system from electron-electron correlation driven Mott system to localization driven Anderson system.

6.2 Disorder induced by ion irradiation

To calculate the damage caused or disorder induced by the Swift heavy ion irradiation (SHII), we have performed the simulation using the stopping and range of ions in matter (SRIM) program [13]. The density of $NdNiO_3$ (NNO) was used from the previous reports on crystallographic properties [14]. When an ion passes through the target material, it undergoes electronic energy and nuclear energy loss [15, 16]. In our calculations, the choice of using 1 MeV Ar ions was made on the following fact:

1. The availability of the ion source.
2. At this energy, the electronic energy and nuclear energy loss were minimum.

3. At this energy, the ion travels a distance of ~ 490 nm (Thickness of our films were ~ 15 nm) and they don't stop in the NNO film but stops in the underlying $SrTiO_3$ (STO) substrate.

Figure 6.1 (a) and (b) shows the electronic energy and nuclear energy loss for the Ar ions in NNO film. Further, the damage and vacancies created by the Ar ions on interactions with NNO were calculated from the Monte Carlo based program called TRIM (transport of ions in the matter). In Figure 6.2, we show the recoil distributions for the different elements of NNO. The knocked-out atoms Nd, Ni, and O are 0.8 x10^7, 0.9 x10^7, and 1.8 x10^7 $\frac{Atomscm^{-3}}{Atomscm^{-2}}$ respectively. The total knocked out atoms (atomic displacements) is nearly 3.5 x10^{22} atoms/cm^3. Now for a fluence of 1 x10^{15} ion/cm^2, if 99 % of the damage anneals instantly and the vacancy rate is 0.35 vacancies/ target atom (as calculated from TRIM). The retention after thermal annealing is ~ 3.5x10^{20} atoms/cm^3. Now dividing it with the atomic density of NNO gives a disorder of nearly 2 %.

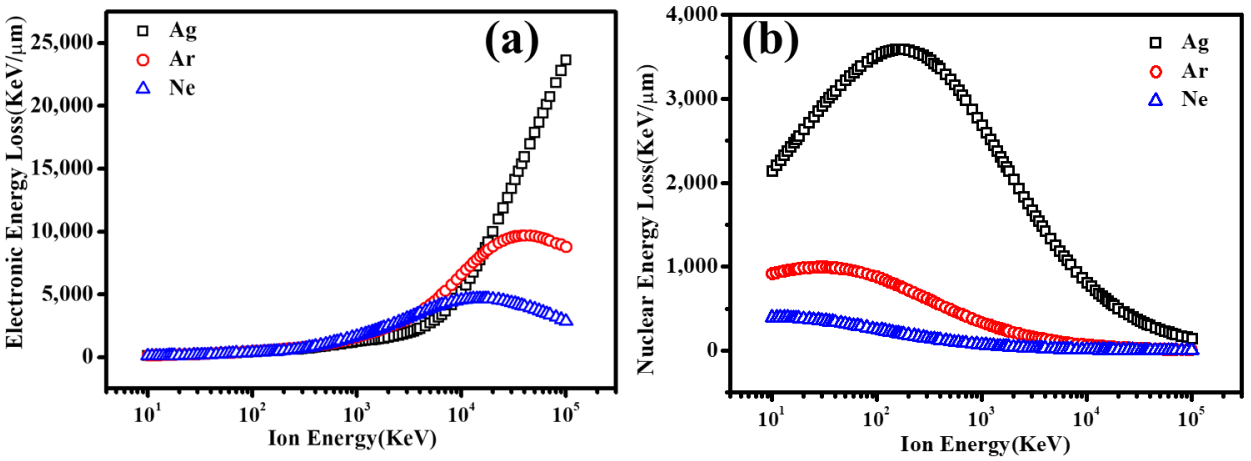

Figure 6.1 (a) Electronic energy loss and (b) Nuclear energy loss for the NNO films.

The ion irradiation was performed in a tandem accelerator with irradiation by 1 MeV Ar^{4+} to achieve an ion current of 250 pnA. Depending on the charge state of the Ar, the ion current ($I = \frac{q}{t}$) was calculated accordingly. During irradiation a beam of Ar^{4+} ions was scanned uniformly over 1 cm^2 area, the scanned area over the films were monitored during the irradiation. The large beam area with respect to sample size (5 mm × 2 mm) ensures uniform irradiation. The doses of Ar^{4+} were varied by varying the irradiation time as given in Table 6. The films were irradiated with a Fluence of $1 \times 10^{14}/cm^2$, $5 \times 10^{14}/cm^2$, and $1 \times 10^{15}/cm^2$ respectively (hereafter NNO1, NNO2,

and NNO3). After the irradiation, samples were characterized by X-ray diffraction and Raman spectroscopy.

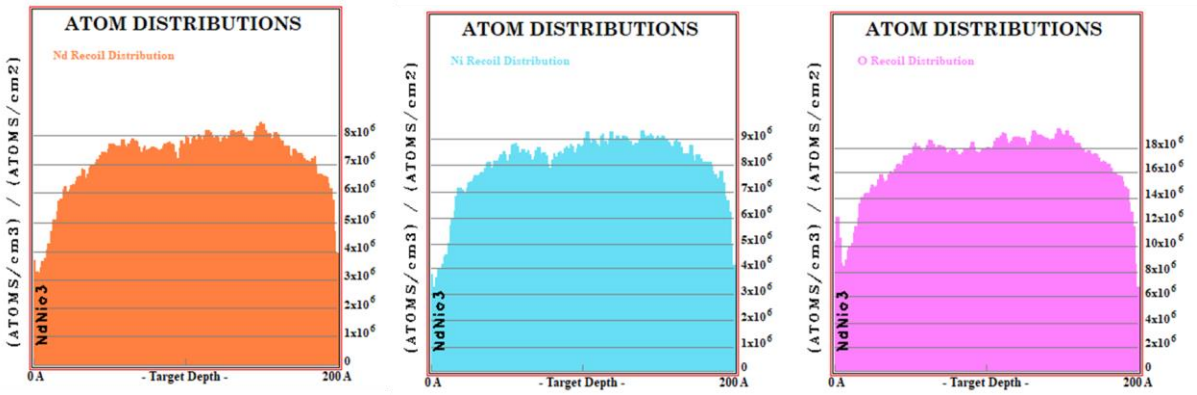

Figure 6.2 Recoil distribution of Nd, Ni and O ions on irradiation.

Table 6 The atomic displacement and irradiation time calculated on the basis of Fluence from TRIM.

Sample	Fluence (ions/cm^2)	Disorder (atomic displacement)	Irradiation time (minutes)
NNO1	1 x 10 ^{14}	0.2 %	1.06
NNO2	5 x 10^{14}	1 %	5.33
NNO3	1 x 10^{15}	2 %	10.66

6.3 Structural study of pristine and irradiated films

To understand the effect of SHII, the high-resolution $\theta - 2\theta$ scans were taken on both pristine and irradiated films of thickness nearly 15 nm. The pristine samples were characterized using RSM (Reciprocal space mapping and XRD). The reciprocal space mapping (RSM) shows that the film is highly oriented in the direction of the substrate, however partially relaxed. The pseudocubic (103) Bragg spot further suggests that the films are partially strained relaxed (As shown in Appendix B (Figure B)). The Raman spectroscopy was performed with the Argon laser

(wavelength 488 nm) as the excitation source. Note: Due to the high background from $SrTiO_3$ (STO) substrate in Raman spectroscopy, we have used NNO film grown on $LaAlO_3$ (LAO) for the Raman spectroscopy to monitor the crystallinity of the samples after irradiation. The NNO/LAO films were irradiated with the same conditions as we used for NNO/STO.

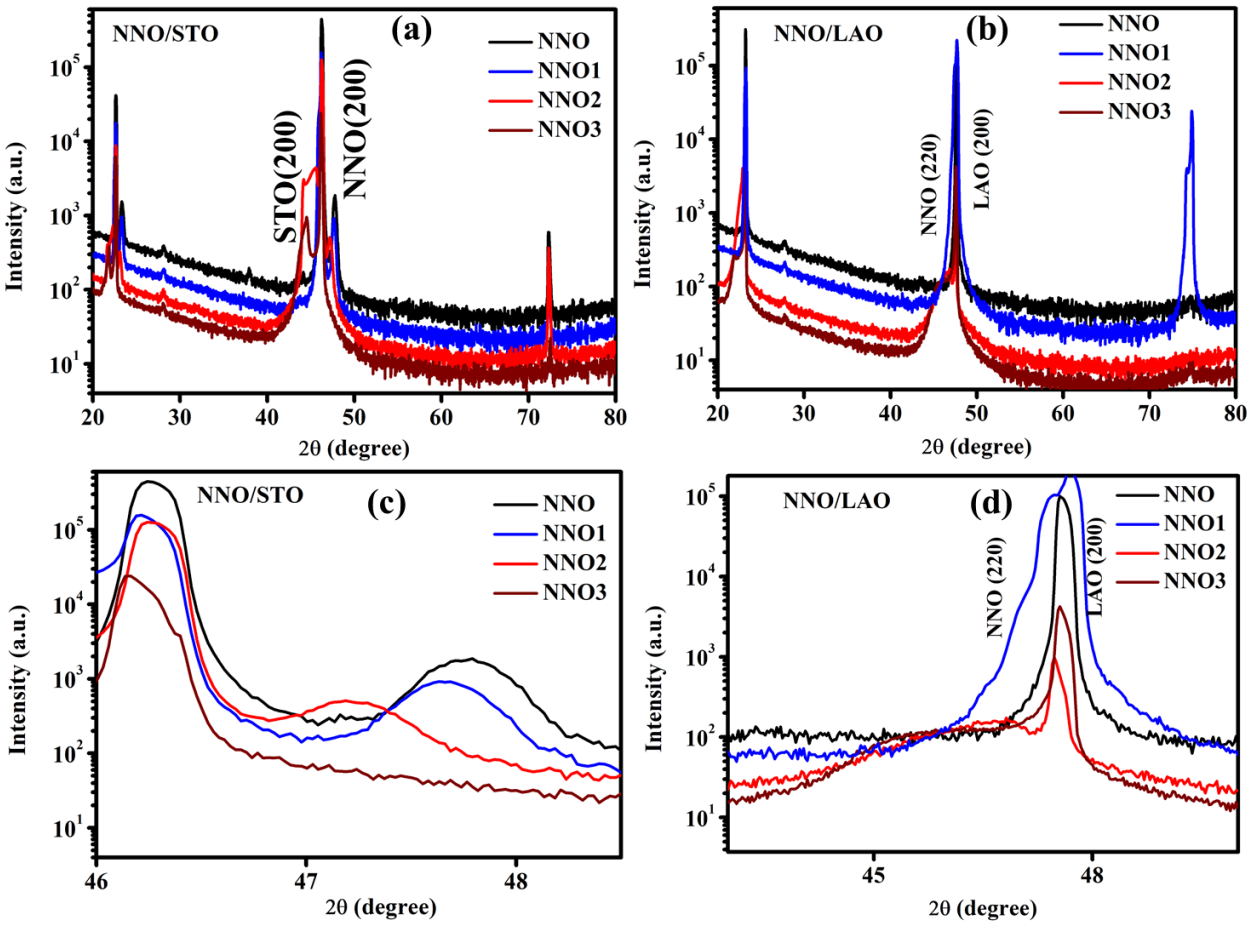

Figure 6.3 (a) Full range XRD data for pristine and irradiated films of NNO/STO, (b) Full range XRD data for pristine and irradiated films of NNO/LAO (c) Zoomed version of the XRD along (200) direction of STO, and (d) Zoomed version of the XRD along (200) direction of LAO. The XRD shows a peak broadening for the films irradiated at higher fluence.

The full scan XRD shows that film is free from any impurity phase and the oriented growth is maintained even for films irradiated with the highest dose. Due to the close lattice mismatch of $NdNiO_3$ (a_{pc} (Å) ~ 3.81) from STO (a_{pc} (Å) ~ 3.90), the films will experience a tensile strain. The growth direction $(220)_o$ of the films has been represented in orthorhombic notation which can also be interpreted as $(002)_{pc}$ in pseudocubic notation. The shift of the XRD peaks to the lower 2θ values

on irradiation shows that the out of plane lattice parameters experiences a expansion, which is consistent with earlier reports [3]. The ion irradiation is known to produce stress in the thin films [3]. The effect of a shift in the theta values to the lower values suggests that the film is under enormous stress state due to irradiation. In Figure 6.3, we show the XRD data for the pristine sample as well as for the one irradiated with different fluence. At this stage just from XRD data it is not clear whether the dynamics of the films are governed by the stress induced by the energy loss mechanism or a strong disorder induced by ion irradiation.

To further collect the information about the structural evolution and the integrity of the NNO structure in the irradiated films, we have performed Raman spectroscopy as it is a local structure sensitive tool and can give information to what happens to the NiO_6 octahedron that is at the core of the NNO structure. Theoretically, there are 24 Raman active modes that have been predicted for the structurally distorted oxides like $NdNiO_3$. Experimentally only few Raman modes have been observed, our data is consistent with the earlier reports in the current spectral range [17-18]. The observed E_g and A_{1g} Raman modes are related to the change in bond length and the rotation of oxygen octahedra respectively [17-18].

Figure. 6.4 shows the Raman spectra for the pristine and irradiated films of NNO on LAO single crystal substrates. As can be seen that the Raman modes for the NNO, NNO1 and NNO2 films show similar Raman bands, however, the Raman bands get completely suppressed for the NNO3 film that has atomic displacement ~2% and thus can be at the onset of amorphization. The Raman spectra thus suggest a change in crystallographic structure or surface amorphization for NNO3 film [19]. In this film the basic integrity of the octahedra has been lost. As shown in Figure 6.3 and Figure 6.4, the XRD data rule out the possibility of any change in crystallographic structure, hence the disappearance of Raman bands due to stress released by a disordered lattice gives a signature of surface amorphization for NNO3.

The XRD and Raman data thus show that the films get progressively modified on SHI irradiation without undergoing any structural changes. Up to a fluence of $5x10^{14}$ ions/cm^2 when the disorder is ~1%, the integrity of the NiO_6 octahedra that decide the physical properties of these systems, are maintained.

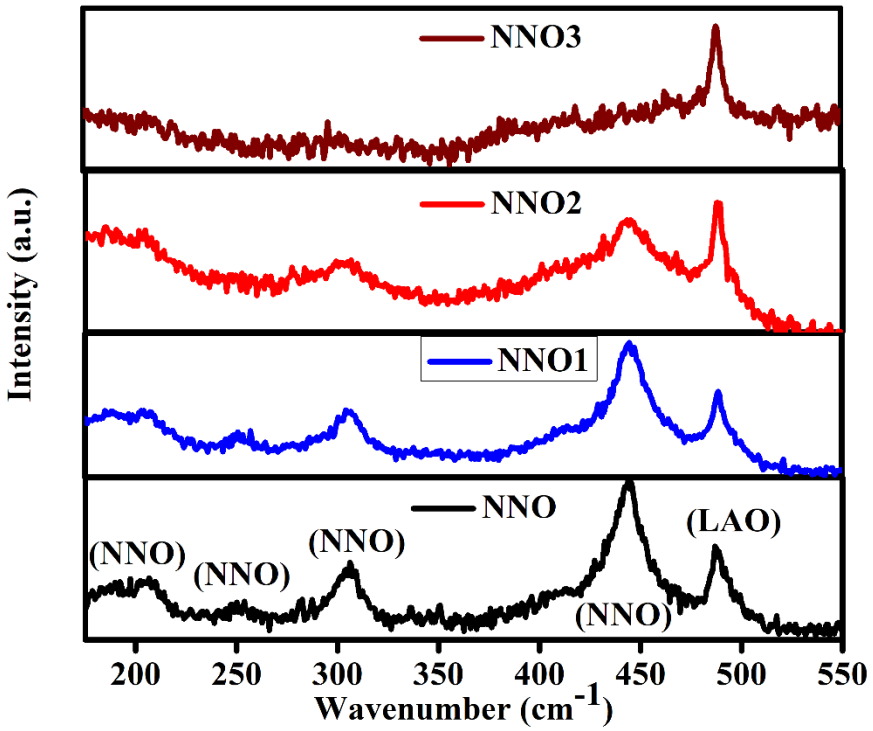

Figure 6.4 Raman spectra for pristine and irradiated films of NNO/LAO. Due to the high background from STO substrate in Raman Spectroscopy, we have used NNO film grown on $LaAlO_3$ (LAO) for the Raman Spectroscopy to monitor the crystallinity of the samples after irradiation. The NNO/LAO films were irradiated with the same conditions as we used for NNO/STO.

6.4 Resistivity as a function of temperature

The electrical transport measurement was performed in all the films down to 3 K in a collinear four-probe configuration. In Figure 6.5 (a), we show the resistivity data for all the films. Resistivity data for pristine NNO film shows a change from negative temperature coefficient of resistivity (NTC) to a positive temperature coefficient of resistivity (PTC). The T_{MI} ~ 180 K was identified as a change in the slope of the resistivity. To understand the nature of metallic regime (high temperature) with PTC in pristine film, the data were fitted with the equation given below

$$\rho(T) = \frac{\rho^*(T)\rho_{sat}}{(\rho_{sat}+\rho^*(T))} \qquad (6.1)$$

where $\rho^*(T) = \rho_0 + BT^m$ and ρ_{sat} is a parallel high resistance when resistivity approaches the Mott-Ioffe-Regel limit (Use of this expression to analyze the metallic regime gas been discussed

before in Chapter 4). The exponent m is closed to 2 and shows the Fermi liquid behavior as expected for the nickelate films which experience tensile strain [20]. At high temperature the NNO1 and NNO2 may have NTC. In case of NNO1, the resistivity at high temperature is nearly independent of temperature and the temperature coefficient of resistivity $(\frac{1}{\rho}\frac{d\rho}{dT})$ at room temperature is - 8.17×10^{-3}/K. For NNO2, the resistivity has more developed NTC with temperature coefficient of resistivity is - 2.41×10^{-3}/K. This behavior is what one expects in a bad metal with NTC. NNO1 appears to stand at the boundary of an NTC and PTC type metals.

The $RNiO_3$ are known to show the Mott variable range hopping in the insulating side (at low temperature), as at low temperature the hopping between two localized states is the mode of electrical transport [21, 22]. In our pristine film, the insulating side below 20 K follows the Mott variable range hopping relation (equation 6.2) and is consistent with the earlier results reported for the pristine NNO film. The values extracted from the fit shows σ_{0M}= 42.5 S/cm and T_0 = 597 K. In the relation of variable range hopping, the T_0 is related to the density of localized states [23, 24]. The fit of the data has shown in Figure 6.5 (b).

$$\sigma = \sigma_{0M} T^{-\frac{1}{4}} exp\left(-\left(\frac{T_0}{T}\right)^{\frac{1}{4}}\right) \qquad (6.2)$$

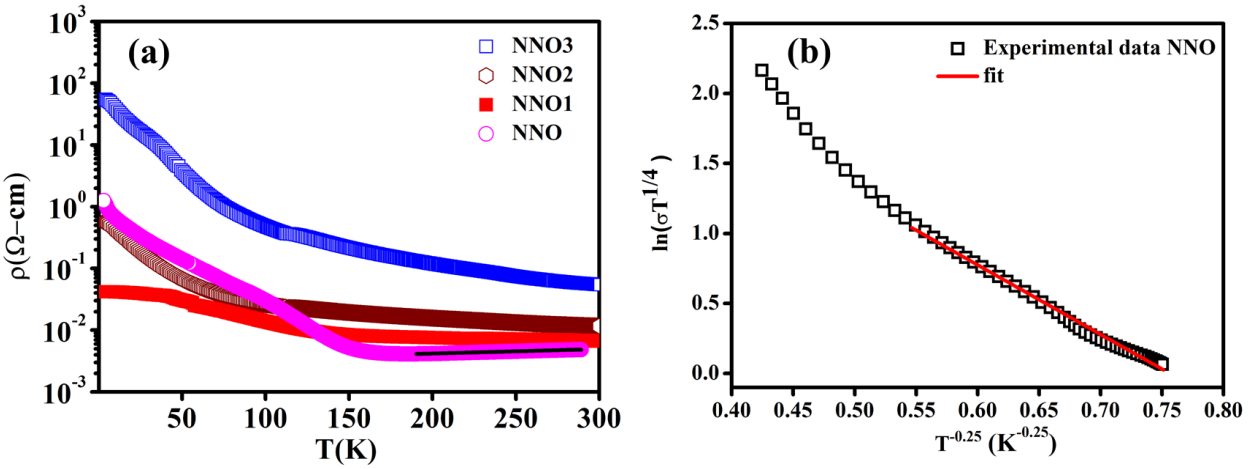

Figure 6.5 (a) The resistivity data for NNO, NNO1, NNO2 and NNO3 films (Solid black line represent fit from the equation 6.1 mentioned in the main text) and (b) Fit to NNO below 20 K from equation 6.2.

We further show that for the pristine film (NNO), the quantity $W \equiv \frac{dln\sigma}{dlnT}$ diverges as temperature approaches zero [25]. In Figure 6.6 (a), we show the diverging nature of $\frac{dln\sigma}{dlnT}$ at low temperature for NNO film. The more details on the diverging/converging nature of $\frac{dln\sigma}{dlnT}$ has given in chapter 4 of this thesis.

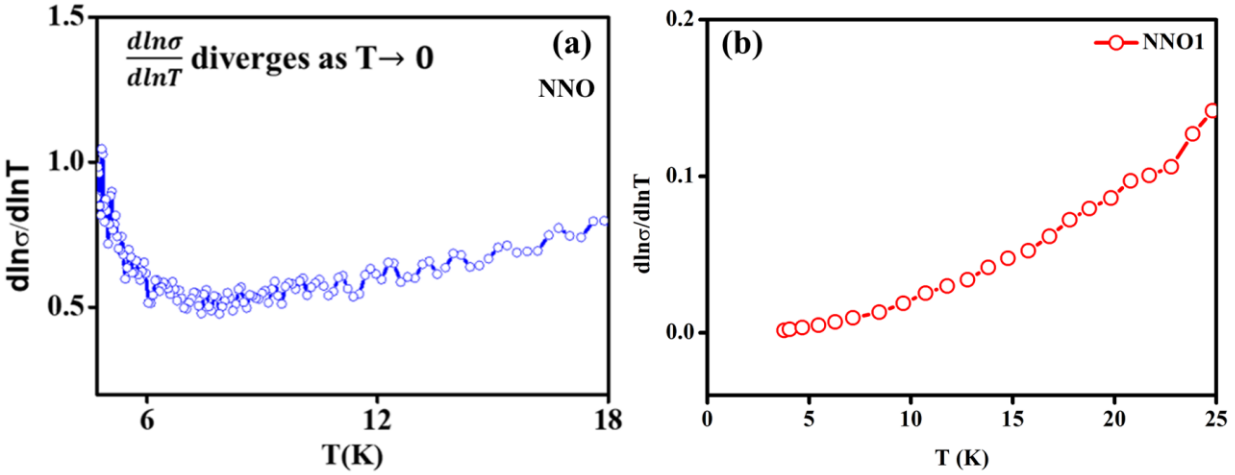

Figure 6.6 (a) $\frac{dln\sigma}{dlnT}$ as a function of temperature at low temperature for NNO and (b) NNO1 films. The diverging nature of $\frac{dln\sigma}{dlnT}$ for NNO is consistent with the Mott variable range hopping.

Interestingly, in the irradiated films with the lowest disorder (NNO1) disorder, the resistivity at higher temperature ($T > T_{MI}$, T_{MI} being the MIT temperature of the pristine film NNO) is similar to the pristine film and may be somewhat higher. The MIT is severely suppressed if not absent and at lower temperature, absence of MIT leads to a resistivity that is much less than the pristine film (NNO). This in itself is important because it is conventional wisdom that disordering by irradiation, in general, leads to increase of resistivity. In this case, however, the opposite has happened. The suppression of the resistivity and absence of a discernible T_{MI} can thus be interpreted as the central inference that disorder has indeed suppressed the correlation driven transition. We have plotted $W \equiv \frac{dln\sigma}{dlnT}$ in Figure 6.6 (b) for NNO1. It shows that $W \to 0$ supporting the inference that a metallic state indeed has been obtained by disordering a Mott insulator. The result is important that it has been carried out by introducing disorder without changing the stoichiometry that often happens when disorder is introduced by substitution (see Chapter 4).

For NNO2, though the resistivity at higher temperature is higher than that of NNO, at lower temperature, the resistivity falls below that of NNO, although there is a clear upturn at $T < 75K$. Importantly at the lowest temperature, the conductivity (and hence resistivity) reaches a constant value with $W \to 0$, signifying existence of a metallic state although of very high resistivity. While the observation made on the high temperature side ($T > T_{MI}$) has been reported previously for many systems on application of disorder [10, 11], the data on the low-temperature side is rather interesting and not been observed for the correlated electron system before. In particular, clear suppression of the insulating state and emergence of the metallic state by disorder is a new result. In particular, clear suppression of the insulating state and emergence of the metallic state by disorder is a new result.

For NNO3 the level of the disorder being much high (2%), as shown by the Raman data the film has lost the integrity of the NiO_6 octahedra and doesn't show the Raman modes associated with it. In this film the resistivity becomes very high and the film becomes an insulator. Thus there is a small window of disorder that the correlation driven MIT is suppressed and the metallic state (bad metallic though it may be) is restored. At higher disorder (as in NNO3), the damage to the structure takes over restoring the insulating state but is not the insulating state that has been ushered in NNO by correlation.

The conductivity data for films NNO1 and NNO2 below 40 K follow the weak localization relation given below [24, 26]:

$$\sigma(T) = \sigma_0 + kT^{p/2} \tag{6.3}$$

where the factor $k \equiv \frac{2e^2}{\xi h\pi^2}$, e is the electronic charge and ξ(de-phasing length scale) is related to the Thouless length $L_{TH} = \xi \mathrm{T}^{-\mathrm{p}/2}$. From the weak localization theory, when the interaction effect is weak $p \approx 4$ [26]. We show p/2 are 1.96 and 1.85 respectively for NNO/STO1 and NNO/STO2 that matches fairly with the exponent suggested from weak localization theory. The fit of the data has shown in Figure 6.7 (a) and (b). The resistivity analysis of the NNO/STO1 and NNO/STO2 thus suggest that the transport is dominated by the interference of the backscattered electrons. The fit to the low-temperature data has shown in Figure 6.7 (a) and (b).

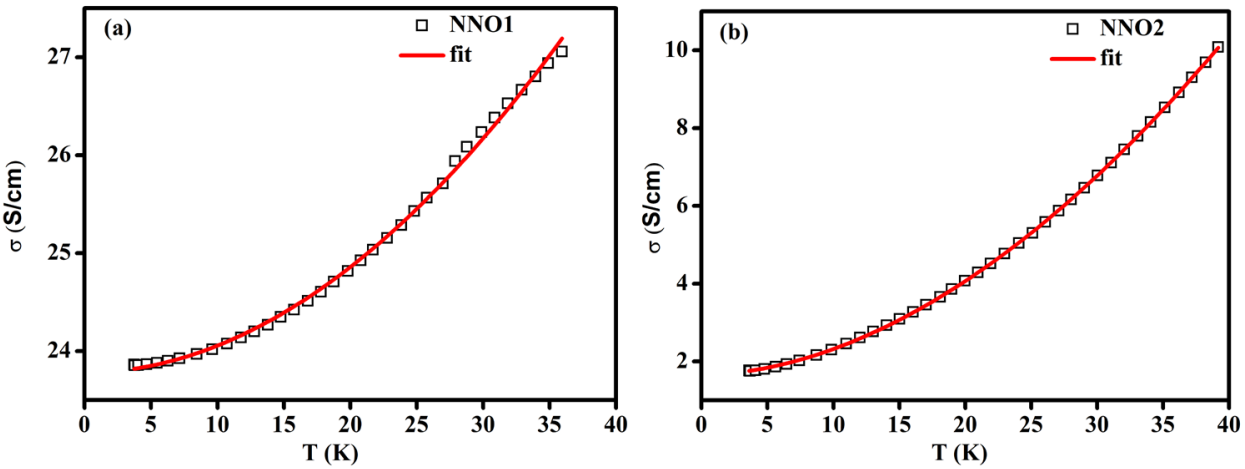

Figure 6.7 Fit to Conductivity data at low temperature for the (a) NNO1 and (b) NNO2 from equation 6.3.

6.5 Discussion

The effect of disorder produced by ion irradiation on different perovskite oxide systems has been investigated widely. It has been suggested that the disorder plays an important role in the transport properties and hence changes the nature of electrical transport completely. Below in Table 6.1, we give some of the results on different system and the observations made in order to put our observations in perspective.

The results and observation on metallic $LaNiO_3$ shows increase in resistivity as the disorder increases. Further, the highest disorderd film shows a change in resistivity by nearly four order [10]. Similar results were obtained by Wang and co-workers on metallic $LaNiO_3$ and $PrNiO_3$ that shows on increasing the disorder the resistivity increases [11]. At this stage it is clear that the backscattering of the electrons due to disorder leads to the correction of conductivity at low temperature as well as increase in the resistivity throughout the temperature range [26].

More recently such/similar observation has been made on epitaxial $SrVO_3$ thin films on irradiation with 5 keV Helium ions [27]. While the studies on $NdNiO_3$ system [3] show suppression of the T_{MI} as well as resistivity in the whole temperature regime on increasing disorder [3]. At this stage it is not clear why the metallic state in the $NdNiO_3$ shows suppression of resistivity on increasing the disorder. It may happen that the energy used for irradiation by Ag ions create different types of disorder like extended defects that can arise from higher electronic energy loss from 200 MeV

ions. In case of $LaNiO_3$ and $PrNiO_3$ films [11] the energy used is very low (6 keV) that leads to predominantly sputtering from surface rather than in-depth damage that happens when the ions penetrate the sample. In such case the surface-induced scattering from a sputtered surface and enhance resistivity.

Table 6.1 Some observation seen for effect of irradiation-induced disorder on different perovskite oxide system

System	Source of Disorder	Observation/Remark
$LaNiO_3$ films [10]	200 MeV Ag^{15+} ions	Suppression of resistivity due to the ion irradiated films.
$NdNiO_3$ films [3]	200 MeV Ag^{15+} ions	Stress generated due to irradiation decrease the T_{MI} to lower temperature.
$LaNiO_3$ and $PrNiO_3$ films [11]	6 keV He ions	The ion-induced disorder driven the system from metallic to insulating regime.
$NdNiO_3$ films (present work)	1 MeV Ar^+ ions	Enhancement of conductivity at lower temperature and suppression of conductivity at the higher temperature.

The current question of this study is what happens to the temperature driven Mott transition that is driven by electron-electron correlation in presence of disorder. It may happen that the disorder created by the ion irradiation has a competition of stress generated (which changes the bandwidth and hence may stabilize T_{MI} to lower temperature) and localized states created. It has been shown for $Sr_3(Ir_{1-x}Ru_x)_2O_7$ that introduction of disorder can lead to opening up of a gap with power-law nature in the system on Ru substitution [9]. In this study the substitution is the cause of the disorder given the small ionic size mismatch of Ir (200pm) and Ru (205pm). The observation made by us has similarity with the observation above. The disorder leads to the enhancement of scattering in the metallic state ($T > T_{MI}$) thus increasing the resistivity while the resistivity of insulating state is suppressed and shows a weak localization behavior. Khomskii suggested that the interplay of the electrons localization (due to correlation and due to disorder) doesn't simply add up but counteract each other [8]. It may happen that electrons sitting at random potential in presence of

strong electron-electron repulsion can be kicked out from the random site and may facilitate metallic conductivity [8].

6.6 Conclusion

- The ion irradiation can be used as a knob to introduce the disorder in a controlled way.
- The $NdNiO_3$ system which is known to show first-order correlation driven metal insulator transition, the insulating state can be suppressed on increasing the disorder and shows character of Anderson localization.
- The tools like Scanning tunneling spectroscopy can be utilized as a tool to probe the density of states at the Fermi level. Such experiments will give a clear idea of gap opening up in the presence of disorder.
- More theoretical work is required to understand the phenomenon of co-existence of Anderson and Mott transition together.

Bibliography for Chapter 6

1. G. Catalan, Phase Trans. 81, 729, (2008).
2. S Catalano, M Gibert, J Fowlie, J Íñiguez, J-M Triscone, and J Kreise, Rep. Prog. Phys. 81, 046501, (2018).
3. Yogesh Kumar, R. J. Choudhary, and Ravi Kumar, Journal of Applied Physics 112, 073718 (2012)
4. D. M. Basko, I. L. Aleiner, and B. L. Altshuler, Ann. Phys. (N.Y.) 321, 1126 (2006).
5. A. Georges, G. Kotliar, W. Krauth, and M. J. Rozenberg, Rev.Mod. Phys. 68, 13 (1996).
6. Helena Braganc¸, M. C. O. Aguiar,J. Vuˇciˇcevi´c, D. Tanaskovi´c, and V. Dobrosavljevi´c, Phys. Rev. B 92, 125143 (2015)
7. K. W. Post, A. S. McLeod, M. Hepting, M. Bluschke, Yifan Wang, G. Cristiani, G. Logvenov, A. Charnukha , G. X. Ni , Padma Radhakrishnan, M. Minola , A. Pasupathy , A. V. Boris , E. Benckiser , K. A. Dahmen, E. W. Carlson , B. Keimer and D. N. Basov, Nature Physics | VOL 14 | OCTOBER 2018 | 1056–1061
8. Daniel I. Khomskii, Transition metal Compounds, Cambridge University Press
9. Zhenyu Wang, Yoshinori Okada , Jared O'Neal , Wenwen Zhou , Daniel Walkup , Chetan Dhital , Tom Hogan , Patrick Clancy , Young-June Kim , Y. F. Hu , Luiz H. Santosa, Stephen D. Wilson , Nandini Trivedi , and Vidya Madhavana, 11198–11202 | PNAS | October 30, 2018 | vol. 115 | no. 44
10. Y. Kumar, R. J. Choudhary, A. P. Singh, G. Anjum, and R. Kumar, J. Appl. Phys. 108, 083706 (2010).
11. Changan Wang, Ching-Hao Chang, Angus Huang, Pei-Chun Wang, Ping-Chun Wu, Lin Yang, Chi Xu, Parul Pandey, Min Zeng, Roman Böttger, Horng-Tay Jeng, Yu-Jia Zeng, Manfred Helm, Ying-Hao Chu, R. Ganesh, and Shengqiang Zhou, Phys. Rev. Mat. 3, 053801 (2019)
12. Ravindra Singh Bisht, Gopi Nath Daptary, Aveek Bid and A. K. Raychaudhuri, J. Phys.: Condens. Matter, 2019, 31, 145603
13. http://www.srim.org/
14. https://materials.springer.com/isp/crystallographic/docs/sd_1813812
15. J. F. Ziegler, J. P. Biersack and U. Littmark, The stopping and range of ions in solids (Pergamon Press, New York, 1985).

16. J. P. Biersack and L. G. Haggmark, Nucl. Instr. and Meth. 174, (1980), 257. We have used the version TRIM-91.04.
17. M. Zaghrioui, A. Bulou, P. Lacorre, and P. Laffez, Phys. Rev. B 64, 081102(R) (2001).
18. Jennifer Fowlie, Electronic and Structural Properties of $LaNiO_3$ Based Heterostructures, Doctoral Thesis accepted by the University of Geneva.
19. Ming Zhang, Raman Study of the Crystalline-to-Amorphous State in Alpha-Decay–Damaged Materials http://dx.doi.org/10.5772/65910
20. E. Mikheev, A. J. Hauser, B. Himmetoglu, N. E. Moreno, A. Janotti, C. G. Van de Walle, and S. Stemmer, Sci. Adv. 1 e1500797 (2015).
21. A. Stupakov, O. Pacherova, T. Kocourek, M. Jelinek, A. Dejneka, and M. Tyunina, Phys. Rev. B 99, 085111 (2019)
22. Koushik Ramadoss, Nirajan Mandal, Xia Dai, Zhong Wan, You Zhou, Leonid Rokhinson, Yong P. Chen, Jiangpin Hu, and Shriram Ramanathan, Phys. Rev. B 94, 235124 (2016)
23. N. F. Mott, Metal-Insulator Transition. Taylor & Francis, London (1990).
24. M. Imada, A. Fujimori, and Y. Tokura, Rev. Mod. Phys. 70, 1039 (1998).
25. A. Möbius, Critical Reviews in Solid State and Materials Sciences 0 1-55 (2017).
26. P. A. Lee and T. V. Ramakrishnan, Rev. Mod. Phys.57 287 (1985).
27. https://arxiv.org/ftp/arxiv/papers/1904/1904.06629.pdf

Chapter 7 Conclusions and Future directions

7.1 Main observations of this thesis

I. The results obtained in chapter 3 for $NdNiO_3$ film grown on $LaAlO_3$ single crystal substrate established that the metal insulator transition (MIT) shows phase separation in the nanoscopic scale (few tens of nanometers) and phase co-existence. The one phase (lower conductivity) has depletion in density of states (DOS) and another phase (higher conductivity) has no depletion in DOS. The phase co-existence actually start well above the metal insulator transition temperature (T_{MI}) and the system becomes highly "inhomogeneous" electronically close to the transition temperature which leads to a large jump in the resistance fluctuation. Such phase separation may be generic in nature and may associated with other strongly correlated systems that show a temperature-driven MIT.

II. The results obtained in chapter 4 for $Nd_{0.7}La_{0.3}NiO_3$ films grown on crystalline substrates of $LaAlO_3$ (LAO), $SrTiO_3$ (STO), and $NdGaO_3$ (NGO) show how a combination of factors like strain, substrate symmetry, and disorder plays an important role in the transport properties and can change the nature of the MIT. The combination of these factors make substituted nickelates ($Nd_{0.7}La_{0.3}NiO_3$) (that are known to exhibit first-order Mott type transition), undergo a continuous transition as seen in systems undergoing disorder/composition driven Anderson transition. We establish that a cross-over from a Positive Temperature Coefficient resistance regime to Negative Temperature Coefficient resistance regime at definite temperatures does not necessarily constitute an MIT.

III. The results obtained in chapter 5 shows the electroresistance effect observed for the $NdNiO_3$ film grown on the $SrTiO_3$ (111) single crystal substrate. The resistivity measurement down to 10 K at different current shows suppression of resistivity by nearly an order without affecting the metal-insulator transition temperature. Our results show that Joule heating is unlikely the reason for the observed electroresistance effect. We discuss that the phase co-existence of the high temperature metallic and low-temperature insulating filaments that may lead to this observation.

IV. The results obtained in chapter 6 show that the introduction of disorder in a controlled way using swift heavy ion irradiation suppresses the correlation driven MIT in $NdNiO_3$ films and makes the systems looks like a heavily disordered metal governed by weak localization. The disorder (atomic displacement up to 2% of the total atoms) in the $NdNiO_3$ films was created using 1 MeV Ar^{4+} ion irradiation. the pristine film shows an MIT at 180 K and consistent with the Mott type behavior of the MIT. At low temperature, such a film shows Variable Range Hopping (VRH) with conductivity $\sigma \rightarrow 0$ at T=0. For disorder, up to 1% of displaced atoms or lower the insulating state is suppressed and the system shows a weak localization behavior with $\sigma \neq 0$ at T=0. The Raman spectroscopy as well as X-Ray studies show that these effects of Anderson transition and proximity to a disordered metallic state persist till the basic integrity of the NiO_6 octahedra is preserved.

7.2 Future directions

- Using piezoelectric substrates to tune the T_{MI} in rare earth nickelates and its implication on phase co-existence.
- Understanding the role of substrate orientation on phase co-existence and it's impact on magnetoresistance.
- Understanding the nature of phase co-existence at the tri-critical point. Do the electronic and magnetic phase co-exist ?
- More theoretical studies to understand phase co-existence in $RNiO_3$.

Appendix A: Low-temperature structural study of $Nd_{0.7}La_{0.3}NiO_3$ nanoparticles

Here, we show that the onset of resistivity in $Nd_{0.7}La_{0.3}NiO_3$ nanoparticles doesn't necessarily mean a metal-insulator transition which is accompanied by a structural change. The temperature dependent synchrotron XRD shows that there is no structural symmetry change down do 13 K. The $Nd_{0.7}La_{0.3}NiO_3$ nanoparticles were prepared by the sol-gel process as described in chapter 2. Figure A shows the SEM image of the nanoparticles and inset shows the particle size distribution. The calculated average particle size was approximately 96 nm. However, a clear size distribution can be seen.

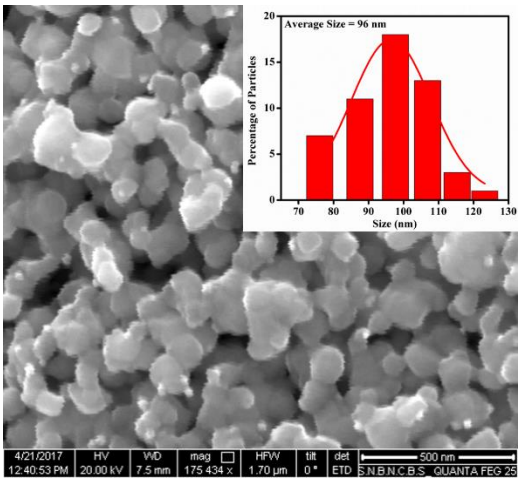

Figure A SEM image of $Nd_{0.7}La_{0.3}NiO_3$ nanoparticles, Inset shows particle size distribution.

The Resistivity (ρ) data was taken down to 3 K in a pulsed tube cryostat. The nanoparticles were pressed into a pellet and the data was taken for the heating cycle in a collinear four-probe method with a lock-in amplifier. The changeover of the sign $\frac{d\rho}{dT} = 0$ is taken as the T^*. In Figure A1, we show the resistivity and $\frac{d\rho}{dT}$ data as a function of temperature. If the upturn in resistivity is considered as metal-insulator transition then one would accept a structural change at the low-temperature region like other nickelates [1, 2]. To answer this we have performed a temperature dependent (13 K – 300 K) synchrotron XRD at KEK photon factory, Japan.

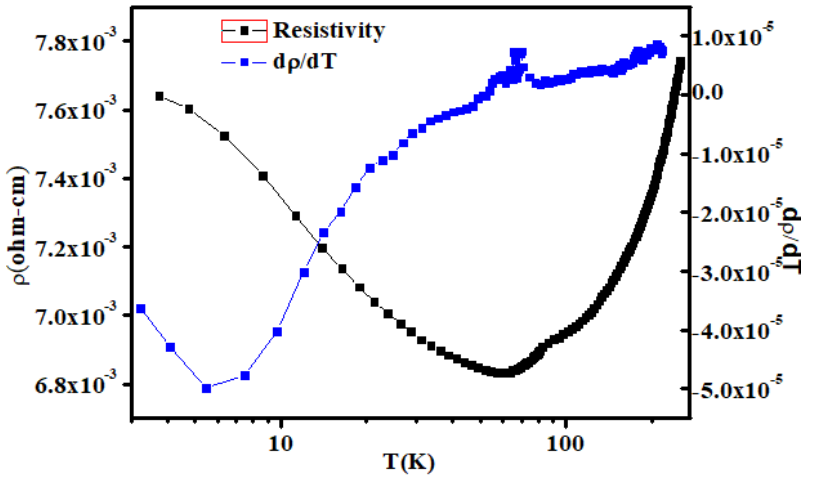

Figure A1 Resistivity and $\frac{d\rho}{dT}$ as a function of temperature for $Nd_{0.7}La_{0.3}NiO_3$ nanoparticles.

The synchrotron XRD was performed at KEK Photon factory with beam energy 15.5 eV. Figure A2 shows the XRD pattern of $Nd_{0.7}La_{0.3}NiO_3$ nanoparticles at 300 K and 13 K. It doesn't show any significant difference for the XRD pattern collected at two different temperature. The obtained occupancy using Rietveld refinement shows that there is no oxygen vacancy in the samples. The characteristics splitting for any of the peaks from orthorhombic to monoclinic transition has not observed. The lattice parameters, bond angle and Ni-O bond length were obtained by Rietveld refinement using Full Proof analysis software with Pbnm space group. The obtained lattice parameters are in good agreement with the earlier reports.

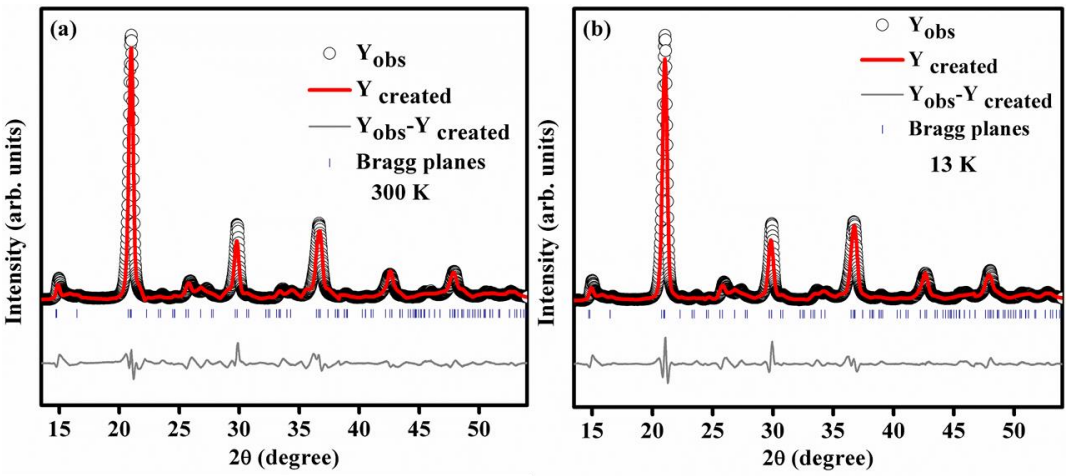

Figure A2 Synchrotron XRD pattern for the $Nd_{0.7}La_{0.3}NiO_3$ nanoparticles at (a) 300 K & (b) 13 K.

A contraction of nearly 0.3%, 0.02% and 0.09% of lattice parameters can be seen in the lattice parameters a, b, and c respectively on lowering the temperature. Similarly, a change in the unit cell volume ($\Delta V/V$) of nearly 0.38% has been observed when the temperature has been lowered down to 13 K. Thus it has been shown that the onset of resistivity upturn is not associated with any structural changes.

Table A: The lattice parameters at 300 K and 13 K

Lattice Parameters	**At 300 K**	**At 13 K**
a	5.455	5.440
b	5.378	5.377
c	7.610	7.603

1. G. Catalan, Phase Trans. **81,** 729-749, (2008).
2. M. L. Medarde, J. Phys.: Condens. Matter 9 1679 (1997).

Appendix B: Reciprocal space mapping data for different nickelate films

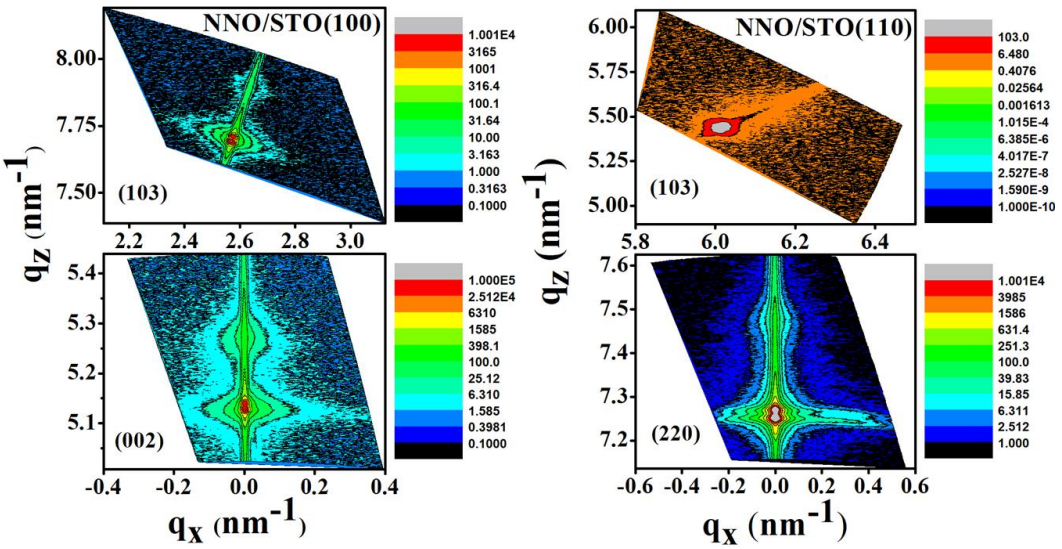

Figure B Reciprocal Space Mapping data for $NdNiO_3$(NNO) film of thickness nearly 15 nm grown on $SrTiO_3$ (STO)(100) substrate and STO (110) substrate along the $(002)_{pc}$ and $(103)_{pc}$ Bragg reflection. Here pc represents the pseudocubic notation. The films are highly oriented and partial strain relaxed. Colour code represent intensity.

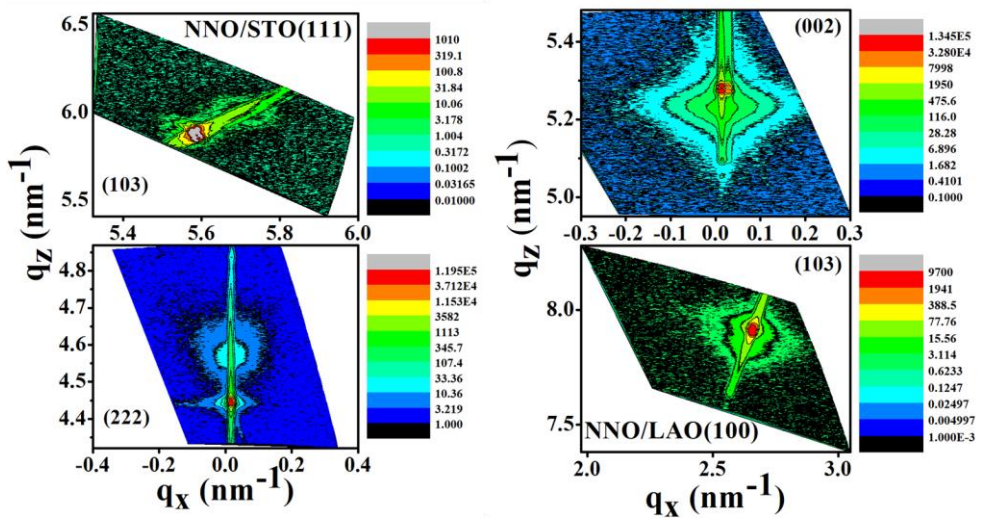

Figure B1 Reciprocal Space Mapping data for $NdNiO_3$(NNO) film of thickness nearly 15 nm and 60 nm grown on $SrTiO_3$ (STO)(111) substrate and $LaAlO_3$ (100) substrate along the $(002)_{pc}$ and $(103)_{pc}$ Bragg reflection. The films are highly oriented and partial strain relaxed.

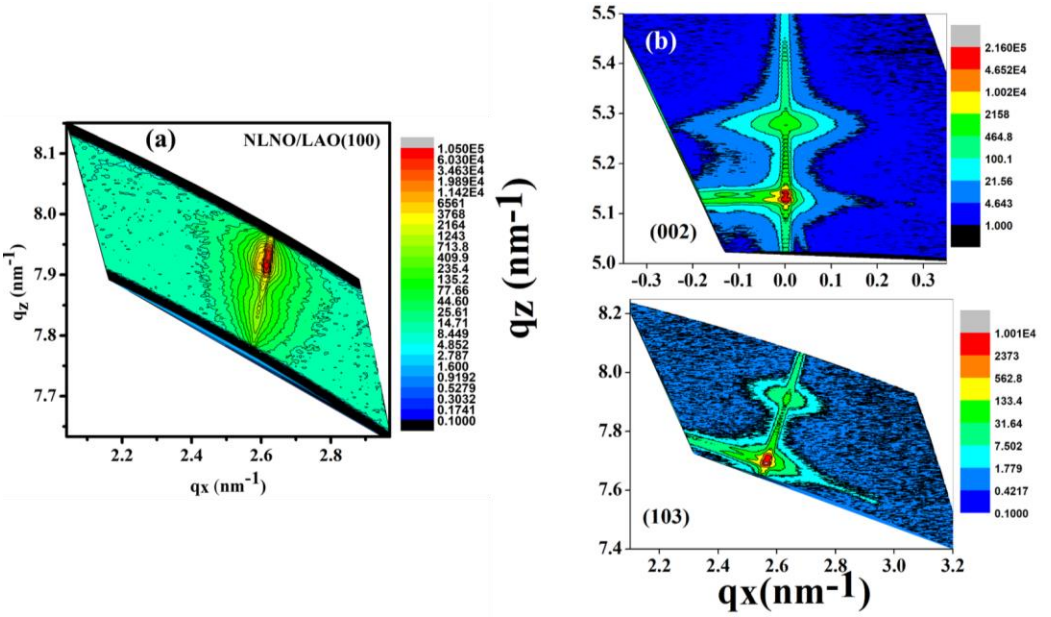

Figure B2 Reciprocal Space Mapping data for $Nd_{0.7}La_{0.3}NiO_3$(NLNO) film of thickness nearly 80 nm grown on (a) $LaAlO_3$ (LAO)(100) and (b) $SrTiO_3$ (STO)(100) substrate along the $(002)_{pc}$ and $(103)_{pc}$ Bragg reflection. The films are highly oriented and partial strain relaxed.

Appendix C: Resistance as a function of current for $NdNiO_3$ film grown on $SrTiO_3$ (100) substrate

Here we show the electroresistance data for nearly 14 nm thick $NdNiO_3$ film grown on $SrTiO_3$(100) single crystal substrate. The resistance as a function of temperature was taken down to 3 K for different current in a collinear four probe configuration. The observed effect of suppression in resistance without affecting the metal insulator transition temperature on high current bias is consistent with the electroresistance effect observed in chapter 5. In Figure C, we show the resistance data as a function of temperature at three different current.

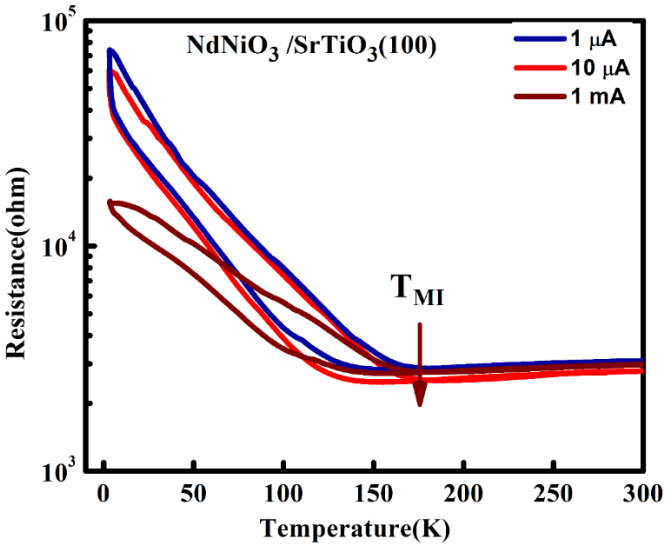

Figure C The resistance as a function of temperature for different current bias for nearly 14 nm $NdNiO_3$ film grown on $SrTiO_3$ (100) single crystal substrate. The metal insulator transition is unaffected while a suppression in resistance can be seen due to electroresistance effect.